

**UNIVERSITY OF SOUTHAMPTON**

# **Applications of Microfluidics in Nuclear Magnetic Resonance**

by

William G Hale

A thesis submitted in partial fulfillment for the  
degree of Doctor of Philosophy

in the  
Faculty of Engineering and Physical Sciences  
School of Chemistry

June 2019



UNIVERSITY OF SOUTHAMPTON

ABSTRACT

FACULTY OF ENGINEERING AND PHYSICAL SCIENCES  
SCHOOL OF CHEMISTRY

Doctor of Philosophy

by William G Hale

Microfluidics is a constantly growing field of research finding applications in a diverse range of subjects such as materials science, chemistry and across the life sciences. This is due to many advantageous attributes that microfluidics enjoys, namely small sample volumes which contribute to waste reduction and reduced cost of experimentation; highly controllable local environments that enable very precise investigation of changes in systems to stimuli; rapid prototyping techniques meaning make, test, tweak cycles can be run more than once in a typical day; ease of parallelisation makes gathering statistically significant data much easier without the need to repeat experiments for days at a time; and ease of automation increases precision and repeatability.

Nuclear magnetic resonance (NMR) spectroscopy is widely applied technique in chemistry and the life sciences. Its non-invasive and non-destructive nature makes it ideal to study living, or mass limited samples. However, it is limited by having to have an extremely homogenous magnetic field as well as the low sensitivities possible in a typical experiment.

This thesis describes methods for integrating these two fields. Some NMR experiments being ‘miniaturised’ to be performed ‘on-chip’ as well as microfluidic concepts that have been engineered to be compatible with NMR techniques. These techniques do not seek to replace established methods of microfluidic analysis such as mass spectrometry or fluorescence spectroscopy but could be used to compliment these techniques as an additional method of extracting data from the system.



# Contents

<b>Nomenclature</b>	<b>xv</b>
<b>Acknowledgements</b>	<b>xvii</b>
<b>1 Introduction</b>	<b>1</b>
<b>2 Background</b>	<b>3</b>
2.1 Microfluidics . . . . .	3
2.1.1 History to present day . . . . .	3
2.2 NMR theory . . . . .	12
2.2.0.1 Nuclear Spin . . . . .	12
2.2.0.2 Spin Systems . . . . .	13
2.2.0.3 Pauli matrices and more Operators . . . . .	16
2.2.0.4 Density Operator . . . . .	18
2.2.1 The Hamiltonian . . . . .	21
2.2.1.1 Spins in a magentic field . . . . .	21
2.2.2 Spin precession . . . . .	23
2.2.3 Rotating Frame . . . . .	24
2.2.3.1 Precession in the rotating frame . . . . .	25
2.2.4 Radio Frequency Pulses . . . . .	25
2.2.4.1 $x$ -pulse . . . . .	26
2.2.4.2 Pulse of general phase . . . . .	27
2.2.4.3 Off-resonance effects . . . . .	28
2.2.5 The Density operator revisited . . . . .	29
2.2.5.1 Magnetization vector . . . . .	30
2.2.5.2 Density operator under pulses . . . . .	31
2.2.6 Free evolution with Relaxation . . . . .	32
2.2.6.1 Transverse relaxation . . . . .	33
2.2.6.2 Longitudinal relaxation . . . . .	34
2.2.7 NMR signal and detection . . . . .	35
2.2.7.1 Quadrature detection . . . . .	36
2.2.7.2 Signal after a pulse . . . . .	38
2.2.7.3 Fourier Transform . . . . .	39
2.2.7.4 Chemical Shift and J-coupling . . . . .	41
2.3 Micro-NMR . . . . .	42
2.3.1 Sensitivity . . . . .	42
2.3.1.1 Signal to noise ratio . . . . .	42

---

2.3.2	Limit of Detection . . . . .	44
2.3.3	Concentration limit of detection . . . . .	45
2.3.4	Transmission line probe . . . . .	45
<b>3</b>	<b>Microfluidic Droplet NMR</b>	<b>49</b>
3.1	Abstract . . . . .	49
3.2	Introduction . . . . .	49
3.2.1	Susceptibility . . . . .	51
3.2.2	Matching susceptibilities in emulsions . . . . .	53
3.3	Materials and Methods . . . . .	57
3.4	Results and Discussion . . . . .	60
3.5	Conclusion . . . . .	65

# List of Figures

1.1	Microfluidic devices developed for this work, as well as for other applications in microfluidic NMR. From the left: A device for perfusion culture of a tissue slice on chip; capable of peristaltic pumping; hydrogenation on a chip; droplet generation; simple sample chamber filler; 2D/3D cell culture device. Figure taken from [1] . . . . .	2
2.1	Coponents of a microfluidic device got increasingly complicated. This device from Ref.[2] performs immunoassays - widely used in medical and biological research. The screws (dashed circles) are manually operated valves. Water with green dye shows the channels. . . . .	5
2.2	Formation of droplets in a T-Junction of a microfluidic device the continuous hydrocarbon phase disperses a water phase. Figure from [3] . . . . .	6
2.3	A collection of microfluidic devices that enabled cell based assays from cell culture, to selection and treatment, to analysis. <b>a</b> , Six biorexctors are operated in parallel in a single chip to monitor small numbers of cells [4], <b>b</b> , Microfluidic cell-culture array with integrated concentration gradient generator (left). Image of concentration gradient when blue and yellow dye is used (right) [5]. <b>c</b> Two laminar streams exposing two sides of a single cell to different conditions [6]. <b>d</b> , Perfusion over a single trapped cell. The perfusion media can be switched in 100 ms [7]. <b>e</b> , (left) Cell dielectrophoresis trap. (right) Fluorescent image of trapped cell indicated by blue arrow [8]. <b>f</b> , Fluorescent image of light path at the detection zone in a micro flow cytometer [9]. <b>g</b> Scanning electron micrograph of a mechanical lysis device with sharp knife-like protrusions [10]. <b>h</b> , Schematic of electrical lysis device with microelectrodes [11]. <b>i</b> , Isoelectric focusing of cell organelles [12]. <b>j</b> , Two-dimensional separation of four model proteins. Isoelectric focusing (top) followed by SDS gel electrophoresis [13]. <b>k</b> , Schematic of immunoassay using microbeads as a solid support [14]. <b>l</b> , Schematic of a hollow cantilever-mased mass sensor for analyte detection [15]. Taken from Ref.[16] . . . . .	7

2.4	Organ-Organ and tissue-tissue interfaces in microdevices. Liver chip: A microfluidic liver device with cell culture and flow chambers separated by a baffle that separates cultured hepatocytes from fluid flow to simulate the endothelial-hepatocyte interface of the liver sinusoid. This geometry promotes alignment of hepatocytes in two lines that facilitates the production of functional bile canaliculi along hepatic-cord-like structures[17]. Kidney chip: A simple kidney on a chip that mimics the interface between epithelium and flowing urine was created by bonding a PDMS well and a PDMS channel to either side of a semi-permeable membrane on which cells are cultured and subjected to fluid flow[18]. Lung chip: A lung-on-a-chip capable of replicating mechanical strain caused by breathing, fabricated from PDMS that mimics the physiological function of the alveolar-capillary interface in the human lung. The hollow chambers are subjected to cyclic suction to replicate breathing movements whilst fluid flowing mimics blood flow[19]. Body chip: A microfluidic device containing multiple linked tissue types representing different organs was constructed by sealing three cell culture chambers against a cover. Each cell culture chamber contains a 3D ECM gel containing living cells from a different organ. Media was circulated through the chambers via microfluidic channels during operation[20]. Figure taken from [21]. . . . .	9
2.5	The projection of the two zeeman eigenstates in a spin 1/2 nucleus. . . . .	14
2.6	Energy level and $\Delta E$ of the two energy levels for a spin-1/2 nucleus . . . . .	22
2.7	A) a magnetisation vector precesses in the $xy$ -plane, eventually returning to equilibrium. B) A plot of the magnetisation along $z$ -axis (yellow) and the $x$ -axis (blue) during the relaxation. . . . .	33
2.8	Drawings of the detector assembly and the microfluidic device (1). A: front view (dimensions in mm); B: exploded view. Spacer (4) ensures the alignment of the sample chamber with the constrictions on the PCB planes. In A, PCB plane 5 is hidden to show the orientation of 1 with respect to PCB plane 3. Thickness of each of the PCB planes is 1.52 mm and the copper layers on the PCBs is $35 \mu m$ . Both the microfluidic device and the spacer are made from PMMA and have thickness of 0.9 mm and 1 mm respectively. Figure reproduced from[1] . . . . .	46
2.9	Plot comparing the limits of detection of previously design micro-NMR detectors. Letters a-t correspond to different authors as cited by Badilata <i>et al.</i> [22] Letters u[23] and t[24] represent more recent work. The probe used here is labelled at TLP and a commercial cryoprobe is shown for reference. . . . .	47

3.1	Summary graphic of the work in [25]. This shows how the NMR spectrum of glucose changes in a susceptibility mismatched chip but by cutting shimstructures around the sample chamber high resolution NMR is still possible despite the mismatches. . . . .	54
3.2	Droplet chip design (left) and detail micrograph of the sample chamber area filled with droplets (right). Some droplets are also visible in the entrance and exit channels. . . . .	54
3.3	A: Finite element simulation of relative magnetic field distribution in an uncompensated chip (circular structures filled with PMMA) filled with cyclohexane and B: a compensated chip filled with cyclohexane; C: a linear plot of relative magnetic field along the z-axis through the middle of the sample chamber. . . . .	56
3.4	A: Finite element simulation of magnetic field distribution in droplets. z-component of the reduced magnetic field $H_{\text{red}}$ in an isolated spherical droplet and B: in a face-centred cubic arrangement of droplets; C: FEM mesh used to calculate the result shown in B; D: histograms of the z-component of the reduced magnetic field in the continuous (orange) and in the droplet (blue) phase in the FCC arrangement. . . . .	57
3.5	$^1\text{H}$ NMR line shapes of water (left) and cyclohexane (right) of a water in cyclohexane emulsion as a function of $\text{Eu}[\text{DTPA}]^{2-}$ concentration in the aqueous phase normalised to the sharpest peak. The spectra given in black are the pure phase spectra produced by the same chip. . . . .	58
3.6	Predicted $^1\text{H}$ NMR line shapes of water (left) and cyclohexane (right) of a water in cyclohexane emulsion as a function of $\text{Eu}[\text{DTPA}]^{2-}$ concentration in the aqueous phase. . . . .	59
3.7	Observed line widths of water (blue circles) and cyclohexane (orange circles) in microfluidic droplet emulsions as a function of the $\text{Eu}[\text{DTPA}]^{2-}$ concentration in the aqueous phase. Inset is the plot around the minimum concentration. The widths of both lines are minimal at the matched concentration of 23.75 mM. . . . .	61
3.8	$B_0$ Field maps obtained by magnetic resonance imaging of emulsions with (A) $\Delta\chi = -1.41 \times 10^{-6}$ and (B) $\Delta\chi \approx 0$ . . . . .	61

- 
- 3.9 Spectra of 200 mM Glucose in H<sub>2</sub>O obtained from microfluidic droplet emulsions in cyclohexane. 1: Aqueous phase contains  $c_0 = 23.75 \pm 0.25$  mM Eu[DTPA]<sup>2-</sup>. Spectra 2-7 have been obtained by gradual dilution of the aqueous phase with small amounts of DI water. 2:  $\ln c/c_0 = -0.5\%$ ; 3:  $\ln c/c_0 = -0.75\%$ ; 4 :  $\ln c/c_0 = -0.875\%$ ; 5 :  $\ln c/c_0 = -1.0\%$ ; 6 :  $\ln c/c_0 = -1.125\%$ ; 7 :  $\ln c/c_0 = -1.25\%$ . A spectrum of pure phase 200mM glucose with optimised Eu doping in the same chip is included for comparison (black). The nonuniform peak at 4.8 ppm is due to carrier frequency drift during water suppression . . . . . 64

# List of Tables

2.1	Summary of electrochemical, mechanical and optimal detection technologies employed in microfluidics . . . . .	10
3.1	Bulk magnetic susceptibilities . . . . .	55



# Listings



# Nomenclature

$a$	The signal amplitude
$\mathbb{B}$	The Boltzmann factor
$B_0$	The external magnetic field
$B_1$	The magnetic field produced by an NMR coil
$c_s$	The concentration of spins in a sample
$C$	A constant in SNR
$d$	The coil diameter
$F$	The noise factor from the spectrometer
<b>H</b>	The magnetic field
$h$	Planck's constant
$\hbar$	The reduced Planck constant
$\hat{H}$	The Hamiltonian operator in natural units
$I$	The spin quantum number
$\hat{I}$	The spin angular momentum operator
$i_c$	The current
$J$	The rotational quantum number
$k_0$	A constant that accounts for spatial inhomogeneities in the $B_1$ field
$k_B$	The Boltzmann constant
$l$	The length of a coil
$M_0$	The net magnetisation
$M_a$	The magnetisation vector component along the $a$ -axis
<b>M</b>	The magnetisation
$n_s$	The number of spins in a sample
$\check{\mathbf{n}}$	The surface normal
$p$	The polarisation of a spin system
$P_\alpha$	The population of the $\alpha$ state
$R_{\text{noise}}$	The dissipative loses
$\hat{R}$	The rotation operator $S(t)$
	The signal in the time domain
$S(\Omega)$	The signal in the frequency domain
$T$	The absolute temperature
$T_1$	The longitudinal relaxation time constant

$T_2$	The transverse relaxation time constant
$U$	The scalar magnetic potential
$V_s$	The sample volume
$V'_s$	The product of $k_0$ and $V_s$ that is the volume is within 10% of maximum
$\mathbb{1}$	The identity matrix
$\alpha_F$	The filling factor
$\beta_p$	The tilt of the roatation axis from $z$ for an off-resonance pulse
$\gamma_j$	The gyromagnetic ratio for a nucleus, $j$
$\delta$	The chemical shift
$\delta_{\text{RF}}$	The RF current penetration depth
$\Delta f$	The spectral bandwidth
$\epsilon$	The enhancement factor
$\theta$	The tilt angle of magentisation
$\theta_{\text{RF}}$	The angle between the r.f. coil and $B_0$
$\lambda_l$	The decay constant of a spin $l$
$\mu$	The reduced mass
$\mu_0$	The vacuum permeability
$\hat{\mu}$	magnetic dipole moment operator
$\xi$	The emf
$\rho_r$	The resistivity
$\hat{\rho}$	The density operator
$\sigma$	The chemical shielding factor
$\phi_p$	The phase of an r.f. pulse
$\phi_{\text{ref}}$	The phase shift in the rotating frame
$\Phi$	The angle that connects the static to rotating frame
$\chi_V$	The Magnetic susceptibility
$\omega_j^0$	The larmour frequency for a nucleus, $j$
$\omega_{\text{nut}}$	The nutation frequency
$\omega_{\text{ref}}$	The rotating frame frequency
$\Omega^0$	The difference between the Larmor frequency and rotating frame frequency

## Acknowledgements

I would like to express my deep gratitude to Professor Marcel Utz for his patient guidance and enthusiastic encouragement that he provided as well as engaging discussion concerning all matters of life and work. His depth of knowledge in all manner of subjects was a great help throughout my PhD and provided a seemingly endless source of ideas and problem solving. The principles of scientific investigation I have learnt from him will stay with me throughout my career.

I wish to thank Professor Malcolm Levitt for his support and guidance, the discussions we have had about science helped me to see problems in a different light and increased my effectiveness as a scientist.

I am grateful to my colleagues who have helped me enormously throughout my time in Southampton in no particular order I wish to thank: James Eills, Graeme Finch, Rachel Greenhalgh, Benno Meir, Javier Alonso-Valdesueiro, Karel Kouril, Hana Kourilova, Aliki Moysiadi, Stuart Elliot, Christian Bengs, Manvendra Sharma, Bishnubatra Partra, Matheus Rossetto, Gabriel Rossetto, Marek Plata, Sylwia Ostrowska, Weidong Gong, Mohammed Sabba, George Bacanu, Laurynas Dagys, Jo Collel and Barbara Ripka.

To the people that provided support and encouragement throughout my work and helped me keep sane, I am indebted to Frankie Leeming, Thomas Kear, Laura Jowett, James Eills, Stuart Elliot, Christian Bengs, Aliki Moysiadi, Nic Charles, Judy Fox, Josie Charles, Gemma Charles and Eddie Robinson you all helped immensely.

In particular I'd like to thank Alyssa Charles for her unwavering support, encouragement and belief in me, as well as proof reading and correcting my grammar errors.

Finally, I'd like to thank my family for all their support over the years, this is all possible because of them.



*To my friends and family*



# Chapter 1

## Introduction

Microfluidics is a broad term that covers a wide variety of research, it is characterised by the analysis of small volumes of liquids usually nL to  $\mu$ L, in doing so, it offers numerous benefits such as: a reduction in the materials used in experiments which leads to less cost and less waste; a high level of control over the microenvironment; and ease of parallelisation and automation. Microfluidics chiefly uses Lab-on-a-chip (LoC) devices, or micro total analysis systems ( $\mu$ TAS), to perform experiments. These devices, or systems, are intended for the scaling down of laboratory functions to a chip-format, the sizes of which range from a few mm<sup>2</sup> to a few cm<sup>2</sup>.

Currently, NMR spectroscopy is not widely utilised in microfluidic devices, or experiments, and could be used to provide extra information on the system. It can also be used in conjunction with existing methods of analysis in microfluidics such as fluorescence spectroscopy. As NMR leaves the sample unperturbed, this makes it an ideal candidate for *in situ* monitoring of living systems.

The goal of the work presented here is to incorporate functional microfluidic experiments with high resolution NMR spectroscopy, in such a way that the validity of either section, microfluidic or magnetic resonance, remains intact. In this approach, microfluidic capability is preserved by utilising a design that, whilst constrained by size and shape, has freedom to house a wide variety of chip designs that enable a host of applications, a few of which are shown in Fig. 1.1. This means that functional microfluidics can be performed, and coupled, with high resolution NMR spectroscopy. In this way not only could NMR become a more widely used tool in the microfluidic toolbox, it would also make a valuable attachment to existing tools

High resolution NMR spectroscopy itself requires an extremely homogenous magnetic field, this means that any device capable of combining microfluidics and NMR should seek to preserve the homogeneity. This combination, however, is not without significant challenges. Firstly, a probe capable of  $\mu$ NMR must be designed with comparable performance to existing probes, to maintain validity, and work with existing magnets and

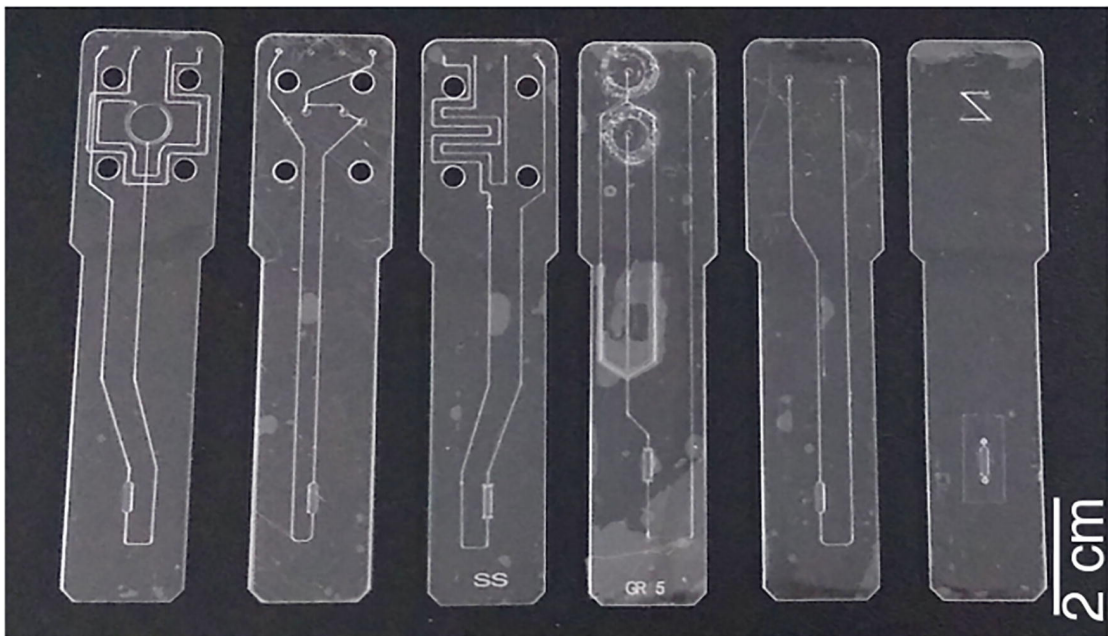


FIGURE 1.1: Microfluidic devices developed for this work, as well as for other applications in microfluidic NMR. From the left: A device for perfusion culture of a tissue slice on chip; capable of peristaltic pumping; hydrogenation on a chip; droplet generation; simple sample chamber filler; 2D/3D cell culture device. Figure taken from [1]

spectrometers. Secondly, the chip, and any functionality it possesses must fit in the bore of the magnet which is typically around 38 mm in diameter. This chip should also couple to the probe in a removable way to enable parallelisation of experiments, preserving one of the key attributes of microfluidics. Thirdly, the materials used in construction should be non-magnetic wherever possible and the use of magnetic parts should be kept to a minimum. When designing experiments, the magnetic susceptibilities of solutions and chip material should also be considered as these need to be as closely matched as possible in order to preserve spectral resolution (a solution for when this isn't the case is discussed in chapter 3).

By combining these two fields, and harnessing the 'best of both worlds' approach new insight and analysis is available. Having quantitative, system-level information in a single or just a few scans could benefit a wide variety of experiments. Enabling microfluidic NMR also provides the opportunity to scan mass-limited samples such as those commonly found in ligand binding reactions[26] or macrocyclic chemistry[27].

# Chapter 2

## Background

### 2.1 Microfluidics

#### 2.1.1 History to present day

The first analytical miniaturised device fabricated on silicon was presented in 1979 by Terry *et al* [28]. This device, was a gas chromatograph capable of separating a simple mixture of gases in seconds and included an injection valve and a 1.5 m long separation column. A thermal conductivity detector was fabricated separately, and clamped to the silicon wafer containing the column. This subsequently allowed for a reduction in size of nearly 3 orders of magnitude compared to the conventional lab equipment at the time, and is regarded [29] as the first demonstration of the power of miniaturisation from which, the field of lab-on-a-chip and microfluidics would be born. Into the 1980s, research related to miniaturisation focused on the fabrication of components, like micropumps [30, 31], and microvalves [32], rather than silicon based analysers.

In 1990, work describing a miniaturised liquid chromatograph on a silicon wafer was published [33]. This work described a 5 x 5 mm chip containing a column and detector that was connected to an off-chip HPLC pump and valves to perform high pressure liquid chromatography. Concurrently, the concept of a 'miniaturised total analysis system' ( $\mu$ TAS) was introduced by Manz *et al* [34], where the incorporation of sample pre-treatment, separation, and detection onto a single device was proposed to enhance the analytical performance of the device rather than to just simply reduce its size. However, it was also recognised that miniaturisation of the device presented the advantages of not only a smaller consumption of materials, but would also enable integration of multiple separation techniques capable of monitoring many components in a single device.

Such a device was envisioned as capable of sample handling, analysis, detection, and incorporating control of mass transport and measurements. Conventional pumps at the

time struggled with the high pressures needed for transport in small channels and early theoretical considerations showed that electroosmotic pumping was an attractive and feasible way to move aqueous liquid through a  $\mu$ TAS especially when separation was needed.

Electroosmosis is defined as the motion of liquid induced by an applied potential. An electroosmotic pump has no moving parts and produces an even flow in the entire length of the channel, ideal for early applications of  $\mu$ TAS that imagined separating and analysing aqueous solutions. Early efforts were first put into optimising injection and separationg by switching voltages between the reservoirs containing reagent, carrier and waste [35].

Electrophoresis in a  $\mu$ TAS was reported in 1992 using silicon and glass [36]. This de-mostrated success in using electroosmotic pumping for flow control in interconnected channels without the use of valves. The concept of integrating injection, separation, and detection was demostrated. As electrophoresis is most commonly used to separate biological samples, usually charged molecules in aqueous solution, it started to be coupled with laser induced fluorescence to detect amino acids separated on-chip [37]. In addition to separation of biological samples, applications of reactions concerning biomolecules and the handlng of cells started to emerge.

Microfabricated devices found uses in DNA amplification by polymerase chain reaction (PCR) [38] and cellular metabolism [39]. As analysis of biological samples in water became available, fabrication of the devices from glass and silicon became unnecessary and inappropriate. Silicon was at the time expensive, but more importantly, opaque to visible and UV-light and so couldn't be used with conventional methods of optical detection frequently used in biology. The increasing complexity of the systems meant it became important for pumps and valves to be integrated into the device these are more easily made from elastomers than rigid materials. The trend towards studying mammalian cells lead to different requirements such as gas permeability which neither glass or silicon can provide. This required replacement of silicon and glass with polymers [40].

Poly(dimethylsiloxane) (PDMS) was the polymer of choice, the properties of which differ greatly from silicon or glass [41, 42]. The switch to PDMS was made even more attractive by the development of soft-lithography as a method for building prototype devices [43] and the development of a method to fabricate pneumatically actuated valves, pumps, and mixers [43]. Thse are only possible due to the elastomeric nature of PDMS and would not be possible with a pure silicon or glass devices. The improved methods of fabrication lead to the developments of the components required for more sophisticated experiments in the form of: valves that enabled immunoassays(Fig. 2.1)[2]; an integrated microfluidic system for efficient mixing [44]; and pumps[45]. With these compnents, microfluidics was

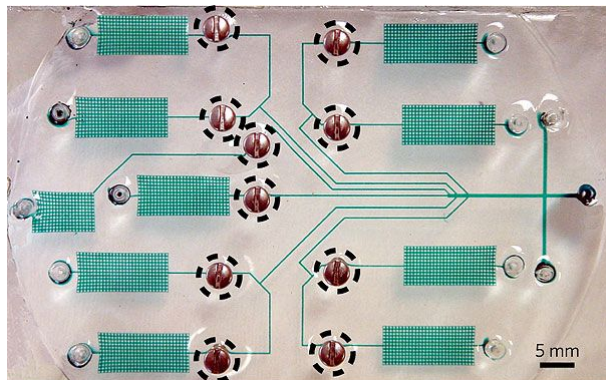


FIGURE 2.1: Components of a microfluidic device got increasingly complicated. This device from Ref.[2] performs immunoassays - widely used in medical and biological research. The screws (dashed circles) are manually operated valves. Water with green dye shows the channels.

in a position to tackle more complex problems one example of the complexity is shown in Fig. 2.1.

As these fabrication methods become more widely used the field of microfluidics moved, from adding components to its analytical arsenal, to starting to find applications for devices. Microfluidic devices then found applications in protein crystallisation [46], separations coupled with mass spectroscopy [47], single cell manipulation [7], and synthesis of <sup>19</sup>F-labelled organic compounds for use in PET scans [48].

A subsection of microfluidics began to emerge around this time too, as low reynolds numbers make multiphase flow manipulation relatively easy, the generation and manipulation of droplets[49, 50, 51] began to be explored. These involved dispersing a liquid phase in a continuous liquid stream to form a monodisperse emulsion of (often) aqueous droplets in oil. These droplets were used to produce polymer particles[52], in making irregular particles[53], hollow microcapsules[54], and protein detection in cells[55]. An example of one of the ways droplets were first produced in microfluidic devices is shown in Fig. 2.2.

In parallel, another branch of microfluidics was being developed. Its goal was to culture cells in a repeatable way. In their normal environment, cells are subject to multiple cues including cytokines and other signalling molecules from neighbouring cells, biochemical interactions with the extracellular matrix, mechanical stress and direct cell to cell contacts. Microfluidics was seen as an ideal method of providing cells with these cues in a controlled and reproducible fashion that couldn't be easily replicated with conventional cell culture, by using microfluidic devices one can combine cell culture with analytical techniques in order to probe the biochemical processes that govern cell behaviour.

Microfluidic devices have been used enable cell-based assays from cell culture to biochemical analysis. In Fig. 2.3 images of different devices are shown that convey how

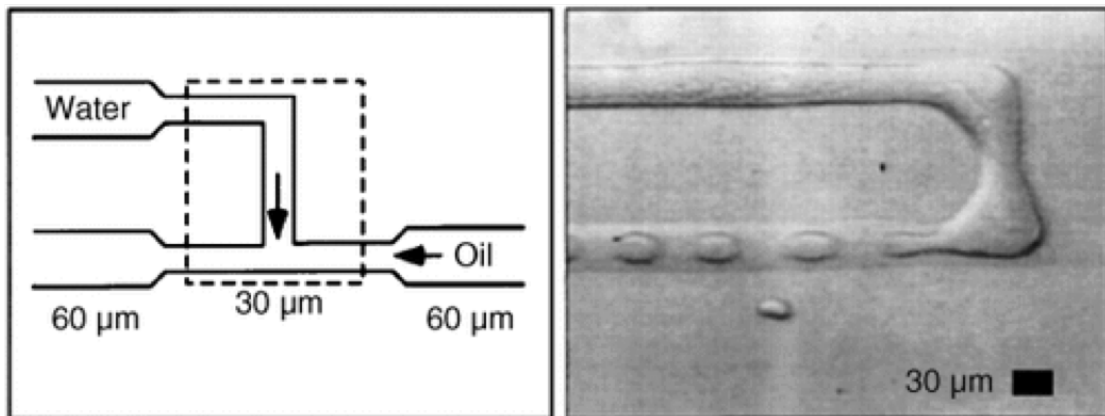


FIGURE 2.2: Formation of droplets in a T-Junction of a microfluidic device the continuous hydrocarbon phase disperses a water phase. Figure from [3]

complex the devices being produced were becoming, despite integration of functionalities proving difficult, these demonstrate the power of miniaturisation and the ingenuity being developed in the field. Microfluidics can offer unique control over cell-cell and soluble cues typical of *in vivo* cell environments by combining microfabrication of 3D extracellular matrix (ECM) structures and fluid networks that can deliver nutrients and oxygen [56].

Throughout the 2000s, microfabrication, which combined micropatterning techniques such as photolithography, photoreactive chemistry, and soft lithography, made it possible to engineer the microenvironment of the cell on similar length scales to the cell itself [57]. This surface patterning of micrometre sized features enabled control of cell-EDM interactions and was used to fabricate 3D scaffolds on which to grow cells that were made of biodegradable materials [58].

One area of application was the 3D culture of liver cells. *In vitro* culture of liver cells is of particular interest as many drugs fail clinical studies because they either damaged the liver directly, or because the metabolites produced by the liver are toxic [59]. Efforts were made to produce *in vitro* culture systems that mimic real liver conditions. In the liver, hepatocytes are found in a complex 3D environment in which nutrients, soluble factors and oxygen are transported through blood capillaries and bile canaliculi. This 3D environment often contains polar tissue structure where two sides of the cell are exposed to different media, for example, in the liver some hepatocytes are exposed to the bile on one side and blood on the other. This polar structure is hard to reproduce using 2D cell culture alone. Using silicon as a substrate, Powers *et al* fabricated 3D liver reactors using array of 300 μm wide channels [60]. In their device they perfused rat liver cells providing fluid shear stresses at physiological range. They found that the cells seeded into the channels rearranged extensively to form 'tissue like' structures and remained viable for up to 2 weeks.

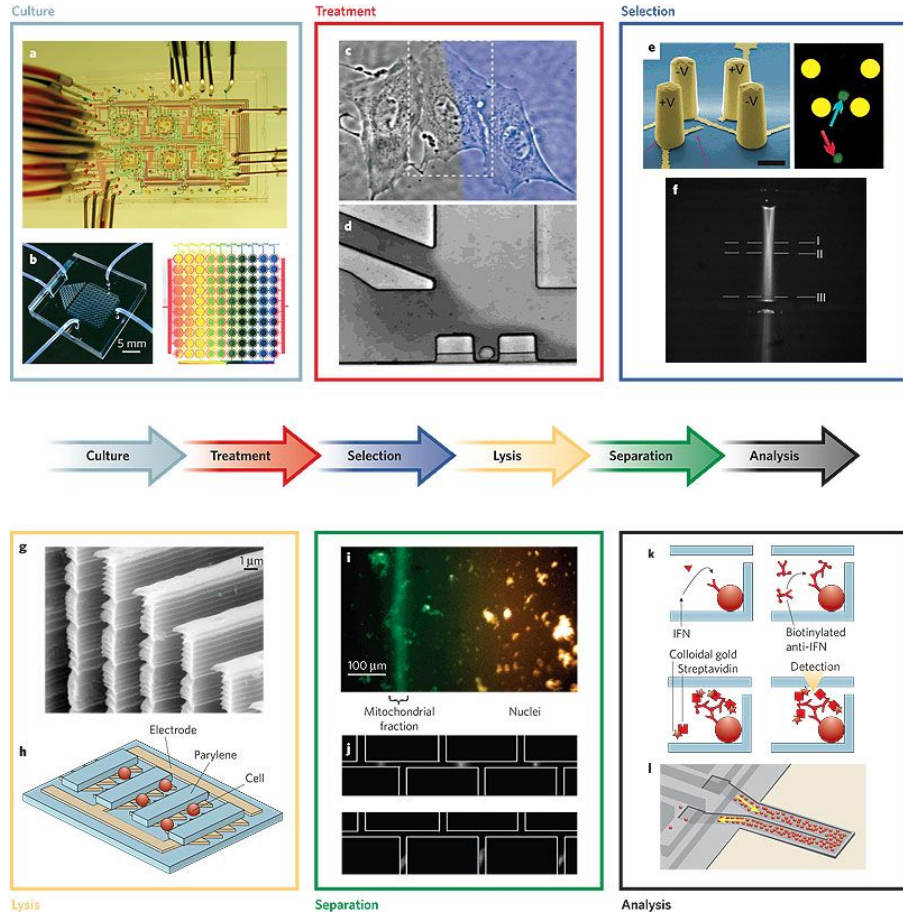


FIGURE 2.3: A collection of microfluidic devices that enabled cell based assays from cell culture, to selection and treatment, to analysis. **a**, Six bioreactors are operated in parallel in a single chip to monitor small numbers of cells [4]. **b**, Microfluidic cell-culture array with integrated concentration gradient generator (left). Image of concentration gradient when blue and yellow dye is used (right) [5]. **c** Two laminar streams exposing two sides of a single cell to different conditions [6]. **d**, Perfusion over a single trapped cell. The perfusion media can be switched in 100 ms [7]. **e**, (left) Cell dielectrophoresis trap. (right) Fluorescent image of trapped cell indicated by blue arrow [8]. **f**, Fluorescent image of light path at the detection zone in a micro flow cytometer [9]. **g** Scanning electron micrograph of a mechanical lysis device with sharp knife-like protrusions [10]. **h**, Schematic of electrical lysis device with microelectrodes [11]. **i**, Isoelectric focusing of cell organelles [12]. **j**, Two-dimensional separation of four model proteins. Isoelectric focusing (top) followed by SDS gel electrophoresis [13]. **k**, Schematic of immunoassay using microbeads as a solid support [14]. **l**, Schematic of a hollow cantilever-mased mass sensor for analyte detection [15]. Taken from Ref.[16]

Later, Sivaraman *et al* developed a different system to culture liver cells in a 3D scaffold, using a polycarbonate housing for a silicon device that contained microfabricated wells in which the cells were seeded and perfused with media. They also found that the cells in the 3D culture also had cell-cell contacts that resembled those found in tissues *in vivo* [59]. It has been observed that co-culture of hepatocytes with other cell types, including liver epithelial cells and Kupffer cells, prolongs the survival of cultured hepatocytes and helps maintain liver-specific properties such as albumin secretion [61].

As 3D cell culture became more widely used, a new subgenre of microfluidics was formed, organ-on-a-chip. Early efforts had shown that microfabrication of adhesive substrates provided well-controlled environments for cell growth and expression of differentiated tissue-specific functions [62, 63]. Advances in soft lithography-based microfluidic devices made it easier to develop the more complex 3D architecture of living tissues and organs. For example, a poly(dimethylsiloxane) (PDMS) device that contained structures that mimic the structure of the endothelial-epithelial interface that forms the liver sinusoid [17].

Along with liver function, kidney, lung, and body functions were replicated in microfluidic devices shown in Fig. 2.4. Whilst the liver and kidney offer highly simplified microengineered models, within organs *in vivo* nutrients, hormones, metabolites, cytokines and physical signals are usually transferred across interfaces between adjacent living cells and therefore require a much more complex microenvironment for true replication. Huh *et al* created a model of the human alveolar-capillary interface formed in a flexible PDMS device containing a central channel and two hollow side chambers [19]. A 10  $\mu\text{m}$  thick PDMS membrane containing an ordered array of micropores (10  $\mu\text{m}$  diameter) was stretched across the central channel, splitting it in two see Fig. 2.4. Human alveolar epithelial cells were then cultured on one side of the membrane and exposed to air, while human lung capillary endothelial cells were cultured on the opposing side and exposed to flowing medium. When the hollow side chambers were exposed to vacuum, the cells were subjected to strain ranging from 5%-15% to match strain observed within whole lung *in vivo*. In doing so, they found their 'lung on a chip' accentuated the inflammatory responses of the cells to silica nanoparticles. This mechanical strain also enhanced uptake of nanoparticles and stimulated the transport into the vascular channel and similar effects of physiological breathing were observed in whole mouse lung. These early organ on chip experiments paved the way for more complex 'Body-on-a-chip' devices that contain multiple types of cultured cells connected by a network of microfluidic channels that permit recirculation and exchange of metabolites in a physiologically-relevant manner [64] and has found applications in drug screening and disease modelling [65].

As the complexity of cell culture within microfluidic devices increased, so to, did the detection methods. Coupling a detector to an LOC is critical for any analytical purpose. A number of detector technologies were demonstrated in microfluidic devices including electrochemical[66], mechanical [67], and optical methods [68]. The small sample

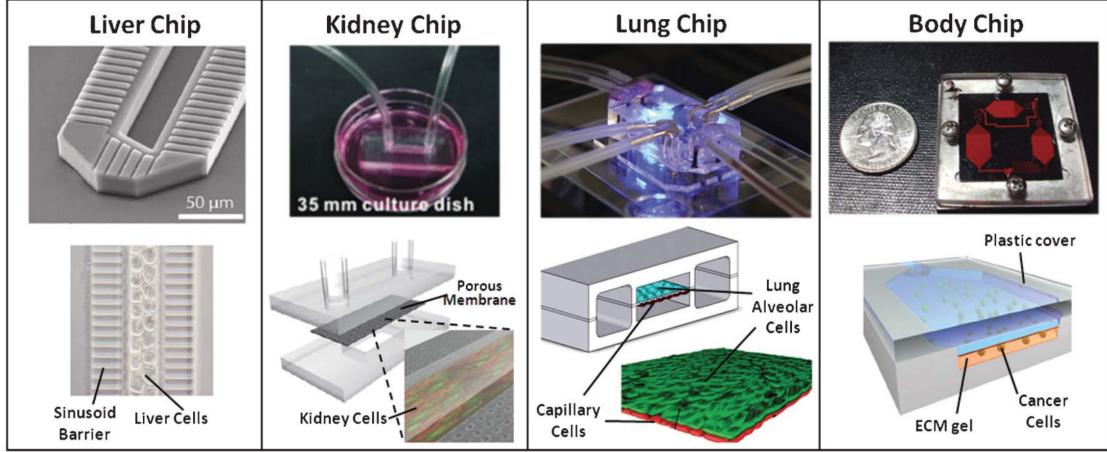


FIGURE 2.4: Organ-Organ and tissue-tissue interfaces in microdevices. Liver chip: A microfluidic liver device with cell culture and flow chambers separated by a baffle that separates cultured hepatocytes from fluid flow to simulate the endothelial-hepatocyte interface of the liver sinusoid. This geometry promotes alignment of hepatocytes in two lines that facilitates the production of functional bile canaliculi along hepatic-cord-like structures[17]. Kidney chip: A simple kidney on a chip that mimics the interface between epithelium and flowing urine was created by bonding a PDMS well and a PDMS channel to either side of a semi-permeable membrane on which cells are cultured and subjected to fluid flow[18]. Lung chip: A lung-on-a-chip capable of replicating mechanical strain caused by breathing, fabricated from PDMS that mimics the physiological function of the alveolar-capillary interface in the human lung. The hollow chambers are subjected to cyclic suction to replicate breathing movements whilst fluid flowing mimics blood flow[19]. Body chip: A microfluidic device containing multiple linked tissue types representing different organs was constructed by sealing three cell culture chambers against a cover. Each cell culture chamber contains a 3D ECM gel containing living cells from a different organ. Media was circulated through the chambers via microfluidic channels during operation[20]. Figure taken from [21].

volumes typical to a microfluidic experiment are an important challenge to overcome for any detector, ideally, a detector should be highly sensitive and scalable to smaller dimensions.

The mechanism and features of the detection technologies summarised in [69] and reproduced in Table 2.1.1.

Method	Mechanism	Features
Electrochemical	Measures changes in conductance, resistance and/or capacitance at the active surface of the electrodes	(+) Real-time detection, (+) Low-cost microelectrode fabrication, (-) Control of ionic concentrations before detection, (-) Short shelf life
Mechanical	Detection is based on variations of the resonant frequency or surface stress of the mechanical sensor	(+) Monolithic sensor integration, (+) Label free detection, (-) damping effects in liquid samples, (-) Detection takes time ( 30 mins), (-) Complex fabrication
Optical	Detects variations in light intensity, refractive index sensitivity, or interference pattern	(+) Minimal sample preparation, (+) Real-time detection, (+) Ubiquitous in laboratories, (-) Conventional instrumentation is expensive, (-) Set-up complexity

TABLE 2.1: Summary of electrochemical, mechanical and optical detection technologies employed in microfluidics.

Electrochemical detection involves the interaction of chemical species with electrodes or probes. This interaction results in a variation of signal, such as potential or current, which enables analysis of target analytes. The electrochemical phenomenon deals with two major effects: (i) chemical reactions are promoted by passing an electrical current through the electrode system; or (ii) electrode responses are triggered due to specific chemical reactions. These effects are usually observed using an electrolytic cell. Reactions of oxidation and reduction occurring at the surface of the electrodes are the basis for electron transfers between the electrolyte (sample) and the electrodes. In a typical electrolytic cell, the electrode system is formed by the working electrode where detection of a certain analyte is analyzed, and the reference electrode where a standard oxidation/reduction is conducted [70]. Wongkaew *et al* reported an electrochemical biosensor that employed microelectrode array. In the array, adjacent electrode fingers form micro-sized gaps which allow an increase of the diffusion flux of chemical species, thus leading to an enhanced collection efficiency and higher signal amplification. The microchannels of the device were made by hot embossing PMMA and the electrodes were made by e-beam and wet-etching processes. The detection of targets using this system took 250 seconds and reported limit of detection of 12.5  $\mu\text{M}$ .

Mechanical detection systems mainly used cantilever technology, which showed that it could be accurate when detecting biomolecules [71]. Cantilever-based devices generally operate in two different modes upon analyte binding: (i) static deflection, where binding on one side of a cantilever causes unbalanced surface stress resulting in a measurable deflection; (ii) dynamic, resonant mode, where binding on a cantilever causes variations

of its mass and consequently shifts the resonant frequency. Mechanical-based detection may require no labelling of biomolecules. Labels often make the detection method more complicated, time-consuming and costly, and could interfere with the function of biomolecules under investigation. Another characteristic of cantilever technology is the potential to fabricate large arrays of sensors for multi-molecular sensing [72]. Hou *et al* [73] presented a device that contained a microfabricated cantilever array for the specific detection of oxytetracycline (OTC), a common broadband antibiotic used in animals that can accumulate in our food chain and cause side effects on humans. The device achieved this by functionalising the cantilevers with OTC specific DNA aptamers which bind to the OTC and increase the load on the cantilevers and causes them to deflect and once calibrated can indicate the concentration of OTC in solution. The limit of detection in this case is 0.2 nM in 1000 seconds.

Optical detection is preferred for robust, sensitive Lab on a chip devices it has been the most widely used technique for quantitative proteomic analysis [74] and infectious disease diagnostics [75], due, in part, to the ubiquity of the optical instrumentation required in biological laboratories meaning these devices can be used readily in most locations. Conventional optical detection methods, including absorbance [76], chemiluminescence [77], fluorescence [78], and surface plasmon resonance (SPR) [79], have all been applied in microfluidic devices. Foudeh *et al* [79] developed an SPR microdevice for the detection of *Legionella pneumophila* which is the pathogenic organism that causes Legionellosis, and is responsible for fatality rates over 10% within hospital and industrial outbreaks [80]. The device is ultra-sensitive to RNA of *Legionella pneumophila* and has a limit of detection of 1 pM in less than 3 hours.

Presently, Microfluidics is a large and diverse field, so much so that the areas that started out as sub-categories are now referred to as their own field of research, indeed, within the last three years the journal Lab on a Chip has published no less than 116 reviews focusing on a wide variety of applications that microfluidics now enjoys such as: 3D printed fluidic networks[81]; droplet microfluidics for synthetic biology[82]; phase behaviour characterization for industrial CO<sub>2</sub>, oil and gas[83]; the production of stem cells using messenger RNAs[84]; and paper microfluidics for diagnosis of malaria in low resource community[85].

## 2.2 NMR theory

### 2.2.0.1 Nuclear Spin

Nuclei have an intrinsic property known as spin. This spin can be represented by operators along the three Cartesian axes  $\hat{I}_x$ ,  $\hat{I}_y$ , and  $\hat{I}_z$  where:

$$\hat{I}_x = -i\hbar(y\frac{\partial}{\partial z} - z\frac{\partial}{\partial y}) \quad (2.1)$$

$$\hat{I}_y = -i\hbar(z\frac{\partial}{\partial x} - x\frac{\partial}{\partial z}) \quad (2.2)$$

$$\hat{I}_z = -i\hbar(x\frac{\partial}{\partial y} - y\frac{\partial}{\partial x}) \quad (2.3)$$

The commutation relation between two operators is defined as:

$$[\hat{A}, \hat{B}] = \hat{A}\hat{B} - \hat{B}\hat{A} \quad (2.4)$$

If  $[\hat{A}, \hat{B}] = 0$  the operators are said to commute. The physical implication of this is that the two observables can be measured at the same time. Measuring one does not affect the outcome of the other and vice versa.

The spin operators  $\hat{I}_x$ ,  $\hat{I}_y$  and  $\hat{I}_z$  have cyclic commutation rules:

$$[\hat{I}_x, \hat{I}_y] = i\hat{I}_z \quad (2.5)$$

$$[\hat{I}_y, \hat{I}_z] = i\hat{I}_x \quad (2.6)$$

$$[\hat{I}_x, \hat{I}_z] = i\hat{I}_y \quad (2.7)$$

This cyclic commutation means that the spin that nuclei posses can be treated as a type of angular momentum and in NMR,  $\hat{I}_x$ ,  $\hat{I}_y$  and  $\hat{I}_z$  are referred to as the spin angular momentum operators.

The total square angular momentum operator,  $\hat{I}^2$  can be defined as:

$$\hat{I}^2 = \hat{I}_x^2 + \hat{I}_y^2 + \hat{I}_z^2 \quad (2.8)$$

This commutes with the three spin angular momentum operators:

$$[\hat{I}^2, \hat{I}_x] = 0 \quad (2.9)$$

$$[\hat{I}^2, \hat{I}_y] = 0 \quad (2.10)$$

$$[\hat{I}^2, \hat{I}_z] = 0 \quad (2.11)$$

Operators act on states. To explain this, consider a generic operator  $\hat{B}$  with eigenstates  $|x\rangle$  and  $|y\rangle$ . When a state is acted upon by an operator it is denoted by:

$$\hat{B}|x\rangle = b|x\rangle \quad (2.12)$$

the same state is returned, multiplied by some scalar  $b$ , that is an eigenvalue of  $|x\rangle$  in the operator basis B.

Analogous to this, spin angular momentum operators have eigenstates and eigenvalues. If the nuclear spin quantum number is  $I$ , then the operator  $\hat{I}_z$  has  $2I + 1$  eigenstates,  $m_I$ . States are denoted  $|I, m_I\rangle$ [86] and the angular momentum operator acts according to the following:

$$\hat{I}_z|I, m_I\rangle = m_I\hbar|I, m_I\rangle \quad (2.13)$$

The total square angular momentum acts in the following way:

$$\hat{I}^2|I, m_I\rangle = I(I+1)\hbar|I, m_I\rangle \quad (2.14)$$

for a nuclear spin state,  $I$  can take half-integer and integer values for zero i.e  $I = 0, \frac{1}{2}, 1, \frac{3}{2} \dots$ ,  $m_I$  takes one of the integer values from  $-I$  to  $+I$ .

### 2.2.0.2 Spin Systems

The simplest case that can be considered in NMR is a system of isolated spin-1/2 nuclei.

According to the quantum theory of angular momentum discussed in 2.2.0.1, a single spin-1/2, when placed in a magnetic field has two eigenstates of angular momentum along the  $z$ -axis, denoted by  $|\alpha\rangle$  and  $|\beta\rangle$  and defined as:

$$|\frac{1}{2}, +\frac{1}{2}\rangle = |\alpha\rangle \quad (2.15)$$

$$|\frac{1}{2}, -\frac{1}{2}\rangle = |\beta\rangle \quad (2.16)$$

The states  $|\alpha\rangle$  and  $|\beta\rangle$  are called the *Zeeman eigenstates* of a spin-1/2 and are acted on by  $\hat{I}_z$  according to the following:

$$\hat{I}_z|\alpha\rangle = +\frac{1}{2}\hbar|\alpha\rangle \quad (2.17)$$

$$\hat{I}_z|\alpha\rangle = -\frac{1}{2}\hbar|\beta\rangle \quad (2.18)$$

Eqn. 2.17 shows that the eigenstate  $|\alpha\rangle$  has an eigenvalue of  $+\hbar/2$  and  $|\beta\rangle$  has an eigenvalue of  $-\hbar/2$  these are said to be polarized along the  $z$ -axis. This polarisation is

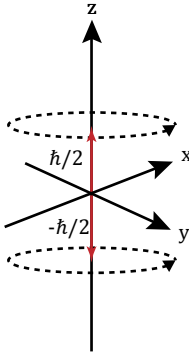


FIGURE 2.5: The projection of the two zeeman eigenstates in a spin 1/2 nucleus.

represented in Fig. 2.5 by the up and down arrows pointing along the positive or negative  $z$ -axis indicating the direction of well-defined spin angular momentum. These arrows should not be overinterpreted as for the same spin, the  $x$  and  $y$  components are fundamentally unpredictable since the states  $|\alpha\rangle$  and  $|\beta\rangle$  are not eigenstates of the operators  $\hat{I}_x$  or  $\hat{I}_y$ . The arrow along the  $z$ -axis does not mean the  $x$ -axis angular momentum is zero. The  $x$ -axis angular momentum is *undefined* as measurements give  $\pm 1/2$  with equal probability and this is very hard to represent in a diagram.

The zeeman eigenstates can be used to define the Zeeman basis. The two kets,  $|\alpha\rangle$  and  $|\beta\rangle$  can be represented by the column vectors:

$$|\alpha\rangle = \begin{pmatrix} 1 \\ 0 \end{pmatrix} \quad |\beta\rangle = \begin{pmatrix} 0 \\ 1 \end{pmatrix} \quad (2.19)$$

as well as kets, bras are also defined by taking the conjugate transpose of the ket,  $|\alpha\rangle^\dagger = \langle\alpha|$  such that

$$\langle\alpha| = (1 \ 0) \quad \langle\beta| = (0 \ 1) \quad (2.20)$$

The state,  $|\psi\rangle$ , of a two level system can now be completely described in this basis as the linear combination of the basis states:

$$|\psi\rangle = c_1 |\alpha\rangle + c_2 |\beta\rangle = \begin{pmatrix} c_1 \\ c_2 \end{pmatrix} \quad (2.21)$$

$$\langle\psi| = c_1^* \langle\alpha| + c_2^* \langle\beta| = (c_1^* \ c_2^*) \quad (2.22)$$

These are normalised such that  $c_1 c_1^* + c_2 c_2^* = 1$ .

To complete the picture, the states must be orthonormal. Orthonormality between states exists if the inner product of the basis states  $|r_i\rangle$  and  $|r_j\rangle$  satisfies the following conditions:

$$\langle r_i | r_j \rangle = \delta_{ij} \quad (2.23)$$

where the Kronecker delta,  $\delta_{ij}$  is:

$$\delta_{ij} = \begin{cases} 0 & \text{if } i \neq j \\ 1 & \text{if } i = j \end{cases} \quad (2.24)$$

where  $\langle r_i | r_j \rangle = \delta_{ij}$  denotes taking the dot product between the two vectors  $|r_i\rangle$  and  $|r_j\rangle$ .

The basis states help to quantify the component of a state vector along that state. Take our example from Eqn. 2.21, we can construct inner products of the overall state,  $|\psi\rangle$  with  $|\alpha\rangle$  and  $|\beta\rangle$  to determine component of the basis states.

$$\langle \alpha | \psi \rangle = c_1 \quad \langle \beta | \psi \rangle = c_2 \quad (2.25)$$

The outer product of the basis state,  $|r_n\rangle$ , for an N-spin system must satisfy:

$$\sum_{n=1}^N |r_n\rangle \langle r_n| = \mathbb{1} \quad (2.26)$$

where  $\mathbb{1}$  is an N by N identity matrix.

When a second spin is introduced, the Hilbert space is extended to accommodate additional spin states by taking the tensor product of the basis states

$$|\alpha_1\alpha_2\rangle = |\alpha_1\rangle \otimes |\alpha_2\rangle = \begin{pmatrix} 1 \\ 0 \\ 0 \\ 0 \end{pmatrix} \quad |\alpha_1\beta_2\rangle = |\alpha_1\rangle \otimes |\beta_2\rangle = \begin{pmatrix} 0 \\ 1 \\ 0 \\ 0 \end{pmatrix} \quad (2.27)$$

$$|\beta_1\alpha_2\rangle = |\beta_1\rangle \otimes |\alpha_2\rangle = \begin{pmatrix} 0 \\ 0 \\ 1 \\ 0 \end{pmatrix} \quad |\beta_1\beta_2\rangle = |\beta_1\rangle \otimes |\beta_2\rangle = \begin{pmatrix} 0 \\ 0 \\ 0 \\ 1 \end{pmatrix} \quad (2.28)$$

The subscripts indicate which spin we are referring to, e.g.  $|\beta_1\alpha_2\rangle$  means that spin 1 is in the  $\beta$  state and spin 2 is in the  $\alpha$  state.

### 2.2.0.3 Pauli matrices and more Operators

In quantum mechanics each observation is associated with a particular operator. For example, the measurement of the spin angular momentum along the  $z$ -axis is associated with  $\hat{I}_z$  and when applied to the  $|\alpha\rangle$  gives the result seen in Eqn. 2.17. The probability of obtaining this result is 1 as  $|\alpha\rangle$  is an eigenstate of  $\hat{I}_z$ . In all other cases the results follow statistical laws and the result of an individual experiment is unpredictable.

In quantum mechanics there is a formula for the average result of very many observations, this is called the expectation value of a general operator,  $\hat{A}$ , when applied to a spin-1/2 system,  $|\psi\rangle$  is denoted:

$$\langle \hat{A} \rangle = \langle \psi | \hat{A} | \psi \rangle \quad (2.29)$$

from the general case listed in Eqn. 2.21 this becomes:

$$\langle \hat{A} \rangle = \langle \psi | \hat{A} | \psi \rangle \quad (2.30)$$

$$= \begin{pmatrix} c_1^* & c_2^* \end{pmatrix} \begin{pmatrix} A_{11} & A_{12} \\ A_{21} & A_{22} \end{pmatrix} \begin{pmatrix} c_1 \\ c_2 \end{pmatrix} \quad (2.31)$$

$$= c_1 c_1^* A_{11} + c_1 c_2^* A_{12} + c_2 c_1^* A_{21} + c_2 c_2^* A_{22} \quad (2.32)$$

The end sum of all these products is the expectation value of a single spin 1/2 particle when acted upon by  $\hat{Q}$ . This quickly becomes cumbersome should there be more than one spin. An easier way to deal with expectation values is described in 2.2.0.4

In NMR we use three operators to determine the projection of angular momentum along a specific axis,  $\hat{I}_x$ ,  $\hat{I}_y$ , and  $\hat{I}_z$ . These are defined by the Pauli matrices in the Zeeman basis multiplied by  $\frac{\hbar}{2}$ .

$$\hat{I}_x = \frac{\hbar}{2} \begin{pmatrix} 0 & 1 \\ 1 & 0 \end{pmatrix} \quad \hat{I}_y = \frac{\hbar}{2i} \begin{pmatrix} 0 & 1 \\ -1 & 0 \end{pmatrix} \quad \hat{I}_z = \frac{\hbar}{2} \begin{pmatrix} 1 & 0 \\ 0 & 1 \end{pmatrix} \quad (2.33)$$

as an example, let's take the example from before of a spin-1/2 particle in a magnetic field and see what happens if we were to project the  $|\alpha\rangle$  state along the z-axis.

$$\hat{I}_z |\alpha\rangle = \frac{\hbar}{2} \begin{pmatrix} 0 & 1 \\ 1 & 0 \end{pmatrix} \begin{pmatrix} 1 \\ 0 \end{pmatrix} = \frac{\hbar}{2} \begin{pmatrix} 1 \\ 0 \end{pmatrix} = \frac{\hbar}{2} |\alpha\rangle \quad (2.34)$$

We find that  $\frac{\hbar}{2}$  is the eigenvalue of  $|\alpha\rangle$  for the operator  $\hat{I}_z$ .

We will now examine three operators and explore how they act on states. They are the total square angular momentum,  $\hat{I}^2$  and the two shift operators  $\hat{I}^+$  and  $\hat{I}^-$  defined as the following:

$$\hat{I}^2 = \hat{I}_x^2 + \hat{I}_y^2 + \hat{I}_z^2 \quad (2.35)$$

$$\hat{I}^+ = \hat{I}_x + i\hat{I}_y \quad (2.36)$$

$$\hat{I}^- = \hat{I}_x - i\hat{I}_y \quad (2.37)$$

They act on general states according to:

$$\hat{I}^2 |I, m_I\rangle = I(I+1)\hbar |I, m_I\rangle \quad (2.38)$$

$$\hat{I}^+ |I, m_I\rangle = \sqrt{(I(I+1) - m_I(m_I+1))} |I, m_{I+1}\rangle \quad (2.39)$$

$$\hat{I}^- |I, m_I\rangle = \sqrt{(I(I+1) - m_I(m_I-1))} |I, m_{I-1}\rangle \quad (2.40)$$

Using a spin-1/2 particle in a magnetic field as an example we'll let these operators act on the  $|\alpha\rangle$  and  $|\beta\rangle$  states

$$\hat{I}^2 |\alpha\rangle = \frac{3}{4}\hbar |\alpha\rangle \quad (2.41)$$

$$\hat{I}^+ |\alpha\rangle = 0 \quad (2.42)$$

$$\hat{I}^- |\alpha\rangle = |\beta\rangle \quad (2.43)$$

$$\hat{I}^+ |\beta\rangle = |\alpha\rangle \quad (2.44)$$

$$\hat{I}^- |\beta\rangle = 0 \quad (2.45)$$

As the '+' and '-' denote raising or lowering  $m_I$  by 1.

As shown in Eqn. 2.5 the three angular momentum operators cyclically commute. This means the *sandwich formula* applies.

In general if  $\hat{A}$ ,  $\hat{B}$  and  $\hat{C}$  cyclically commute then:

$$\exp\{-i\theta\hat{A}\} \hat{B} \exp\{+i\theta\hat{A}\} = \hat{B} \cos\theta + \hat{C} \sin\theta \quad (2.46)$$

geometrically, this can be thought of as a rotation of  $\hat{B}$  by  $\hat{A}$  through an angle  $\theta$ .

It is important to define a set of rotation operators as these are essential for the generation of signal in NMR. They are defined as the complex exponentials of the angular momentum operators seen in 2.2.0.1:

$$\hat{R}_x(\theta) = \exp\{-i\theta\hat{I}_x\} \quad (2.47)$$

$$\hat{R}_y(\theta) = \exp\{-i\theta\hat{I}_y\} \quad (2.48)$$

$$\hat{R}_z(\theta) = \exp\{-i\theta\hat{I}_z\} \quad (2.49)$$

and they too have matrix representations:

$$\hat{R}_x(\theta) = \begin{pmatrix} \cos(\frac{1}{2}\theta) & -i\sin(\frac{1}{2}\theta) \\ -i\sin(\frac{1}{2}\theta) & \cos(\frac{1}{2}\theta) \end{pmatrix} \quad (2.50)$$

$$\hat{R}_y(\theta) = \begin{pmatrix} \cos(\frac{1}{2}\theta) & \sin(\frac{1}{2}\theta) \\ \sin(\frac{1}{2}\theta) & \cos(\frac{1}{2}\theta) \end{pmatrix} \quad (2.51)$$

$$\hat{R}_z(\theta) = \begin{pmatrix} \exp\{-i\frac{1}{2}\theta\} & 0 \\ 0 & \exp\{+i\frac{1}{2}\theta\} \end{pmatrix} \quad (2.52)$$

The rotation operators are applied to the angular momentum operators using the sandwich formula:

$$\hat{R}_x(\theta)\hat{I}_z = \exp\{-i\hat{I}_x\theta\}\hat{I}_z\exp\{+i\hat{I}_x\theta\} \quad (2.53)$$

The result of this is a rotation of  $\hat{I}_z$  around the  $x$ -axis by an angle  $\theta$ :

$$\hat{R}_x(\theta)\hat{I}_z = \cos\theta\hat{I}_z - \sin\theta\hat{I}_y \quad (2.54)$$

The rotational direction (sign of the  $\sin\theta$  term) is determined by the right hand coordinate system defined in Eqn. 2.5.

How each rotational operator transforms the spin angular momentum operators is shown below:

$$\hat{R}_x(\theta) \begin{cases} \hat{I}_x \rightarrow \hat{I}_x \\ \hat{I}_y \rightarrow \hat{I}_y \cos\theta + \hat{I}_z \sin\theta \\ \hat{I}_z \rightarrow \hat{I}_z \cos\theta - \hat{I}_y \sin\theta \end{cases} \quad (2.55)$$

$$\hat{R}_y(\theta) \begin{cases} \hat{I}_x \rightarrow \hat{I}_x \cos\theta - \hat{I}_z \sin\theta \\ \hat{I}_y \rightarrow \hat{I}_y \\ \hat{I}_z \rightarrow \hat{I}_z \cos\theta + \hat{I}_y \sin\theta \end{cases} \quad (2.56)$$

$$\hat{R}_z(\theta) \begin{cases} \hat{I}_x \rightarrow \hat{I}_x \cos\theta + \hat{I}_y \sin\theta \\ \hat{I}_y \rightarrow \hat{I}_y \cos\theta - \hat{I}_x \sin\theta \\ \hat{I}_z \rightarrow \hat{I}_z \end{cases} \quad (2.57)$$

#### 2.2.0.4 Density Operator

In Eqn. 2.30 we saw how the expectation value of an operator can be expressed as the product of the matrix representations of the state and the operator. We can simplify this by constructing a matrix of the quadratic products of the superposition coefficients. If

in the general case

$$|\psi\rangle = \begin{pmatrix} c_1 \\ c_2 \end{pmatrix} = c_1 |\alpha\rangle + c_2 |\beta\rangle \quad (2.58)$$

$$\langle\psi| = \begin{pmatrix} c_1^* & c_2^* \end{pmatrix} = c_1^* \langle\alpha| + c_2^* \langle\beta| \quad (2.59)$$

Then the matrix has the form:

$$|\psi\rangle \langle\psi| = \begin{pmatrix} c_1 c_1^* & c_1 c_2^* \\ c_2 c_1^* & c_2 c_2^* \end{pmatrix} \quad (2.60)$$

The expectation value of the operator  $\hat{A}$  can now be expressed as:

$$\langle\hat{A}\rangle = \text{Tr}\{|\psi\rangle \langle\psi| \hat{A}\} \quad (2.61)$$

If there are now two spins we need to consider with states,  $|\psi_1\rangle$  and  $|\psi_2\rangle$  the result of measuring  $A$  is still uncertain but we can now write an expression for the most likely outcome,  $A_{\text{obs}}$  using the sum of expectation values:

$$A_{\text{obs}} = \langle\psi_1| \hat{A} |\psi_1\rangle + \text{bra}\psi_2 \hat{A} |\psi_2\rangle \quad (2.62)$$

which can be rewritten using the simplification:

$$A_{\text{obs}} = \text{Tr}\{(|\psi_1\rangle \langle\psi_1| + |\psi_2\rangle \langle\psi_2|)\hat{A}\} \quad (2.63)$$

If there are a large number of spin, like in a usual NMR experiemnt we can simplify by defining an operator,  $r\hat{\rho}$ :

$$\hat{\rho} = \mathbb{N}^{-1}(|\psi_1\rangle \langle\psi_1| + |\psi_2\rangle \langle\psi_2| + \dots) \quad (2.64)$$

where  $\mathbb{N}$  is the number of spins in the ensemble. For brevity this is written as:

$$\hat{\rho} = \overline{|\psi\rangle \langle\psi|} \quad (2.65)$$

where the overbar indicates the average over all members of the ensemble.

Now the expectation of  $\hat{A}$  over all memebrs of some spin esemble can now be written as:

$$\langle A \rangle = \text{Tr}\{\hat{\rho}\hat{A}\} \quad (2.66)$$

the operator  $\hat{\rho}$  is referred to as the density matrix.

$$\hat{\rho} = \begin{pmatrix} \overline{c_1 c_1^*} & \overline{c_1 c_2^*} \\ \overline{c_2 c_1^*} & \overline{c_2 c_2^*} \end{pmatrix} = \begin{pmatrix} \rho_\alpha & \rho_+ \\ \rho_- & \rho_\beta \end{pmatrix} \quad (2.67)$$

The diagonal elements of  $\hat{\rho}$ ,  $\rho_\alpha$  and  $\rho_\beta$  are state populations or the probabilities of being in a certain state.

The off-diagonal elements are coherences between states. These coherences represent superposition states in the ensemble the coherences are complex numbers and two coherences between the same pair of states are complex conjugates of each other. e.g.:

$$\langle \alpha | \hat{\rho} | \beta \rangle = (\langle \beta | \hat{\rho} | \alpha \rangle)^* = c_1 c_2^* = (c_1^* c_2)^* \quad (2.68)$$

The coherence order between two states in a magnetic field is defined as the difference in angular momentum projection along the  $z$  axis. In our two spin system this would be:

$$\hat{I}_z |\beta\rangle = m_\alpha = +\frac{1}{2}\hbar |\alpha\rangle \quad (2.69)$$

$$\hat{I}_z |\beta\rangle = m_\beta = -\frac{1}{2}\hbar |\beta\rangle \quad (2.70)$$

We can use these results to calculate the coherence order of the coherence  $\rho_+$ :

$$m_\alpha - m_\beta = +1 \quad (2.71)$$

and conversely the coherence order of  $\rho_-$  is:

$$m_\beta - m_\alpha = -1 \quad (2.72)$$

The density operator can be written as:

$$\hat{\rho} = \rho_\alpha \hat{I}^\alpha + \rho_\beta \hat{I}^\beta + \rho_+ \hat{I}^+ + \rho_- \hat{I}^- \quad (2.73)$$

using the shift operators,  $\hat{I}^+$  and  $\hat{I}^-$ , and the projection operators,  $\hat{I}^\alpha$  and  $\hat{I}^\beta$  these have the following matrix representations:

$$\hat{I}^+ = \begin{pmatrix} 0 & 1 \\ 0 & 0 \end{pmatrix} \quad \hat{I}^- = \begin{pmatrix} 0 & 0 \\ 1 & 0 \end{pmatrix} \quad (2.74)$$

$$\hat{I}^\alpha = \begin{pmatrix} 1 & 0 \\ 0 & 0 \end{pmatrix} \quad \hat{I}^\beta = \begin{pmatrix} 0 & 0 \\ 0 & 1 \end{pmatrix} \quad (2.75)$$

The physical interpretations of the components of the density operator can help to understand the microscopic state of the individual spins. The sum of the populations,  $\rho_\alpha$  and  $\rho_\beta$ , is always equal to one, only the differences between the states have any significance. The difference in population indicates the net longitudinal spin polarization. i.e. if the  $|\alpha\rangle$  state population is larger than the  $|\beta\rangle$  state then there is net polarization of the spins along the external field direction.

The presence of the coherences  $\rho_+$  and  $\rho_-$  indicates transverse spin magnetisation i.e. net spin polarization *perpendicular* to the external field. These coherences are complex numbers and as such have phase and amplitude. The phase of the coherences indicates the direction of the spin polarization in the  $xy$ -plane. The  $(-1)$ -quantum coherence is written as:

$$\rho_- = |\rho_-| \exp\{i\phi_-\} \quad (2.76)$$

and the polarization axis of the spins is:

$$\mathbf{e}'_x \cos \phi_- + \mathbf{e}'_y \sin \phi_- \quad (2.77)$$

These populations and coherences play a vital role in NMR and will be revisited in later sections.

### 2.2.1 The Hamiltonian

The Hamiltonian plays an important part in quantum systems. When the Hamiltonian acts on an eigenstate the eigenvalue returned is the energy level of that state.

#### 2.2.1.1 Spins in a magnetic field

In NMR the energy of a nucleus in a magnetic field,  $E$ , is given by:

$$E = -m_I \hbar \gamma B_0 \quad (2.78)$$

For a spin-1/2 nuclei there are two states labelled as  $\alpha$  and  $\beta$  and these have an energy difference depicted in Fig. 2.6

This splitting of energy levels due to the presence of a magnetic field is referred to as Zeeman splitting. When examining a spin ensemble at thermal equilibrium, overall there is a slight bias to the lower energy state  $\alpha$ . This preference can be quantified by calculating the ratio of the populations,  $P$ :

$$\frac{P_\beta}{P_\alpha} = \exp\left\{-\frac{\Delta E}{k_B T}\right\} \quad (2.79)$$

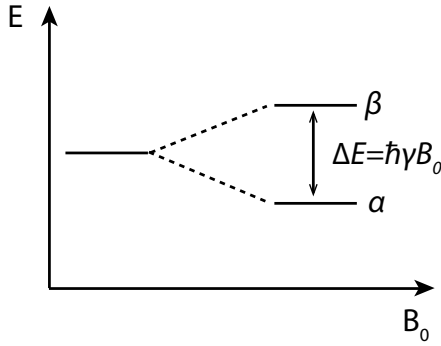


FIGURE 2.6: Energy level and  $\Delta E$  of the two energy levels for a spin-1/2 nucleus

where  $P_\beta/P_\alpha$  is the population ratio between the states,  $k_B$  is Boltzmann constant, and  $T$  is the temperature. The polarisation,  $p$ , of a system of spin-1/2 nuclei is

$$p = \frac{P_\alpha - P_\beta}{P_\alpha + P_\beta} \quad (2.80)$$

For an NMR experiment which typically operates at 298K and a field of 14.1 T the polarisation level is circa  $10^{-5}$  meaning that the spins are aligned weakly in the same direction as the magnetic field. It is this small polarisation that gives rise to the NMR signal and why NMR is famed for sensitivity issues. One possible solution to this, hyperpolarisation, will be described in a later chapter.

When placed in a magnetic field, the nuclei will precess around the axis of the field at a rate known as the larmour frequency defined as:

$$\omega_j^0 = -\gamma_j B_0 \quad (2.81)$$

where  $\gamma_j$  is the gyromagnetic ratio for a nucleus,  $j$ . The gyromagnetic ratio is typically 10s of MHz T<sup>-1</sup> that give larmour frequencies in the 100s of MHz in an NMR experiment.

If we let  $|\psi_1\rangle$  and  $|\psi_2\rangle$  be eigenstates of the Hamiltonian  $\hat{\mathcal{H}}$  then

$$\hat{\mathcal{H}} |\psi_1\rangle = E_1 |\psi_1\rangle \quad (2.82)$$

$$\hat{\mathcal{H}} |\psi_2\rangle = E_2 |\psi_2\rangle \quad (2.83)$$

The Hamiltonian can also be expressed in matrix form:

$$\hat{\mathcal{H}} = \begin{pmatrix} E_1 & 0 \\ 0 & E_2 \end{pmatrix} \quad (2.84)$$

If the Hamiltonian is written in the eigenbasis of the system its main diagonal corresponds to state energies and it has values of 0 everywhere else.

The evolution in time of a quantum system is described by the Schrödinger equation:

$$\frac{d}{dt} |\psi\rangle = i\hbar^{-1} \hat{\mathcal{H}} |\psi\rangle \quad (2.85)$$

the factor of  $\hbar^{-1}$  here is cumbersome and can be removed by defining a Hamiltonian in natural units,  $\hat{H}$  such that:

$$\hat{H} = \hbar^{-1} \hat{\mathcal{H}} \quad (2.86)$$

both Hamiltonians share the same eigenfunctions

$$\hat{H} |\psi_1\rangle = \omega_{\psi_1} |\psi\rangle \quad (2.87)$$

eigenvalues are denoted  $\omega_{\psi}$  and are given by:

$$\omega_{\psi_1} = \hbar^{-1} E_1 \quad (2.88)$$

the eigenvalue,  $\omega_{\psi_1}$ , is the energy of the state  $|\psi\rangle$  in *units* of  $\hbar$ .

Returning to the example of a spin-1/2 particle in a magnetic field. The Hamiltonian is initially proportional to the  $z$  angular momentum operator

$$\hat{H} = \omega^0 \hat{I}_z \quad (2.89)$$

where  $\omega^0 = -\gamma B_0$  and is the Larmor frequency from Eqn. 2.81. In matrix form, in the original zeeman basis, the Hamiltonian is:

$$\hat{H} = \begin{pmatrix} +\frac{\omega}{2} & 0 \\ 0 & -\frac{\omega}{2} \end{pmatrix} \quad (2.90)$$

where

$$\hat{H} |\alpha\rangle = +\frac{\omega}{2} |\alpha\rangle \quad (2.91)$$

### 2.2.2 Spin precession

As discussed when describing Larmor frequency when a spin-1/2 particle is placed in a magnetic field it precesses at the Larmor frequency. In quantum mechanics this precession means that the spin state  $|\psi\rangle$  depends on time.

The law of motion for the spin is the time dependent Schrödinger equation:

$$\frac{d}{dt} |\psi\rangle(t) = -i\hat{H} |\psi\rangle(t) \quad (2.92)$$

The spin Hamiltonian is:

$$\hat{H} = \omega^0 \hat{I}_z \quad (2.93)$$

the equation of motion then becomes:

$$\frac{d}{dt} |\psi\rangle(t) = -i\omega^0 \hat{I}_z |\psi\rangle(t) \quad (2.94)$$

this is a first order differential equation that has the solution:

$$|\psi\rangle(t) = \exp\{-i\omega^0 \Delta t \hat{I}_z\} \psi(t_0) \quad (2.95)$$

where  $t_0$  is the initial time and  $\Delta t$  is the difference in time between  $t_0$  and  $t$ . As the  $\omega^0 \Delta t$  term is angular frequency multiplied by time this simply gives an angle. This shows that it is equal to a rotation about the  $z$ -axis:

$$\hat{R}_z \theta = \exp\{-i\theta \hat{I}_z\} \quad (2.96)$$

The solution therefore to the Schrödinger equation in the absence of rf fields is:

$$|\psi\rangle(t) = \hat{R}_z(\omega^0 \Delta t) |\psi\rangle(t_0) \quad (2.97)$$

In the absence of r.f. fields the Schrödinger equation says that the spin rotates around the  $z$ -axis, through the angle  $\omega_0 \Delta t$

### 2.2.3 Rotating Frame

The field,  $B_0$ , of a regular NMR experiment is many Tesla, giving precession frequencies of hundreds of megahertz. These frequencies correspond to radio frequencies in the electromagnetic spectrum. When considering these precessing spins it can be useful to change from a static frame to a rotating frame of reference.

the static frame of reference axes ( $x$ ,  $y$ , and  $z$ ) and the rotating frame axes ( $x'$ ,  $y'$ , and  $z'$ ) of reference are connected through a time dependent angle,  $\Phi(t)$  such that:

$$x' = x \cos \Phi(t) + y \sin \Phi(t) \quad (2.98)$$

$$y' = y \cos \Phi(t) - x \sin \Phi(t) \quad (2.99)$$

$$z' = z \quad (2.100)$$

The frame rotates with a constant frequency  $\omega_{\text{ref}}$  around the  $z$ -axis:

$$\Phi(t) = \omega_{\text{ref}} t + \phi_{\text{ref}} \quad (2.101)$$

for brevity  $(t)$  is now dropped

If a spin in state  $|\psi\rangle$  has a larmor frequency equal to  $\omega_{\text{ref}}$  then the spin state in the rotating frame,  $|\tilde{\psi}\rangle$  is:

$$|\tilde{\psi}\rangle = \hat{R}_z(-\Phi) |\psi\rangle \quad (2.102)$$

where the tilde denotes a state in the rotating frame.

These of course have an equation of motion:

$$\frac{d}{dt} |\tilde{\psi}\rangle = i\hbar^{-1} \hat{\tilde{H}} |\tilde{\psi}\rangle \quad (2.103)$$

where:

$$\hat{\tilde{H}} = \hat{R}_z(-\Phi) \hat{H} \hat{R}_z(\Phi) - \omega_{\text{ref}} \hat{I}_z \quad (2.104)$$

### 2.2.3.1 Precession in the rotating frame

The spin Hamiltonian in a static field is:

$$\hat{H}^0 = \omega^0 \hat{I}_z \quad (2.105)$$

The rotating fram Hamiltonian is:

$$\hat{\tilde{H}} = \omega^0 \hat{R}_z(-\Phi) \hat{I}_z \hat{R}_z(\Phi) - \omega_{\text{ref}} \hat{I}_z = (\omega^0 - \omega_{\text{ref}}) \hat{I}_z \quad (2.106)$$

The frequency  $\omega^0 - \omega_{\text{ref}}$  is the differenc bwtween the larmor frequency and that of the frame and is denoted,  $\Omega^0$ :

$$\Omega^0 = \omega^0 - \omega_{\text{ref}} \quad (2.107)$$

The rotating-frame spin Hamiltonian in the presence pf a static field, is therefore:

$$\hat{\tilde{H}} = \Omega^0 \hat{I}_z \quad (2.108)$$

### 2.2.4 Radio Frequency Pulses

In NMR 'pulses' are used to manipulate the spin states. These pulses take the form of an oscillating magnetic field applied at a frequency such that it is resonant with the precessing spin. The frequencies correspond to radio frequncies anf the pulses and fields are reffered to as r.f. pulses and r.f. fields.

When an r.f. pulse is applied, the spin experiences two magnetic fields: a static field generated by the magnet; and an oscillating field from the excitation coil. The static field is much larger than the oscillating r.f. field.

The weak r.f. field produces a large effect on the nuclear spin due to it being *resonant* with the precession of that spin. This allows the effect of the weak r.f. field to accumulate as time goes on. If the pulse is applied for long enough, then the weak r.f. field can cause a large change in the spin state. In practice, this corresponds to applying several microseconds of an r.f. pulse which allows for several hundred Larmor precession cycles.

For an r.f. pulse of phase,  $\phi_p$ , applied along the  $x$ -axis, the r.f. field oscillates at the spectrometer resonance frequency,  $\omega_{\text{ref}}$ , and the spin Hamiltonian during the r.f. pulse is given by:

$$\hat{H} = \omega^0 \hat{I}_z + \hat{H}_{\text{RF}} t \quad (2.109)$$

where

$$\hat{H}_{\text{RF}}(t) = -\frac{1}{2}\gamma B_{\text{RF}} \sin \theta_{\text{RF}} \hat{R}_z(\Phi_p) \hat{I}_x \hat{R}_z(-\Phi_p) \quad (2.110)$$

and

$$\Phi_p(t) = \omega_{\text{ref}} t + \phi_p \quad (2.111)$$

The rotating frame Hamiltonian is:

$$\hat{\tilde{H}} = -\frac{1}{2}\gamma B_{\text{RF}} \sin \theta_{\text{RF}} \hat{R}_z(-\Phi + \Phi_p) \hat{I}_x \hat{R}_z(\Phi - \Phi_p) + (\omega^0 - \omega_{\text{ref}}) \hat{I}_z \quad (2.112)$$

$$= -\frac{1}{2}\gamma B_{\text{RF}} \sin \theta_{\text{RF}} \hat{R}_z(-\phi_{\text{ref}} + \phi_p) \hat{I}_x \hat{R}_z(\phi_{\text{ref}} - \phi_p) + \Omega^0 \hat{I}_z \quad (2.113)$$

an additional simplification is possible if we include the value of  $\phi_{\text{ref}}$  which is  $\pi$  for positive  $\gamma$  spins and has the effect of changing the sign of the  $\gamma B_{\text{RF}}$  term:

$$\hat{\tilde{H}} = \omega_{\text{nut}} \hat{R}_z(\phi_p) \hat{I}_x \hat{R}_z(-\phi_p) + \Omega^0 \hat{I}_z \quad (2.114)$$

where  $\omega_{\text{nut}}$  is the nutation frequency:

$$\omega_{\text{nut}} = \left| -\frac{1}{2}\gamma B_{\text{RF}} \sin \theta_{\text{RF}} \right| \quad (2.115)$$

the nutation frequency is the measure of the r.f. field amplitude.

Using the sandwich property again the final form of the rotating-frame Hamiltonian during an r.f. pulse is:

$$\hat{\tilde{H}} = \Omega^0 \hat{I}_z + \omega_{\text{nut}} (\hat{I}_x \cos \phi_p + \hat{I}_y \sin \phi_p) \quad (2.116)$$

#### 2.2.4.1 *x*-pulse

To illustrate the effect an r.f. pulse has on a sample we consider a strong pulse with frequency  $\omega_{\text{ref}}$ , duration  $\tau$ , and phase  $\phi_p = 0$  (an '*x*-pulse'). The amplitude is given by  $\omega_{\text{ref}}$ . We assume this pulse to be applied directly on resonance such that  $\Omega^0 = 0$ .

The rotating frame spin Hamiltonian is:

$$\hat{H} = \omega_{\text{ref}} \hat{I}_x \quad (2.117)$$

the motion of the spin states may be found using the rotating frame Schrödinger equation. If the spin state before the pulse is given by  $|\tilde{\psi}\rangle_1$  and the spin state after the pulse is  $|\tilde{\psi}\rangle_2$  then they are related by:

$$|\tilde{\psi}\rangle_2 = \hat{R}_x(\theta) |\tilde{\psi}\rangle_1 \quad (2.118)$$

where the rotation operator is as defined in Eqn. 2.47 and the angle  $\theta$  is given by

$$\theta = \omega_{\text{nut}} \tau \quad (2.119)$$

this angle is referred to as the *flip angle* of the pulse.

To calculate what effect the pulse has on spins in specific states we can use the matrix representation. A  $(\pi/2)_x$  pulse, which means a flip angle of  $\theta = \pi/2$  and a phase of  $\phi_p = 0$ , applied to spin in the state  $|\alpha\rangle$  can be calculated using the matrix representation of  $\hat{R}_x(\theta)$  as:

$$\hat{R}_x(\pi/2) |\alpha\rangle = \frac{1}{\sqrt{2}} \begin{pmatrix} \cos(\frac{1}{2}\pi/2) & -i \sin(\frac{1}{2}\pi/2) \\ -i \sin(\frac{1}{2}\pi/2) & \cos(\frac{1}{2}\pi/2) \end{pmatrix} \begin{pmatrix} 1 \\ 0 \end{pmatrix} \quad (2.120)$$

$$= \frac{1}{\sqrt{2}} \begin{pmatrix} 1 & -i \\ -i & 1 \end{pmatrix} \begin{pmatrix} 1 \\ 0 \end{pmatrix} \quad (2.121)$$

$$= \frac{1}{\sqrt{2}} \begin{pmatrix} 1 \\ -i \end{pmatrix} = e^{-i\pi/4} \frac{1}{2} \begin{pmatrix} 1+i \\ 1-i \end{pmatrix} = e^{i\pi/4} |-y\rangle \quad (2.122)$$

The pulse transforms the state  $|\alpha\rangle$  into the state  $|-y\rangle$  in other words it has rotated the polarization by  $\pi/2$  around the  $x$ -axis.

#### 2.2.4.2 Pulse of general phase

To understand the significance of the phase of a pulse, consider a pulse exactly on resonance ( $\Omega^0 = 0$ ) with a general phase  $\phi_p$ . The rotating frame spin Hamiltonian is:

$$\hat{H} = \omega_{\text{nut}} (\hat{I}_x \cos \phi_p + \hat{I}_y \sin \phi_p) \quad (2.123)$$

from this, one can see that the effect of the phase shift is to change the axis about which the spin polarizations rotate. The rotation axis is still in the  $xy$ -plane but forms an angle,  $\phi_p$ , with the  $x$  axis. Therefore, a pulse with a phase of  $\pi/2$  rotates the spin polarization around the  $y$ -axis and a phase of  $\pi$  rotates the polarization around the  $-x$ -axis and so on.

The propagator for an on resonance pulse with phase  $\phi_p$  is given by:

$$\hat{R}_{\phi_p}(\theta) = \exp\{-i\omega_{\text{nut}}\tau(\hat{I}_x \cos \phi_p + \hat{I}_y \sin \phi_p)\} \quad (2.124)$$

$$= \exp\{-i\theta(\hat{I}_x \cos \phi_p + \hat{I}_y \sin \phi_p)\} \quad (2.125)$$

this can be rewritten using rotation operators:

$$\hat{R}_{\phi_p}(\theta) = \hat{R}_z(\phi_p)\hat{R}_x(\theta)\hat{R}_z(-\phi_p) \quad (2.126)$$

The matrix representation can be obtained by multiplying together the matrix representations of the rotation operators from Eqn. 2.50:

$$\hat{R}_{\phi_p}(\theta) = \begin{pmatrix} \cos \frac{1}{2}\theta & -i \sin \frac{1}{2}(\theta)e^{-i\phi_p} \\ -i \sin \frac{1}{2}(\theta)e^{+i\phi_p} & \cos \frac{1}{2}\theta \end{pmatrix} \quad (2.127)$$

#### 2.2.4.3 Off-resonance effects

In general, it is not always possible to ensure exact resonance for all spins at the same time, so the condition  $\Omega^0 = 0$  cannot always be satisfied. We can consider the case when  $\Omega^0 \neq 0$  by examining the spin Hamiltonian during a rectangular pulse where:

$$\hat{\tilde{H}} = \Omega^0 \hat{I}_z + \omega_{\text{nut}}(\hat{I}_x \cos \phi_p + \hat{I}_y \sin \phi_p) \quad (2.128)$$

The rotation axis of the spin polarization now has a  $z$ -component as well as an  $x$ - and  $y$ -component. The axis is therefore tilted out of the  $xy$ -plane.

The rotating frame spin Hamiltonian for an off-resonance pulse may be written as:

$$\hat{\tilde{H}} = \omega_{\text{eff}} \cdot \hat{\mathbf{I}} \quad (2.129)$$

where  $\omega_{\text{eff}}$  is the effective rotation axis, given by:

$$\omega_{\text{eff}} = \omega_{\text{eff}} \{ \mathbf{e}'_x \sin \beta_p \cos \phi_p + \mathbf{e}'_y \sin \beta_p \sin \phi_p + \mathbf{e}'_z \cos \beta_p \} \quad (2.130)$$

and  $\{\mathbf{e}'_x, \mathbf{e}'_y, \mathbf{e}'_z\}$  are the rotating reference frame axes. The vector operator  $\hat{\mathbf{I}}$  is defined as:

$$\hat{\mathbf{I}} = \mathbf{e}'_x \hat{I}_x + \mathbf{e}'_y \hat{I}_y + \mathbf{e}'_z \hat{I}_z \quad (2.131)$$

The tilt of the rotation axis away from the  $z$ -axis is:

$$\beta_p = \arctan\left(\frac{\omega_{\text{nut}}}{\Omega^0}\right) \quad (2.132)$$

the magnitude of the rotation frequency around the tilted axis is given by:

$$\omega_{\text{eff}} = \{(\omega_{\text{nut}})^2 + (\Omega^0)^2\}^{1/2} \quad (2.133)$$

Using these parameters the rotating frame spin Hamiltonian may be written as:

$$\hat{H} = \omega_{\text{eff}} \hat{R}_z(\phi_p) \hat{R}_y(\beta_p) \hat{I}_z \hat{R}_y(-\beta_p) \hat{R}_z(-\phi_p) \quad (2.134)$$

The rotating-frame spin states before and after the pulse are related through:

$$|\tilde{\psi}\rangle_2 = \hat{R}_{\text{off}} |\tilde{\psi}\rangle_1 \quad (2.135)$$

where  $\hat{R}_{\text{off}}$  is:

$$\hat{R}_{\text{off}} = \hat{R}_z(\phi_p) \hat{R}_y(\beta_p) \hat{R}_z(\omega_{\text{eff}}\tau) \hat{R}_y(-\beta_p) \hat{R}_z(-\phi_p) \quad (2.136)$$

### 2.2.5 The Density operator revisited

Usually in NMR there are  $> 10^{20}$  spins in the sample, the density operator becomes more advantageous here as mentioned it contains information about the entire spin ensemble. Normally, there is only a small population difference between  $\alpha$  and  $\beta$  governed by the Boltzmann distribution, so for a general polarisation level,  $p$ , the density operator can be written as:

$$\hat{\rho} = \frac{1}{2} \begin{pmatrix} 1+p & 0 \\ 0 & 1-p \end{pmatrix} \quad (2.137)$$

using the definition given in Eqn. 2.34 we can re-write this as

$$\hat{\rho} = \frac{1}{2} \hat{\mathbb{1}} + \frac{1}{2} p \hat{I}_z \quad (2.138)$$

$\hat{\mathbb{1}}$  is identity matrix and corresponds to no population difference between  $|\alpha\rangle$  and  $|\beta\rangle$ .

$\hat{\mathbb{1}}$  is unaffected by rotations so can be ignored in the context of NMR and so we write

$$\hat{\rho} = \frac{1}{2} p \hat{I}_z \quad (2.139)$$

to describe the  $z$  magnetisation of our sample. If the system is at thermal equilibrium then  $p$  is equal to the Boltzmann factor defined as:

$$\mathbb{B} = \frac{\hbar\gamma B_0}{k_b T} \quad (2.140)$$

In NMR we can describe the dynamics of a system using the density operator evolution rather than the evolution of the states using

$$\frac{\partial}{\partial t} |\psi\rangle = -i\hat{H}|\psi\rangle \quad (2.141)$$

$$\frac{\partial}{\partial t} \langle\psi| = i\langle\psi|\hat{H} \quad (2.142)$$

we can derive[87]:

$$\frac{\partial}{\partial t}\hat{\rho} = \frac{\partial}{\partial t}[|\psi\rangle\langle\psi|] \quad (2.143)$$

$$= \left[ \frac{\partial}{\partial t} |\psi\rangle \right] \langle\psi| + |\psi\rangle \left[ \frac{\partial}{\partial t} \langle\psi| \right] \quad (2.144)$$

$$= -i\hat{H}|\psi\rangle\langle\psi| + i|\psi\rangle\langle\psi| \quad (2.145)$$

to give the relationship

$$\frac{\partial}{\partial t}\hat{\rho} = -i[\hat{H}, \hat{\rho}] \quad (2.146)$$

this is called the Liouville von Neumann equation.

The calculation of the response of the spin ensemble to r.f. pulses given the general rotating frame as before the rotating frame density operator is given by:

$$\hat{\tilde{\rho}} = |\tilde{\psi}\rangle\tilde{\langle\psi}| \quad (2.147)$$

The rotating frame and fixed frame populations and coherences are related by:

$$\tilde{\rho}_\alpha = \rho_\alpha \quad \tilde{\rho}_\beta = \rho_\beta \quad (2.148)$$

$$\tilde{\rho}_- = \rho_- \exp\{-i\Phi(t)\} \quad \tilde{\rho}_+ = \rho_+ \exp\{+i\Phi(t)\} \quad (2.149)$$

where

$$\Phi(t) = \omega_{\text{ref}}t + \phi_{\text{ref}} \quad (2.150)$$

the populations remain the same and the coherences are linked through a time dependant phase factor.

### 2.2.5.1 Magnetization vector

The state of a single spin-1/2 can be represented by an arrow indicating the direction of well-defined angular momentum and the response measured by rotating the arrow around the different axes in three dimensional space. Then similarly an ensemble of isolated spins-1/2 can be represented as a magnetization vector,  $\mathbf{M}$ , indicating the magnitude and direction of the net magnetisation. The dynamics of the ensemble corresponds to the motion of the magnetization vector.

The magnetization vector has three Cartesian components:

$$\mathbf{M} = M_x \mathbf{e}_x + M_y \mathbf{e}_y + M_z \mathbf{e}_z \quad (2.151)$$

The longitudinal component is related to the population difference between states:

$$M_z = 2\mathbb{B}^{-1}(\rho_\alpha - \rho_\beta) \quad (2.152)$$

The transverse magnetization components  $M_x$  and  $M_y$  are related to the  $(-1)$ -quantum coherence between the states:

$$M_x = 4\mathbb{B}^{-1} \operatorname{Re}\{\rho_-\} \quad (2.153)$$

$$M_y = 4\mathbb{B}^{-1} \operatorname{Im}\{\rho_-\} \quad (2.154)$$

These are chosen so that thermal equilibrium magnetization is a unit vector along the  $z$ -axis:

$$\mathbf{M}^{\text{eq}} = \mathbf{e}_z \quad (2.155)$$

With these, the density operator may be written as:

$$\hat{\rho} = \frac{1}{2} \mathbb{1} + \frac{1}{2} \mathbb{B} \mathbf{M} \cdot \mathbf{I} \quad (2.156)$$

$$= \frac{1}{2} \mathbb{1} + \frac{1}{2} \mathbb{B} (M_x \hat{I}_x + M_y \hat{I}_y + M_z \hat{I}_z) \quad (2.157)$$

The populations and coherences can be represented in terms of magnetization:

$$\rho_\alpha = \frac{1}{2} + \frac{1}{4} \mathbb{B} M_z \quad \rho_\beta = \frac{1}{2} - \frac{1}{4} \mathbb{B} M_z \quad (2.158)$$

$$\rho_+ = \frac{1}{4} \mathbb{B} (M_x - i M_y) \quad \rho_- = \frac{1}{4} \mathbb{B} (M_x + i M_y) \quad (2.159)$$

### 2.2.5.2 Density operator under pulses

We can use the sandwich equation to calculate the effect of a strong  $(\pi/2)_x$  pulse on an ensemble of spins-1/2 at thermal equilibrium. Before the pulse, the spin density operator is

$$\hat{\rho}_1 = \frac{1}{2} \mathbb{1} + \frac{1}{2} \mathbb{B} \hat{I}_z \quad (2.160)$$

after the pulse the density operator is

$$\begin{aligned} r\hat{\rho}_2 &= \hat{R}_x(\pi/2) \hat{\rho}_1 \hat{R}_x(-\pi/2) = \frac{1}{2} \hat{R}_x(\pi/2) \mathbb{1} \hat{R}_x(-\pi/2) + \frac{1}{2} \mathbb{B} \hat{R}_x(\pi/2) \hat{I}_z \hat{R}_x(-\pi/2) \\ &\quad (2.161) \end{aligned}$$

$$= \frac{1}{2} \mathbb{1} + \frac{1}{2} \mathbb{B} \hat{R}_x(\pi/2) \hat{I}_z \hat{R}_x(-\pi/2) \quad (2.162)$$

since the identity matrix,  $\mathbb{1}$  is invariant under rotations. The last term can be calculated using the sandwich relationship:

$$\hat{R}_x(\pi/2)\hat{I}_z\hat{R}_x(-\pi/2) = -\hat{I}_y \quad (2.163)$$

therefore

$$\hat{\rho}_2 = \frac{1}{2}\mathbb{1} - \frac{1}{2}\mathbb{B}\hat{I}_y \quad (2.164)$$

In terms of the magnetisation vector, this is equivalent to rotating the magnetization from the  $z$ -axis to the  $-y$ -axis.

$$\mathbf{M}_1 = \mathbf{e}_z \xrightarrow{(\pi/2)_x} \mathbf{M}_2 = -\mathbf{e}_y \quad (2.165)$$

To determine what happens to the populations and coherences we can look at the pulse effects in terms of the matrix representation:

$$\hat{\rho}_1 = \begin{pmatrix} \frac{1}{2} + \frac{1}{4}\mathbb{B} & 0 \\ 0 & \frac{1}{2} - \frac{1}{4}\mathbb{B} \end{pmatrix} \xrightarrow{(\pi/2)_x} \begin{pmatrix} \frac{1}{2} & -\frac{1}{4i}\mathbb{B} \\ \frac{1}{4i}\mathbb{B} & \frac{1}{2} \end{pmatrix} \quad (2.166)$$

the pulse accomplishes two things, firstly, the pulse equalizes the populations of the two states and secondly, converts the population difference into coherences.

### 2.2.6 Free evolution with Relaxation

So far, we have only discussed the Hamiltonian and density operator before, during and immediately after an r.f. pulse. This picture is insufficient to describe what one observes experimentally. In terms of populations and coherences, experimentally we find that the populations are not time independent but gradually drift towards their thermal equilibrium values and that the coherences do not last forever but gradually decay to zero.

For populations and coherences there are two forms of relaxation,  $T_1$  and  $T_2$ .  $T_1$  is the longitudinal relaxation time constant and  $T_2$  is the transverse relaxation time constant. The difference between them is demonstrated in Fig. 2.7. Classically  $T_1$  is the rate constant that governs the return of magnetisation to the  $z$ -axis from the  $xy$ -plane.  $T_2$  on the other hand is the time constant that governs the return of magnetisation to equilibrium in the  $xy$ -plane. When talking in terms of the density operator we say that  $T_1$  is the relaxation rate constant for populations, and  $T_2$  is the relaxation rate constant for coherences. But this is incompatible with the classical description of NMR.

The Bloch equations are used to describe how the magnetisation vectors change in time [88]:

$$\frac{dM_x(t)}{dt} = \gamma(M_y(t)B_z(t) - M_z(t)B_y(t)) - \frac{M_x(t)}{T_2} \quad (2.167)$$

$$\frac{dM_y(t)}{dt} = \gamma(M_z(t)B_x(t) - M_x(t)B_z(t)) - \frac{M_y(t)}{T_2} \quad (2.168)$$

$$\frac{dM_z(t)}{dt} = \gamma(M_x(t)B_y(t) - M_y(t)B_x(t)) - \frac{M_z(t) - M_0}{T_1} \quad (2.169)$$

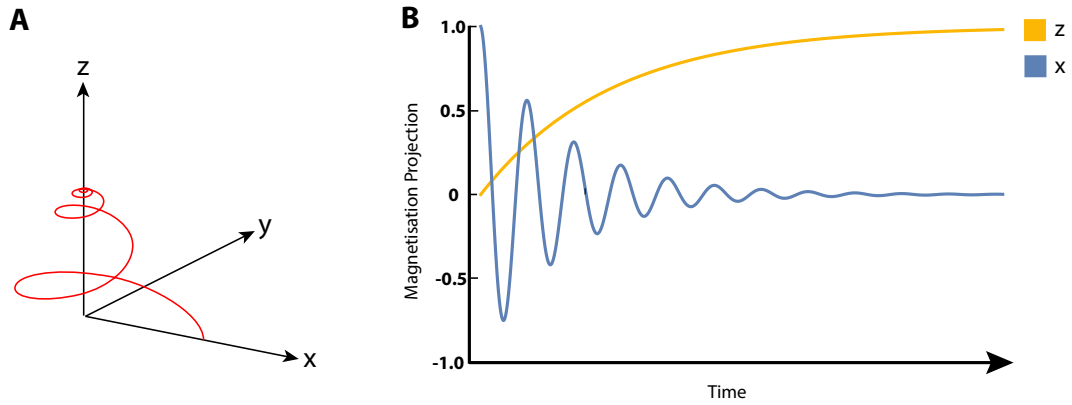


FIGURE 2.7: A) a magnetisation vector precesses in the  $xy$ -plane, eventually returning to equilibrium. B) A plot of the magnetisation along  $z$ -axis (yellow) and the  $x$ -axis (blue) during the relaxation.

#### 2.2.6.1 Transverse relaxation

The coherences decaying to zero is ensured in the equations by introducing an exponential decay term. between time points 2, immediately after an r.f. pulase, and 3 with some delay  $\tau$  the equations for the rotating frame coherences are:

$$\rho_-(3) = \rho_-(2)\exp\{(i\Omega^0 - \lambda)\tau\} \quad (2.170)$$

$$\rho_+(3) = \rho_+(2)\exp\{(-i\Omega^0 - \lambda)\tau\} \quad (2.171)$$

where the damping rate constant  $\lambda$  is given by the inverse of the transverse relaxation time constat  $T_2$ :

$$\lambda = T_2^{-1} \quad (2.172)$$

These equations for coherences correspond to the following substitution rules for the transverse spin angular momentum operators:

$$\hat{I}_x \rightarrow (\hat{I}_x \cos \Omega^0 \tau + \hat{I}_y \sin \Omega^0 \tau) e^{-\lambda \tau} \quad (2.173)$$

$$\hat{I}_y \rightarrow (\hat{I}_y \cos \Omega^0 \tau - \hat{I}_x \sin \Omega^0 \tau) e^{-\lambda \tau} \quad (2.174)$$

For the transverse components of the magnetization vector, the equations are:

$$M_x(3) = M_x(2) \cos \Omega^0 \tau + M_y(2) \sin \Omega^0 \tau e^{-\lambda \tau} \quad (2.175)$$

$$M_y(3) = M_y(2) \cos \Omega^0 \tau - M_x(2) \sin \Omega^0 \tau e^{-\lambda \tau} \quad (2.176)$$

Physically, coherence requires a consistent polarization direction of the spin ensemble. On average all spins experience the same field in a liquid due to motional averaging, however, at any particular instant in time the field are slightly different for different spins locally which cause a gradual loss of synchronization across the ensemble. Coherence decay does increase the entropy of the spin ensemble and is therefore irreversible.

### 2.2.6.2 Longitudinal relaxation

The equations of motion for the populations is a bit more complicated as the populations decay back to their thermal equilibrium values the equations for this are:

$$\rho_\alpha(3) = (\rho_\alpha(2) - \rho_\alpha^{eq}) e^{-\tau/T_1} + \rho_\alpha^{eq} \quad (2.177)$$

$$\rho_\beta(3) = (\rho_\beta(2) - \rho_\beta^{eq}) e^{-\tau/T_1} + \rho_\beta^{eq} \quad (2.178)$$

where the thermal equilibrium populations are:

$$\rho_\alpha^{eq} = \frac{1}{2} + \frac{1}{4} \mathbb{B} \quad \rho_\beta^{eq} = \frac{1}{2} - \frac{1}{4} \mathbb{B} \quad (2.179)$$

The equation of motion for the  $z$ -axis magnetisation vector is:

$$M_z(3) = (M_z(2) - 1) e^{-\tau/T_1} + 1 \quad (2.180)$$

Longitudinal relaxation involves an energy exchange between the spin system and the molecular surroundings and is why it is often referred to as spin-lattice relaxation.

### 2.2.7 NMR signal and detection

In NMR the signal produced by the spins is inductively detected. The precessing transverse magnetization, created when an r.f. field is applied to the sample, induces a voltage, and therefore a current, in a coil that is placed near the sample.

In order to do this, consider a sample containing  $n_s$  number of non-interacting spins-1/2 which have a sample volume,  $V_s$ , and a concentration of spins,  $c_s$ . The total magnetic dipole moment operator in this case is:

$$\hat{\mu} = \hbar\gamma \sum_{k=1}^n \hat{\mathbf{I}}_k \quad (2.181)$$

where  $\hat{\mathbf{I}}_k$  is the spin angular momentum operator for a nucleus  $k$  such that:

$$\hat{\mathbf{I}}_k = (\hat{I}_{kx}\mathbf{e}_x + \hat{I}_{ky}\mathbf{e}_y + \hat{I}_{kz}\mathbf{e}_z) \quad (2.182)$$

The total magnetisation of the sample is given by:

$$\mathbf{M} = \frac{\sum_{k=1}^n \hat{\mu}}{V_s} = \frac{c_s V_s \langle \hat{\mu} \rangle}{V_s} = c_s \langle \hat{\mu} \rangle \quad (2.183)$$

where  $\langle \hat{\mu} \rangle$  is the ensemble average magnetic dipole moment for the sample.

This magnetisation leads to the signal obtained in NMR, to find the relationship we can invoke the principle of reciprocity [89]. Consider the induction field,  $\mathbf{B}_1$ , produced by a coil carrying unit current. For a magnetic dipole,  $\mathbf{m}$ , the induced emf is given by:

$$\xi = -\frac{\partial}{\partial t} \{ \mathbf{B}_1 \cdot \mathbf{m} \} \quad (2.184)$$

where  $\mathbf{B}_1$  is the field produced by the unit current in the wire at  $\mathbf{m}$ . It follows that for our sample after being subjected to a  $(\pi/2)$  pulse, we need only know the value of  $\mathbf{B}_1$  at all points within the sample to be able to calculate the emf induced in the coil if  $\mathbf{M}$  lies in the  $xy$ -plane:

$$\xi = - \int_{\text{sample}} \frac{\partial}{\partial t} \{ \mathbf{B}_1 \cdot \mathbf{M} \} dV_s \quad (2.185)$$

as  $\mathbf{B}_1$  is considered to be homogeneous over the sample volume this gives:

$$\xi = \frac{\partial}{\partial t} \{ \mathbf{B}_1 \cdot \mathbf{M} \} V_s \quad (2.186)$$

we can sub in the result from Eqn. 2.183 to give

$$\xi = \frac{\partial}{\partial t} \{ \mathbf{B}_1 \cdot \langle \hat{\mu} \rangle \} V_s c_s \quad (2.187)$$

if we take the  $B_1$  coil to be aligned along the  $x$ -axis, the  $x$ -axis components contribute to the emf

$$\xi = \frac{\partial}{\partial t} \{B_{1x} \langle \hat{\mu}_x \rangle\} V_s c_s \quad (2.188)$$

using Eqn. 2.181 we get that  $\langle \hat{\mu}_x \rangle = \hbar \gamma \langle \hat{I}_x \rangle$  the emf becomes

$$\xi = \frac{\partial}{\partial t} \{B_{1x} \langle \hat{I}_x \rangle\} V_s c_s \hbar \gamma \quad (2.189)$$

from 2.2.0.4 we find that the ensemble average can be found using the density operator  $\langle \hat{I}_x \rangle = \text{Tr}\{\hat{\rho} \hat{I}_x\}$  so

$$\xi = \frac{\partial}{\partial t} \{B_{1x} [\text{Tr}\{\hat{\rho} \hat{I}_x\}]\} V_s c_s \hbar \gamma \xi = \frac{\partial}{\partial t} \{B_{1x} [\rho_- + \rho_+]\} V_s c_s \hbar \gamma \frac{1}{2} \quad (2.190)$$

all terms apart from the coherences are time independent so the emf can be simplified for now as

$$\xi \sim \frac{\partial}{\partial t} \rho_-(t) + \frac{\partial}{\partial t} \rho_+(t) \quad (2.191)$$

using Eqn. 2.170

$$\rho_-(t) = \rho_-(0) \exp\{(i\omega^0 - \lambda)t\} \quad (2.192)$$

$$\rho_+(t) = \rho_+(0) \exp\{(-i\omega^0 - \lambda)t\} \quad (2.193)$$

the emf becomes

$$\xi \sim (i\omega^0 \rho_- - i\omega^0 \rho_+) \quad (2.194)$$

the signal that one obtains in an NMR experiment is proportional to the emf induced in the pick-up coil this is denoted  $s_{\text{FID}}$  and is given by:

$$s_{\text{FID}} \sim (i\omega^0 \rho_- - i\omega^0 \rho_+) \frac{1}{2} \frac{B_1}{i} \gamma \hbar c_s V_s \quad (2.195)$$

### 2.2.7.1 Quadrature detection

This 'raw' NMR signal oscillates at many hundred megahertz which is too fast for conversion to a digital signal that can be interpreted on a computer. Therefore, it is necessary to down convert the frequency of the NMR signals. This is accomplished by subtracting a frequency that is close to the Larmor frequency, typically, the frequency we subtract is set somewhere in the middle of the spectrum. This frequency is usually generated locally by an r.f. synthesizer and is called the reference frequency and denoted  $\omega_{\text{ref}}$  and has an associated phase  $\phi_{\text{ref}}$

This process of subtraction is carried out by a device called a mixer. The mixer achieves this by multiplying together the two input signals. The signal from the FID is multiplied

by the receiver reference signal:

$$s_{\text{rec}}(t) = \cos(\omega_{\text{ref}}t + \phi_{\text{rec}}) \quad (2.196)$$

the reference signal is split into two parts  $A$  and  $B$  where  $A$  has the same form as above and  $B$  is given an additional phase shift so:

$$s_{\text{rec}}^A(t) = \cos(\omega_{\text{ref}}t + \phi_{\text{rec}}) \quad (2.197)$$

$$s_{\text{rec}}^B(t) = \cos(\omega_{\text{ref}}t + \phi_{\text{rec}} + \pi/2) \quad (2.198)$$

The signal after mixing with  $A$  is:

$$s_{\text{FID}}(t)s_{\text{rec}}^A(t) = (i\omega^0\rho_-(t) - i\omega^0\rho_+(t))\cos(\omega_{\text{ref}}t + \phi_{\text{rec}}) \quad (2.199)$$

which can be evaluated as

$$s_{\text{FID}}(t)s_{\text{rec}}^A(t) = \frac{1}{2}i\rho_-(0)\exp\{i[(\omega^0 + \omega_{\text{ref}})t + \phi_{\text{rec}}]\}e^{-\lambda t} \quad (2.200)$$

$$+ \frac{1}{2}i\rho_-(0)\exp\{i[(\omega^0 - \omega_{\text{ref}})t - \phi_{\text{rec}}]\}e^{-\lambda t} \quad (2.201)$$

$$- \frac{1}{2}i\rho_+(0)\exp\{i[-(\omega^0 - \omega_{\text{ref}})t + \phi_{\text{rec}}]\}e^{-\lambda t} \quad (2.202)$$

$$+ \frac{1}{2}i\rho_+(0)\exp\{i[-(\omega^0 + \omega_{\text{ref}})t - \phi_{\text{rec}}]\}e^{-\lambda t} \quad (2.203)$$

This rather complicated signal is now passed through a low pass r.f. filter which removes the high frequency components this removes the components oscillating at  $\omega^0 + \omega_{\text{ref}}$  and retains the low frequency components  $\Omega^0 = \omega^0 - \omega_{\text{ref}}$  the signal  $s_A(t)$  emerging from the filter is

$$s_A = + \frac{1}{2}i\rho_-(0)\exp\{i(\Omega^0t - \phi_{\text{rec}})\}e^{-\lambda t} \quad (2.204)$$

$$- \frac{1}{2}i\rho_+(0)\exp\{i(-\Omega^0t + \phi_{\text{rec}})\}e^{-\lambda t} \quad (2.205)$$

due to the relationship between laboratory and rotating-frame coherences from Eqn. 2.148 this can be written as

$$s_A = + \frac{1}{2}i\tilde{\rho}_-(0)\exp\{i(\Omega^0t - \phi_{\text{rec}} + \phi_{\text{ref}})\}e^{-\lambda t} \quad (2.206)$$

$$- \frac{1}{2}i\tilde{\rho}_+(0)\exp\{i(-\Omega^0t + \phi_{\text{rec}} - \phi_{\text{ref}})\}e^{-\lambda t} \quad (2.207)$$

where  $\phi_{\text{ref}}$  represents the angle of the rotating frame with respect to the laboratory frame at time  $t = 0$ . The equations for the precession in the rotating frame (Eqn. 2.170) allow for the simplification

$$s_A = + \frac{1}{2}i\tilde{\rho}_-(t)\exp\{-i(\phi_{\text{rec}} - \phi_{\text{ref}})\} - \frac{1}{2}i\tilde{\rho}_+(t)\exp\{i(\phi_{\text{rec}} - \phi_{\text{ref}})\} \quad (2.208)$$

The same arguments can be repeated for the phase shifted signal path  $B$

$$s_B = +\frac{1}{2}\tilde{\rho}_-(t)\exp\{-i(\phi_{\text{rec}} - \phi_{\text{ref}})\} + \frac{1}{2}\tilde{\rho}_+(t)\exp\{i(\phi_{\text{rec}} - \phi_{\text{ref}})\} \quad (2.209)$$

These signals are treated as two components of one complex signal:

$$s(t) = s_A(t) + is_B(t) \quad (2.210)$$

which evaluates to

$$s(t) \sim i\tilde{\rho}_-(t)\exp\{-i(\phi_{\text{rec}} - \phi_{\text{ref}})\} \quad (2.211)$$

Which contains contributions from the rotating frame  $(-1)$ -quantum coherences. The  $(+1)$ -quantum coherences have disappeared however, the contribution is equal to the  $(-1)$ -quantum coherence so a factor two is included the frame phase shift as well as other sources of constant shifts from instrumentation are corrected in post-processing so the quadrature signal can be expressed as:

$$s(t)2i\tilde{\rho}_-(t)\exp\{-i\phi_{\text{rec}}\} \quad (2.212)$$

There are some time independant variables from the original expression of  $s_{\text{FID}}$  which can now be included:

$$s(t) = 2i\omega^0 \frac{1}{2} \frac{B_{1x}}{i_c} \gamma \hbar c_s V_s \tilde{\rho}_-(t) \exp\{-i\phi_{\text{rec}}\} \quad (2.213)$$

$$s(t) = i\omega^0 \frac{B_{1x}}{i_c} \gamma \hbar c_s V_s \tilde{\rho}_-(t) \exp\{-i\phi_{\text{rec}}\} \quad (2.214)$$

where  $\omega^0$  is the larmor frequency,  $B_{1x}/i_c$  is the coil sensitivity,  $\gamma$  is the gyromagnetic ratio,  $\hbar$  is the reduced Planck's constant, the term  $c_s V_s$  is the number of spins in the sample. This signal is still strictly speaking a voltage that produces an osciallting current

### 2.2.7.2 Signal after a pulse

The signal dependence can be seen more clearly if one gets more quantitative, to do this, consider a  $(\pi/2)_x$  pulse with receiver phase,  $\phi_{\text{rec}} = 0$ , for brevity the tilde will be dropped as the rotating frame will be considered. In order to calculate the  $(-1)$ -quantum coherence we must first calculate the density operator. The rotating frame density operator at equilibrium is

$$\hat{\rho}^{eq} = \frac{1}{2}\mathbb{1} + \frac{1}{2}\mathbb{B}\hat{I}_z \quad (2.215)$$

immediately after the pulse at  $t = 0$  the density operator is

$$\hat{\rho}(0) = \frac{1}{2}\mathbb{1} - \frac{1}{2}\mathbb{B}\hat{I}_y \quad (2.216)$$

this can be written in terms of the shift and projection operators:

$$\hat{\rho}(0) = \frac{1}{2}\hat{I}^\alpha + \frac{1}{2}\hat{I}^\beta - \frac{1}{4i}\mathbb{B}\hat{I}^+ + \frac{1}{4i}\mathbb{B}\hat{I}^- \quad (2.217)$$

the  $(-1)$ -quantum coherence is equal to the coefficient of the  $\hat{I}^-$  operator

$$\rho_-(0) = \frac{1}{4i}\mathbb{B} \quad (2.218)$$

the coherence at a time  $t > 0$  is given by:

$$\rho_-(t) = \rho_-(0)\exp\{(i\Omega^0 - \lambda)t\} \quad (2.219)$$

By combining this with the signal equation:

$$s(t) = a\exp\{(i\Omega^0 - \lambda)t\} \quad (2.220)$$

where the signal amplitude  $a$  is

$$a = i\omega^0 \frac{B_{1x}}{i_c} \gamma \hbar c_s V_s \rho_-(0) \exp\{-i\phi_{\text{rec}}\} \quad (2.221)$$

and in the case of the  $(\pi/2)_x$  pulse

$$a = i\omega^0 \frac{B_{1x}}{i_c} \gamma \hbar c_s V_s \frac{1}{4i} \mathbb{B} \quad (2.222)$$

collecting like terms and expanding  $\mathbb{B}$  gives

$$a = \frac{1}{4} \frac{B_{1x}}{i_c} \gamma^3 \hbar^2 B_0^2 \frac{n_s}{k_b T} \quad (2.223)$$

where  $n_s$  is the number of spins in the sample. This relationship makes sense intuitively as increasing the number of spins in your sample leads to an increase in single amplitude as does increasing the coil sensitivity.

### 2.2.7.3 Fourier Transform

After applying an r.f. pulse, the resulting free induction decay (FID) measured is typically an exponentially decaying sinusoidal function. The signal produced from this can be written generally as:

$$S(t) = \sum_l s_l(t) \quad (2.224)$$

$$s_l(t) = a_l \exp\{-(i\omega_l + \lambda_l)t\} \quad (2.225)$$

where  $S(t)$  is the total signal from the sample and  $s_l$  are the signals from the individual spins. Each spin has an amplitude,  $a_l$ , and an associated decay constant,  $\lambda_l = T_2^{-1}$ .

$S(t)$  is easy to evaluate and interpret if it originates from one spin or a group of spins precessing at precisely the same frequency, however, if there are more spins in the sample processing at different frequencies the FID becomes extremely hard to interpret on its own.

We can clear this picture up however by employing a Fourier transform. This converts the time-domain data into the frequency-domain, such that the total signal in the frequency domain,  $S(\Omega)$  is the sum of all individual spin signals resonating at the frequency,  $S_l(\Omega)$ :

$$S(\Omega) = \sum_l S_l(\Omega) \quad (2.226)$$

This allows us to clearly see which resonances are possessed by our spins in the sample. To perform a Fourier transform we must do the following:

$$S_l(\Omega) = \int_0^\infty s_l(t) \exp\{-i\Omega t\} dt \quad (2.227)$$

and using Eqn. 2.224 can be rewritten:

$$S_l(\Omega) = a_l \int_0^\infty \exp\{(-i(\Omega + \Omega_l) + \lambda_l t\} dt \quad (2.228)$$

sometimes written more concisely as:

$$S(\omega) = \mathcal{F}\{S(t)\}(\Omega) \quad (2.229)$$

where  $S(t)$  is the signal for the time domain (FID) and  $S(\omega)$  is the signal in the frequency domain.

The Fourier transform of our general case is:

$$\mathcal{F}\{S(t)\}(\omega) = a_l \frac{1}{\lambda_l + i(\omega - \omega_l)} \quad (2.230)$$

which is Lorentzian function centered at  $\omega_l$  with peak width parameter  $\lambda_l$ .

The NMR signal represented in the frequency domain is a spectrum. It is usually consists of many peaks indicating different resonance frequencies of spins in the sample. In the next section we will discuss chemical shift and J-coupling. Two additional effects that when combined with larmour frequencies already discussed form the NMR spectrum as we know it.

### 2.2.7.4 Chemical Shift and J-coupling

In a molecule, nuclei are surrounded by clouds of electrons which can shield, or de-sheild, it from the effects of the external field  $B_0$ .

The chemical shielding factor,  $\sigma$ , shifts the resonance frequency of the nuclear spin. We can now include it in Eqn. ??:

$$\omega_j^0 = -\gamma_j B_0 (1 - \sigma) \quad (2.231)$$

this chemical shielding is specific to each nuclei position in the molecule. It is possible for two or more nuclei to share the same factor. We refer to these as being chemically equivalent.

The shielding is often around  $10^{-6}$  for  ${}^1\text{H}$ , when plotting and examining spectra it would not be useful to use absolute frequencies, as discussed they are regularly in the hundreds of MHz, whereas the differences in peaks might only be kHz or less. To combat this we use a relative frequency scale called chemical shift,  $\delta$ , defined as:

$$\delta = \frac{\omega_j - \omega_j^{\text{ref}}}{\omega_j^{\text{ref}}} \quad (2.232)$$

where  $\omega_j$  is the precession frequency of the nucleus of interest, and  $\omega_j^{\text{ref}}$  is the precession frequency of a reference nucleus.  $\delta$  is a dimensionless number, unaffected by magnetic field strength, it often small compared to the size of the field and is reported in parts per million (ppm).

In addition to the external  $B_0$  field, the nuclear spins are also affected by the magnetic fields generated by neighboring spins. These magnetic fields are mediated by the electrons in the chemical bonds. This is referred to as spin-spin coupling or  $J$ -coupling and gives rise to peak splittings in spectra. These splittings, and therefore the values of  $J$ -couplings, range from a few Hz to a thousand Hz typically. These become important when considering the Hamiltonian of a multi-spin system but is not discussed in this work.

Both of these,  $\sigma$  and  $J$ -couplings, are tensors this means they depend on the orientation of the molecule and the spin with respect to the magnetic field. In liquids, however, tumble rapidly compared to the timescale of an NMR experiment. This averages the interactions resulting in a scalar quantity for each.

There are additional effects the nuclear spins experience, for example, dipole-dipole coupling which is a through space spin-spin coupling, and quadrupole coupling where there are spins with  $>1/2$  values however, these are not relevant to this work.

## 2.3 Micro-NMR

All NMR experiments depend on two performance metrics: sensitivity and resolution. Sensitivity here means the minimum number of spins needed to give a signal clearly above the noise. Resolution quantifies how well different spins in the sample can be differentiated. These two properties are often linked, by selecting a smaller sample it is possible to enhance resolution by detecting a smaller portion of spins in the sample but this compromises sensitivity as the number of spins become more limited.

In NMR, the long life time of the nuclear spin states (minutes in some cases) contribute to extremely narrow lines in the spectrum with resolutions of one part per billion regularly achieved in commercial systems.

### 2.3.1 Sensitivity

#### 2.3.1.1 Signal to noise ratio

Sensitivity in NMR at thermal equilibrium is always in short supply. In an NMR experiment, the signal amplitude at thermal equilibrium  $a$  can be expressed as:

$$a = \frac{1}{4} \frac{B_{1x}}{i_c} \gamma^3 \hbar^2 B_0^2 \frac{n_s}{k_b T} \quad (2.233)$$

where  $\gamma$  is the gyromagnetic ratio of the nucleus,  $\hbar$  is Planck's constant  $h/2\pi$ ,  $B_0$  is the magnetic field,  $n_s$  is the number of spins in the sample,  $k_B$  is the Boltzmann constant and  $T$  is the absolute temperature. The amplitude of the signal depends on the Boltzmann distribution of population which at room temperature is on the order of  $10^{-25}$  J which is much lower than the thermal energy of the system. From the equation, increasing  $B_0$  would seem a valid strategy and comparatively it can be, increasing from 14.1T to 23.5T can almost triple the signal amplitude, however even at 23.5T there is only a factor of  $6 \times 10^{-6}$  in population difference. It's this very small value that is responsible for the low sensitivity of NMR compared to other techniques.

As mentioned, detection in NMR is typically done through the induction of a voltage in a coil that's close to the precessing nuclear spins this is usually referred to as the sample coil. Unfortunately, this coil also brings with it a type of interference, noise, analogous to the 'hiss' in the background of radio it is produced mainly from thermal motion of electrons in the sample coil with some contribution from thermal motion of ions in solution. The signal to noise ratio, SNR, is an important factor in NMR experiments if its too low the signal will never be seen.

The SNR was formulated by Abragam[90] and the analysis extended by Hoult and Richards[89] and is defined as the peak signal divided by the root mean square (rms)

noise. By including the amplitude from Eqn. 2.233 and using the *Rayleigh-Jeans approximation* for the noise we find:

$$\text{SNR} = \frac{k_0 \frac{1}{4} \frac{B_{1x}}{i_c} \gamma^3 \hbar^2 B_0^2 \frac{n_s}{k_b T_s}}{F \sqrt{4k_b T_c R_{\text{noise}}} \Delta f} \quad (2.234)$$

where  $k_0$  is a factor that accounts for inhomogeneity in the  $B_1$  field,  $n_s$  is the number of spins in the sample,  $\omega_0$  is the larmour frequency. The factor  $B_1/i_c$  the magnetic field from the coil per unit current is defined as the coil sensitivity. The denominator is the noise determined by the noise factor from the spectrometer ( $F$ ) and the dissipative loses ( $R_{\text{noise}}$ ) of the coil, circuit and sample for the spectral bandwidth  $\Delta f$ .  $T_c$  is the absolute temperature of the coil, and  $k_b$  is the boltzmann constant.

In the same paper, Hoult and Richards introduced the principle of reciprocity for calculating the sensitivity of the RF coil, This states that the signal received from a sample by a coil is proportional to the magnetic field which would have been created in the sample if unit current were passed through the coil. Therefore the SNR is directly proportional to the sensitivity of the coil,  $B_1/i$ . This can be seen if we define an effective sample volume that is the volume in which  $B_1$  is within 10% of the maximum value at the center of the coil. The SNR is given by a more simple expression[91]:

$$\text{SNR} = C \frac{B_1 n_s}{i_c \sqrt{R \Delta f}} \quad (2.235)$$

where  $n_s$  is the number of spins in located within an effective volume. For protons at 600MHz the constant,  $C$  equals  $1.4 \times 10^{-11}$  in SI units ( $B_0 = 14.1\text{T}$ ,  $T = 300\text{K}$ ,  $\gamma = 0.2675 \times 10^9 \text{ radT}^{-1}\text{s}^{-1}$ ,  $I = 1/2$  and  $F = 1$  assuming neglige noise from the spectrometer.)

From the simple expression it becomes clear that the way to improve SNR is to increase the filling factor, maximise coil sensitivity,  $B_1/i_c$ , and minimise the total resistance. The filling factor,  $\alpha_F$  is given by:

$$\alpha_F = \frac{\int B_1^2 \rho(r) dV}{\int B_1^2 dV} \quad (2.236)$$

where the function  $\rho$  is unity in the sample area, and zero elsewhere. For a long solenoid coil with the interior space filled with sample,  $\alpha_F = 1/2$ .

Increasing the filling factor and maximising maximise coil sensitivity, can be solved by decreasing the size of the detector. The third, minimising resistance in the coil can be tackled by commercially available cryoprobes where the coil is cooled with a stream of He gas to 20K this reduces the thermal noise from the source and can increase SNR by a factor of four.

To see how size of coil affects SNR we take an RF helical coil. An idealised coil is a cylindrical shell with uniform current density. The RF current penetrates to a frequency

specific depth  $\delta_{RF}$ . For copper at 600 MHz and room temperature  $\delta_{RF} = 2.7 \mu\text{m}$ . The center field is given by:

$$\frac{B_1}{i_c} = \frac{\mu_0}{\sqrt{l^2 + d^2}} \quad (2.237)$$

Resistance is:

$$R = \rho_r \frac{\pi d}{l\delta} \quad (2.238)$$

with  $l$ , the height of the copper cylinder,  $d$  the diameter and  $\rho_r$  the resistivity. Optimum coil sensitivity is given by  $d/l = 1$  in this case the signal to noise is:

$$SNR = 0.9 \times 10^{-16} \frac{N_s}{d\sqrt{\Delta f}} \quad (2.239)$$

For a fixed number of spins the SNR scales with  $1/d$  as predicted by [89]

### 2.3.2 Limit of Detection

The signal to noise ratio can be found in the time or frequency domain. In the time domain the noise,  $N$ , is proportional to  $\sqrt{\Delta f}$ . Therefore the SNR in the time domain is not a good measure of sensitivity, it can be artificially inflated by narrowing the bandwidth. Instead it is better to use *limit of detection*, defined as the number of spins that have to resonate within a bandwidth of 1 Hz to give an SNR of 3. This gives the normalised limit of detection as[22]:

$$nLOD_t = \frac{3n_s}{SNR_t \sqrt{\Delta f}} \quad (2.240)$$

Where  $n_s$  is the number of spins that were present in the sample for the measurement and  $SNR_t$  is the signal to noise ratio in the time domain. In the frequency domain, this becomes

$$nLOD_\omega = \frac{3n_s \sqrt{\Delta t}}{SNR_\omega} \quad (2.241)$$

here,  $\Delta t$  is the effective acquisition time for a single scan given by the inverse of the line broadening applied in the processing of the spectrum.

Practically, NMR relies on signal averaging (see ??) to enhance the spectra. This method requires waiting between scans for the spins to reach thermal equilibrium. In this case, a better measure of sensitivity can be applied by using total measurement time as  $\Delta t$ . The drawback here, is that the limit of detection now depends on instrumentation and sample as  $T_1$  relaxation dictates the experiment repetition rate.

### 2.3.3 Concentration limit of detection

Both types of LOD discussed so far are absolute measures. It is often of more interest to examine the *concentration* limit of detection cLOD. This is given by dividing the LOD by the sample volume:

$$\text{cLOD} = \frac{n\text{LOD}}{V_s} = \frac{\text{nLOD}}{\alpha_f V_c} \quad (2.242)$$

Where  $V_c$  is the volume of the coil and  $\alpha_f$  is the filling factor defined in Eqn. 2.236.

Eqn. 2.234 and Eqn. 2.233 show that overall the SNR and magnetization depend on number of spins and energy level population differences, therefore, best practice would be to wherever possible have higher  $B_0$  to increase population differences and in the case of concentrated limited samples to have a larger volume, increasing the number of spins. One of the major reasons, however, for development of micro-NMR has been the scaling of SNR and therefore LOD with coil size. The trade off here is that as the coil size, and LOD, becomes lower and lower, the volume shrinks too which leads to losses in cLOD. Micro-NMR therefore, only makes sense for mass or volume limited samples.

### 2.3.4 Transmission line probe

This work employs the use of a planar transmission line probe(TLP)[26, 1], in which the geometry differs from that of a classic micro-coil. The design of which is based off early work by van Bentum *et al.* and for an equivalent helix gives  $\sqrt{2}$  larger SNR[91]. The design of the TLP is shown in Fig. 2.8. It works with a generic microfluidic device that has well defined outer geometry and a fixed sample chamber position. The main advantage of using this probe is the compatibility of the device with customisable chips allowing a broad range of applications and enabling the marrying of practical NMR and some microfluidic capabilities which few others allow[24, 92, 93]. The limit of detection LOD for the TLP used is  $1.4 \text{ nmol s}^{1/2}$  which comparitatively lower than detectors of a similar size and more similar to the LOD of commercial cryo-probes mentioned previously. Where the probe is exceptional in terms of micro-detector is the cLOD, this is demonstrated in Fig. 2.9 which shows a wide variety of micro-NMR detectors that have been reported in the literature. Fig. 2.9 has detection volume and mass LOD (nLOD) plotted logarithmically on the  $x$ -axis and  $y$ -axis respectively, the lines of gradient 1 depict lines of constant concentration (cLOD). The general trend of decreasing nLOD with size is indicated with a line of gradient 1/2. The area shaded orange that is defined as the 'metabolomics feasible' range is a maximum  $5 \text{ mM } \sqrt{s}$  ensuring species present at  $0.1 \text{ mM}$  can be detected within less than 20 mins to a sufficient resolution. The TLP has a cLOD of  $1 \text{ mM } \sqrt{s}$  and can detect species at  $0.02 \text{ mM}$  in that time frame. Whilst this is suitable for some metabolomic information to be gained, however, the subtle changes in molecules present at less than  $0.02 \text{ mM}$  are of interest but are unreachable with this probe at this time

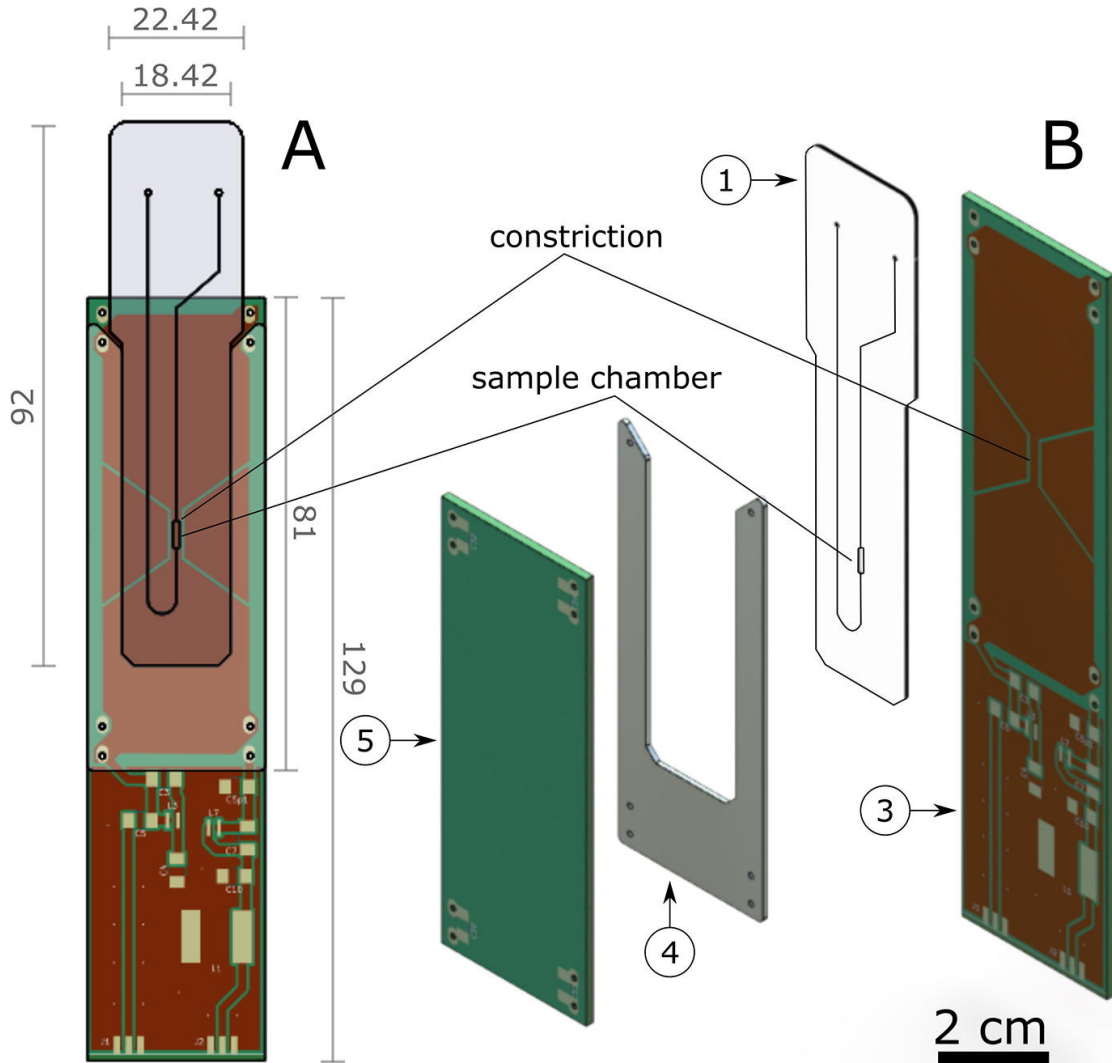


FIGURE 2.8: Drawings of the detector assembly and the microfluidic device (1). A: front view (dimensions in mm); B: exploded view. Spacer (4) ensures the alignment of the sample chamber with the constrictions on the PCB planes. In A, PCB plane 5 is hidden to show the orientation of 1 with respect to PCB plane 3. Thickness of each of the PCB planes is 1.52 mm and the copper layers on the PCBs is  $35 \mu\text{m}$ . Both the microfluidic device and the spacer are made from PMMA and have thickness of 0.9 mm and 1 mm respectively. Figure reproduced from [1]

For this work, the goal is not only to combine NMR detection and microfluidics, clearly that has been done before. However, it is the combination of these two in a way that does not compromise in either. That, in an NMR sense, means nLODs comparable to macroprobes as well as sub 0.01 ppm line widths for true spectral resolution. The main challenge, as in most NMR, is decreasing the limits of detection. Efforts towards lowering the nLOD and cLOD are described in ??

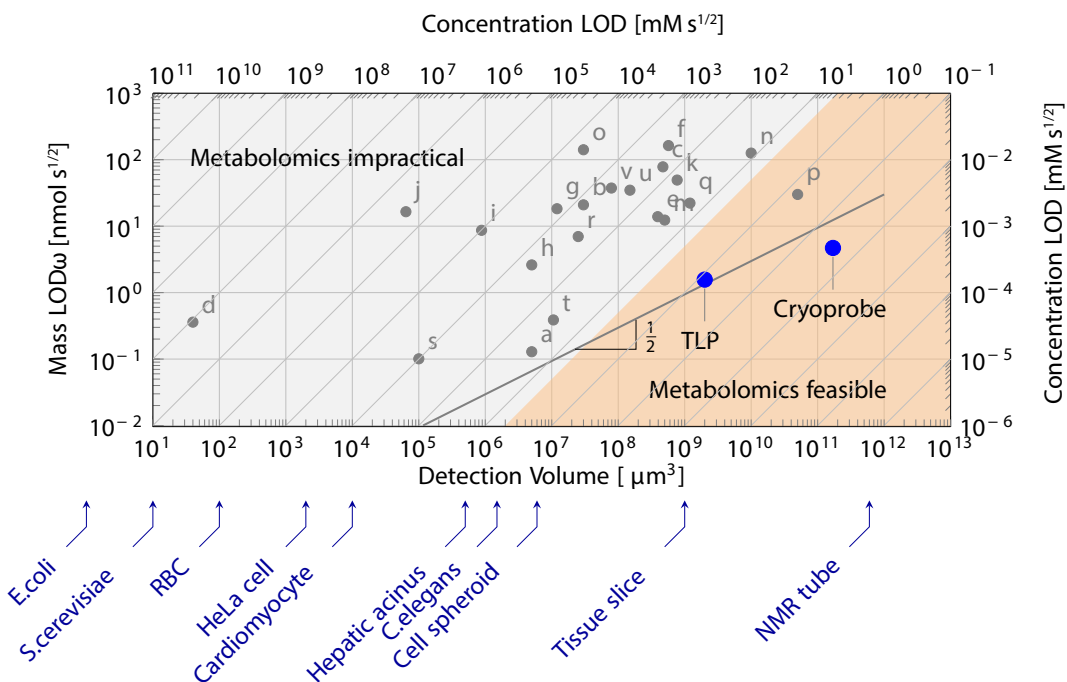


FIGURE 2.9: Plot comparing the limits of detection of previously design micro-NMR detectors. Letters a-t correspond to different authors as cited by Badilita *et al.*[22] Letters u[23] and t[24] represent more recent work. The probe used here is labelled at TLP and a comercial cyroprobe is shown for reference.



## Chapter 3

# Microfluidic Droplet NMR

This chapter is an extended version of Hale. W, Rossetto. G, Greenhalgh. R, Finch. G and Utz. M, High-resolution nuclear magnetic resonance spectroscopy in microfluidic droplets, *Lab Chip*, 2018, **18**, 3018-3024 [94]

### 3.1 Abstract

In this chapter, a system that enables high-resolution NMR spectroscopy of microfluidic droplet emulsions is discussed. Acquiring NMR spectra of emulsions is complicated by the magnetic susceptibility mismatch between the phases and the chip material. In order to overcome these challenges a 2-part solution is needed. Firstly, air-filled structures are incorporated into the microfluidic chip design in order to match the poly(methyl methacrylate) (PMMA) with the continuous phase (cyclohexane) susceptibility. Secondly, a Eu<sup>3+</sup> complex was doped into the dispersed phase (water) in order to match the susceptibility of the phases. High resolution spectra with linewidths of 3Hz were obtained in the ideal case. However, a serial dilution experiment that was used to obtain spectra of glucose droplets showed the highly sensitive dependence of linewidth on Eu concentration.

### 3.2 Introduction

Droplet microfluidics is the field of microfluidic research that separates samples into discrete droplets by dispersing one immiscible fluid (dispersed fluid) in another (continuous fluid). In this way, samples can be manipulated freely in the lab-on-a-chip (LoC) system, and problems due to viscous dispersion and cross-contamination are avoided. In doing so, microdroplets of tunable size and volume, typically femto- to nanolitres, are produced at rates reported to be up to 44 kHz [95]. Thorsen et al [3] reported one of the

first droplet microfluidic devices. In the letter, they show how one can use microfluidic channels to generate mono-disperse microemulsions by shearing water into a perpendicular flow of oil. By varying the ratio of the pressures driving the flow of each fluid they produce droplets that range in diameter from 10  $\mu\text{m}$  to 60  $\mu\text{m}$ .

Droplets have since emerged as a versatile tool finding wide ranging applications in areas such as microcapsule synthesis [96], crystal growth [97], chemical reactions [98], cell/organism encapsulation [99, 100, 101], PCR [102, 103], and Protein studies [104, 105]. These applications are diverse owing to many advantages that microfluidic droplets possess: limited cross contamination; high production rates; large surface area to volume ratio; small reagent volumes; and independent control of each droplet [106].

Droplet generation can, broadly speaking, be divided into two categories. These are active and passive generation methods. Active methods are defined as applying additional force to the device to create droplets such as electric[107], magnetic[108] or centrifugal[109] or by modifying intrinsic forces by tuning fluid velocity[110]. Passive methods rely on the inherent instability of the liquid-liquid interface when mixing two immiscible fluid in order to generate droplets[111, 112, 113]. Zhu and Wang[114] have published an in-depth review of the various methods of droplet generation as well as the equations that govern them.

Here, active droplet generation is used in the form of fluid velocity variation. Two syringe pumps were employed that allowed separate manipulation of flow rates of the dispersed and continuous fluid. The dispersed and continuous phase are co-flowed to the the droplet generation point. By using this method, one can control the production rate and size of the droplets. Droplets of size 100  $\mu\text{m}$  in diameter and a rate suitable enough to fill the sample chamber. If the flow is too fast the droplets have a very low residence time and there is never enough build up to perform an experiment. If, however, the flow is too slow the droplets that are formed are too big and inconsistent for any kind of reliable experimentation.

As discuss in chapter 2, nuclear magnetic resonance (NMR) as a spectroscopic technique has two chief advantages. It is non-invasive and non-destructive which makes it ideally placed to study living systems without destroying them. Indeed, NMR and magnetic resonance imaging (MRI) are both methods actively employed in metabolomics [115], drug discovery [116] and cancer imaging [117]. The nature of NMR means that one can glean quantitative, system level information in one experiment without the need for chemical tags. In a microfluidic context, where fluorescence [118, 119], or mass spec [120, 121], are often the methods of choice for spectroscopy NMR can be used in parallel to these and contribute to a better understanding of the system.

In this work, the possibility to obtain high-resolution NMR spectra from small volumes of droplet emulsions on a chip is explored. Integration of high-resolution NMR spectroscopy with microfluidic systems is challenging for a number of reasons. On the one

hand, small sample volumes place stringent demands on detector sensitivity[22, 122] This has recently been addressed with the design of highly efficient planar NMR micro-coils[123] and transmission line resonators[26] Another challenge is the preservation of high spectral resolution, which depends on a highly homogeneous magnetic field over the sample volume. Differences in magnetic susceptibility between the materials used for the microfluidic chip and the sample fluid, as well as the materials and geometry of the probe assembly, lead to a demagnetising field that varies continuously over the sample volume. Typical diamagnetic volume susceptibilities range from about  $-11$  ppm to about  $-5$  ppm (in SI units);[124, 125] differences of the order of several ppm are therefore commonplace. Unmanaged, they lead to broadening of NMR spectral lines over a ppm or more, which corresponds to a severe loss of resolution in  $^1\text{H}$  liquid state NMR.

Managing susceptibility differences for an emulsion of droplets on a microfluidic chip adds additional complexity, since three different materials are now involved: the chip, the continuous phase, and the droplet phase, all with different susceptibilities. This can be mitigated in a two-step approach, which is based on the observation that most organic solvents in use as continuous phases for droplet microfluidics are less diamagnetic than water. First, the susceptibility difference between the chip and the continuous phase are compensated by shimming structures that are added to the chip design. Then, the susceptibility of the aqueous droplet phase is matched to that of the continuous phase by adding a paramagnetic solute.

### 3.2.1 Susceptibility

Magnetic susceptibility,  $\chi_V$ , is a measure of how much a material will become magnetized in an applied magnetic field, broadly, this allows a classification of most materials as para- ( $\chi > 0$ ) or dia- ( $\chi < 0$ ) magnetic. Materials used in this work are listed in Table 3.1.

The magnetization of the material is given by the equation  $\mathbf{M} = \chi_V \mathbf{H}$  where  $\mathbf{M}$  is the magnetisation of the material and  $\mathbf{H}$  is the magnetic field. In [25], a derivation of how the susceptibility can affect the magnetic field around a sample and influence its spectra is given.

In the absence of currents Ampere's law requires that  $\nabla \times \mathbf{H} = 0$ . The magnetic field  $\mathbf{H}$  can then be expressed by a scalar magnetic potential  $U$  as:

$$\mathbf{H} = -\nabla U \quad (3.1)$$

To describe an object being inserted into a magnetic field we split the potentials as  $U = U_0 + U_d$ , where  $U_0 = H_0 z$  represents the original homogeneous field, and  $\mathbf{H}_d = -\nabla U_d$  is the field generated by the magnetic dipoles induced in the inserted object (sometimes

referred to as demagnetising field). The magnetic field  $H_0$ , which we assume to be along the z-axis, arises from the superconducting coil

The macroscopic magnetic induction  $\mathbf{B}$  is given by:

$$\mathbf{B} = \mu_0(\mathbf{H} + \mathbf{M}) \quad (3.2)$$

where  $\mu_0 = 4\pi \times 10^7 \text{ VsAm}^{-1}$  denotes vacuum permeability. With Gauss' law  $\nabla \cdot \mathbf{B} = 0$  this becomes:

$$\mathbf{B} = \mu_0(-\nabla(U_0 + U_d) + \mathbf{M}) \quad (3.3)$$

$$\nabla \cdot \mathbf{B} = \mu_0(-\nabla^2(U_0 + U_d) + \nabla \cdot \mathbf{M})\nabla^2U_d = \nabla \cdot \mathbf{M} \quad (3.4)$$

We assume that the object consists of a number of spatial domains characterised by a locally constant magnetic susceptibility  $\chi_k$ . The magnetisation therefore, is a piecewise constant,

$$\mathbf{M}_k = \chi_k H_0 \mathbf{e}_z \quad (3.5)$$

the  $\cdot \mathbf{M}$  term from Eqn. 3.3 vanishes everywhere except at domain boundaries. The magnetic field satisfies the boundary conditions[126]

$$(\mathbf{H}_{d2} - \mathbf{H}_{d1}) \times \check{\mathbf{n}} = 0, \quad (3.6)$$

$$(\mathbf{H}_{d2} - \mathbf{H}_{d1}) \cdot \check{\mathbf{n}} = H_0(\chi_2 - \chi_1)\mathbf{e}_z \cdot \check{\mathbf{n}}, \quad (3.7)$$

where  $\check{\mathbf{n}}$  denotes the surface normal from material 1 to material 2. Equations 3.3, 3.6 and 3.7 are formally solved by:

$$U_d(\mathbf{r}) = \frac{H_0}{4\pi} \int_{\delta_{12}} \frac{\check{\mathbf{n}} \cdot \mathbf{e}_z (\chi_2 - \chi_1)}{\sqrt{(\mathbf{r} - \mathbf{r}')^2}} dS, \quad (3.8)$$

where  $dS$  is an infinitesimal surface element, and  $\mathbf{r}'$  is the integration variable. If there are more than two materials involved, as there are in droplets where there are three: the continuous phase; the water phase; and the PMMA, each boundary gives an additive contribution of the same form.

The resonance frequency observed is proportional to the magnetic induction  $\mathbf{B}_{ext}$  experienced by chemically equivalent nuclei within each domain. This induction is determined by the outside field  $H_0$  plus the induced magnetic dipoles of all molecules in the same

domain except the molecule carrying the observed spin.[127] In liquids and isotropic solids, the external magnetic induction differs from the macroscopic  $\mathbf{B}$  as:

$$\mathbf{B}_{ext} - \mathbf{B} = \frac{2\mu_0\chi_s}{3}\mathbf{H}_0 \quad (3.9)$$

The magnetic induction relevant for the Larmor precession of nuclear spins in the sample is therefore

$$\mathbf{B}_{ext} = \mu_0 H_0 \left(1 + \frac{\chi_s}{3}\right) \mathbf{e}_z - \mu_0 \nabla U_d \quad (3.10)$$

Since  $\chi$  is a piecewise constant, the  $\mu_0 \nabla U_d$  term contributes to continuously varying fields and therefore any line broadening seen in the spectrum, whereas the  $\mu_0 H_0 \left(1 + \frac{\chi_s}{3}\right) \mathbf{e}_z$  produces a bulk magnetic susceptibility shift (BMS) of the resonance line.

### 3.2.2 Matching susceptibilities in emulsions

Matching susceptibilities of materials is a problem in microfluidic NMR. Fortunately, the susceptibilities of the materials used are typically similar as in most of our experiments, the solvent is water and the chip material is PMMA.

When the susceptibilities are mismatched, as they are in droplets, this can cause inhomogeneities in the magnetic field, this shifts the resonances and broadens the lines in the spectra rendering them useless. For any kind of useful NMR, the magnetic field needs to be very homogeneous with most commercial superconducting magnets achieving homogeneities of a few parts per billion. In microfluidic devices, air-filled shim structures have been utilised to match susceptibilities between chip construction material and fluid. Utz and co workers[25] have shown that susceptibility mismatches can be compensated for by installing such shim structures around the NMR sensitive region, to produce an equal and opposite demagnetising field to the one caused by the solution, well resolved spectra can be taken of glucose dissolved in the mismatched liquid.

This work, combines both structural shimming and chelated lanthanide doping, to glean high resolution NMR spectroscopy from a microfluidic droplet emulsion. The system is comprised a PMMA chip, an aqueous dispersed phase, and a cyclohexane continuous phase. As mentioned the PMMA and water are susceptibility are quite similar. The cyclohexane, however, is matched to neither. Hence, for all materials and solvents to be matched, structural shimming is employed to match the PMMA to the cyclohexane and a chelated lanthanide  $[\text{Eu(DTPA)}]^{2-}$  will be used to match the water susceptibility.

In emulsions, susceptibility differences between the oil and aqueous phases lead to similar line broadening[124] NMR spectroscopy is extensively used to characterise emulsion droplet size distributions using pulsed field gradient methods[128, 129, 130, 131, 132, 133,

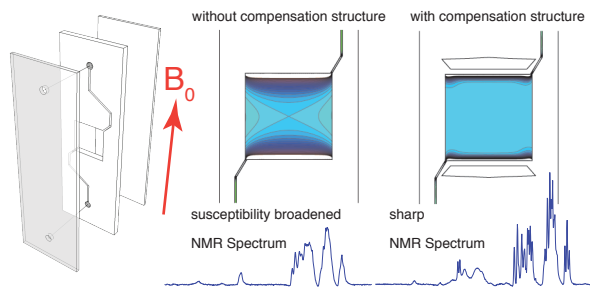


FIGURE 3.1: Summary graphic of the work in [25]. This shows how the NMR spectrum of glucose changes in a susceptibility mismatched chip but by cutting shim structures around the sample chamber high resolution NMR is still possible despite the mismatches.

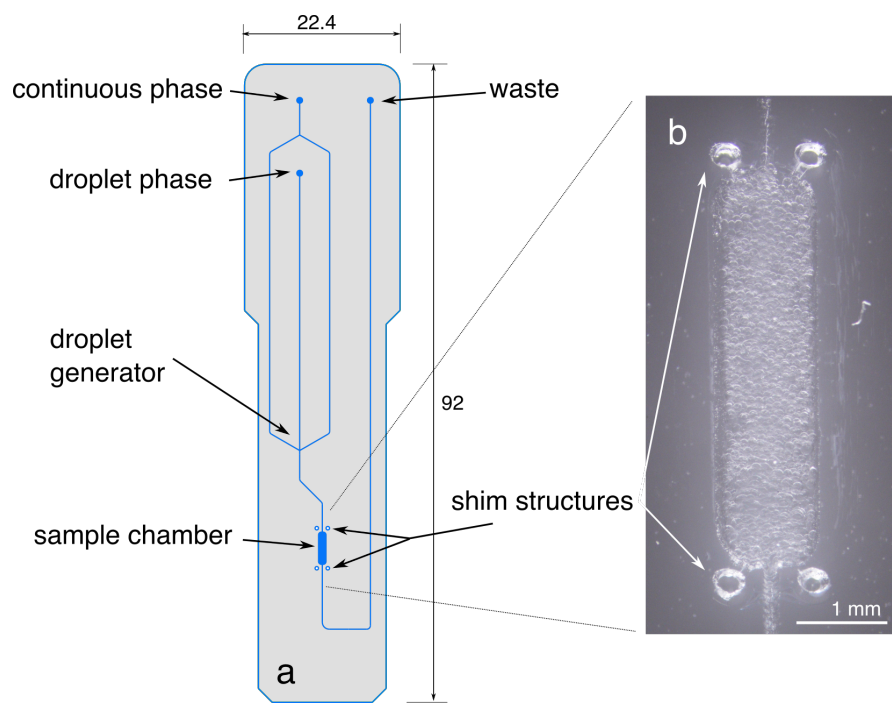


FIGURE 3.2: Droplet chip design (left) and detail micrograph of the sample chamber area filled with droplets (right). Some droplets are also visible in the entrance and exit channels.

[134]. These methods do not require spectral resolution of individual compounds other than the two solvents, and are therefore unaffected by the susceptibility broadening. By contrast, high-resolution NMR spectroscopy, with sufficient resolution to distinguish multiple compounds present in either of the two phases, requires careful mitigation of the susceptibility differences. It has also been shown that susceptibility differences can be compensated for in a liquid sample by doping of a chelated lanthanide[135] For example, Lennon *et al.* demonstrated that the susceptibility mismatch between the inside and outside of deoxygenated red blood cells could be compensated for by doping 3mM of dysprosium tripolyphosphate  $[Dy(PPP)_2]^{7-}$  into the extracellular fluid[136]

It should be noted that in principle, the same effect could be achieved if a diamagnetic

TABLE 3.1: Bulk magnetic susceptibilities

Compound	$\chi_V/10^{-6}$ (SI)	Ref
water	-9.05	[138]
cyclohexane	-7.640	[138]
PMMA	-9.01	[139]
Air	+0.36	[140]

dopant could be added to the continuous phase. However, while paramagnetic dopants are easily available in the form of transition metal ions, no effective diamagnetic dopants exist in the literature.

$\text{Eu}^{3+}$  complexes are paramagnetic, and are frequently used as shift agents in NMR spectroscopy. Unlike other lanthanide ions such as  $\text{Gd}^{3+}$  or  $\text{Ho}^{3+}$ , which are powerful nuclear relaxation agents,  $\text{Eu}^{3+}$  has only a minimal effect on nuclear magnetic relaxation due to its extremely short electron spin-lattice relaxation time[137]. Addition of millimolar quantities of  $\text{Eu}^{3+}$  to aqueous solutions therefore does not cause significant relaxation line broadening, but changes the bulk magnetic susceptibility of the solution proportionally to the  $\text{Eu}^{3+}$  concentration. It is therefore possible to adjust the susceptibility difference in a droplet emulsion by adding a  $\text{Eu}^{3+}$  complex that selectively dissolves in (or at least strongly partitions to) the aqueous phase.

In the present work, the diethyl-triamine pentaacetate (DTPA) complex of  $\text{Eu}^{3+}$ ,  $\text{Eu}[\text{DTPA}]^{2-}$  is used. As an ion species, it is readily soluble in aqueous media, while exhibiting only negligible solubility in apolar organic solvents. Microfluidic chips are fabricated from poly methyl methacrylate (PMMA). By a fortunate coincidence, the susceptibilities of PMMA and water are very close to each other (Table 3.1). NMR lines in microfluidic devices made from PMMA are therefore narrow if aqueous samples are used, provided that the boundaries of the chip and the environment are either aligned with the external magnetic field, or are kept sufficiently remote from the detection area. By contrast, most organic solvents are considerably less diamagnetic than water, as exemplified by the case of cyclohexane, which has been used in the present study.

In the remainder of this chapter, finite element calculations are used to estimate the NMR line widths expected in a droplet emulsion depending on the susceptibility mismatch. The results are then compared to experimental line widths obtained with varying concentrations of  $\text{Eu}[\text{DTPA}]^{2-}$  in the aqueous phase. Finally, narrow NMR lines are obtained by combining structural shimming[141] with susceptibility matching, and demonstrate that this approach can be used to obtain a high resolution of glucose contained within the compensated droplets. The chip used in this work is shown in Fig. 3.2. It consists of a sample chamber in the centre of the chip, which is designed to line up with the sensitive area of a transmission-line micro-NMR detector,[26] and a convergent flow droplet generator. The aqueous phase and the continuous phase are fed into the

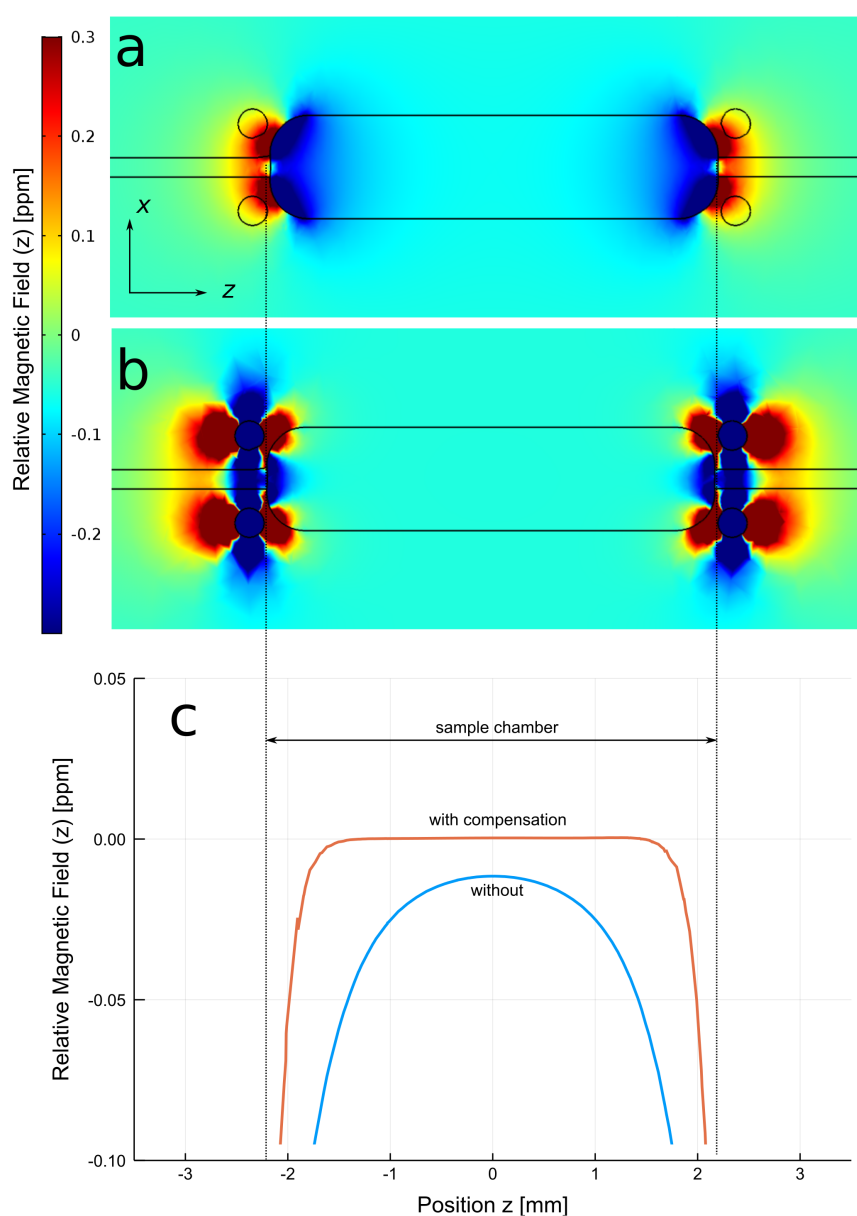


FIGURE 3.3: A: Finite element simulation of relative magnetic field distribution in an uncompensated chip (circular structures filled with PMMA) filled with cyclohexane and B: a compensated chip filled with cyclohexane; C: a linear plot of relative magnetic field along the z-axis through the middle of the sample chamber.

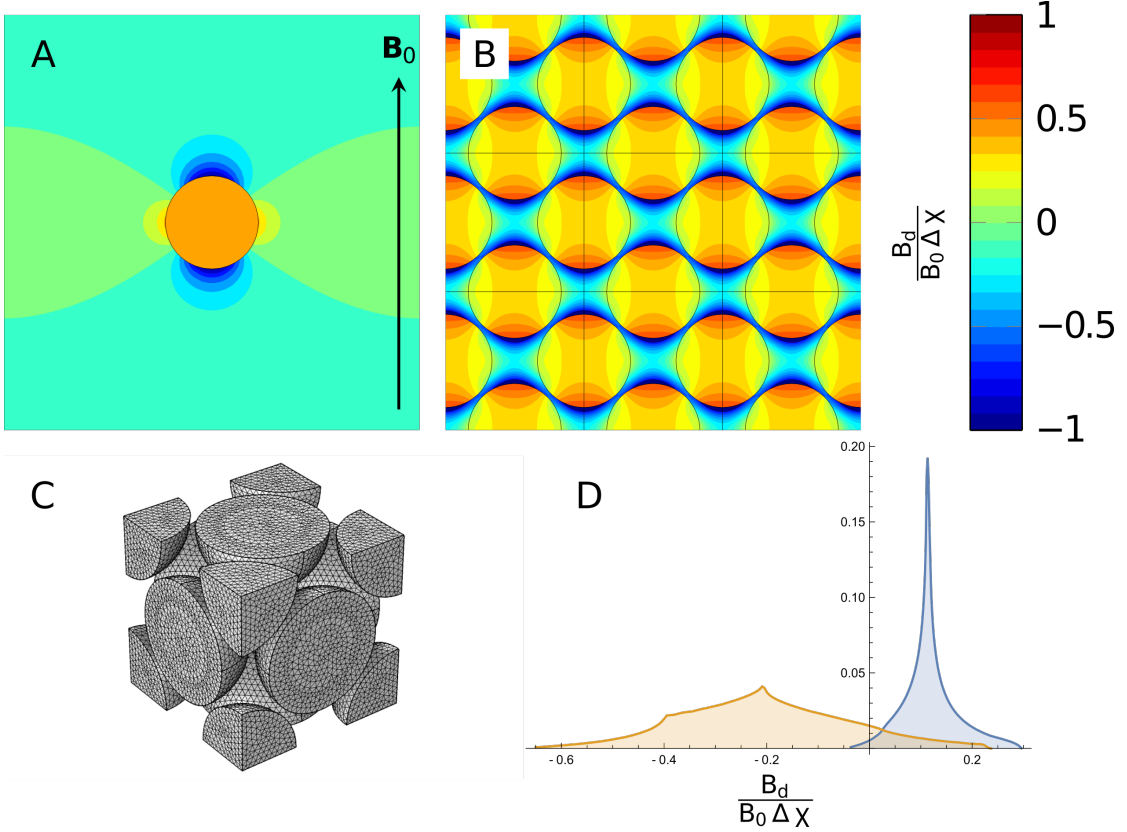


FIGURE 3.4: A: Finite element simulation of magnetic field distribution in droplets.  $z$ -component of the reduced magnetic field  $H_{\text{red}}$  in an isolated spherical droplet and B: in a face-centred cubic arrangement of droplets; C: FEM mesh used to calculate the result shown in B; D: histograms of the  $z$ -component of the reduced magnetic field in the continuous (orange) and in the droplet (blue) phase in the FCC arrangement.

two ports at the top. Droplets are formed and transported downstream into the sample chamber. The chamber is surrounded by four shim structures, which are circular shaped cutouts filled with air. They have been designed to compensate for the difference in susceptibility between the chip material (PMMA) and the oil phase (cyclohexane) as shown in Fig. 3.3. The operation of the chip is shown on the right side of Fig. 3.2; droplets of about  $100 \mu\text{m}$  diameter are formed and fill the sample chamber.

### 3.3 Materials and Methods

Microfluidic chips of the design shown in Fig. 3.2 were fabricated from PMMA sheet material by laser cutting, and subsequent bonding of layers with a plasticiser under heat and pressure [142]. The chips consist of a top and bottom layer of  $200 \mu\text{m}$  thickness each, and a middle layer of  $500 \mu\text{m}$ . Fluid channels upstream from the flow-focussing droplet generator were scored into the middle layer at low laser power to a depth of about  $100 \mu\text{m}$ . Downstream from the droplet generator, the channels and the sample chamber

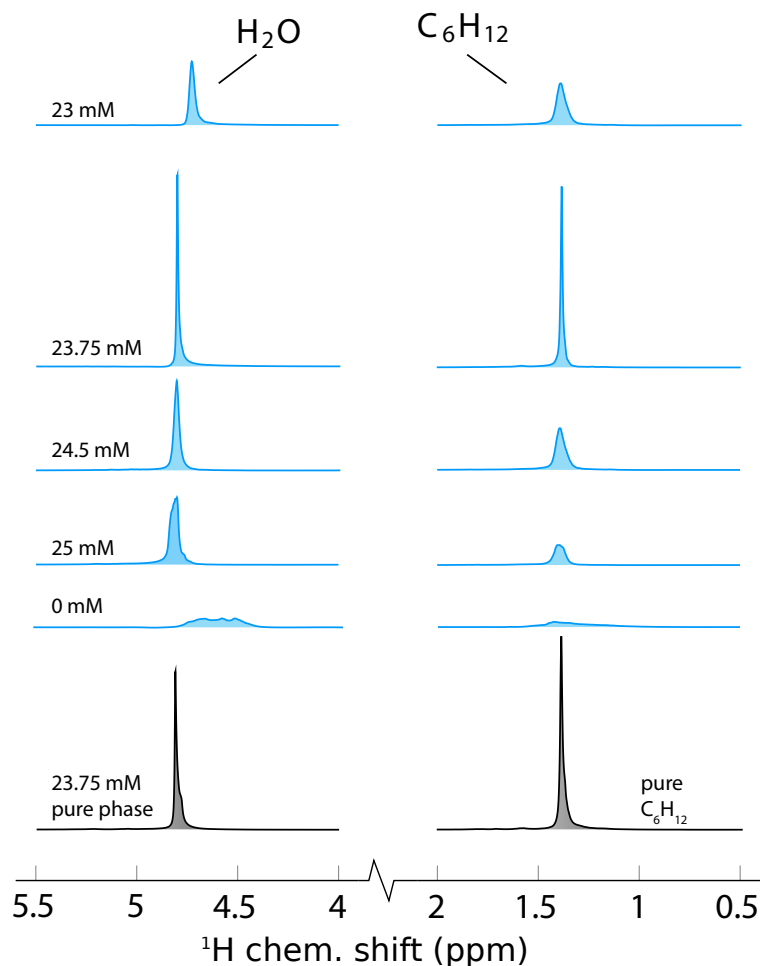


FIGURE 3.5:  $^1\text{H}$  NMR line shapes of water (left) and cyclohexane (right) of a water in cyclohexane emulsion as a function of  $\text{Eu}[\text{DTPA}]^{2-}$  concentration in the aqueous phase normalised to the sharpest peak. The spectra given in black are the pure phase spectra produced by the same chip.

were cut through the  $500 \mu\text{m}$  middle layer by increased laser power, as were the shimming structures. The chips were connected to a pair of Cole-Palmer 200-CE syringe pumps for droplet generation. A flow rate of  $20 \mu\text{l}/\text{min}$  was typically used for the continuous phase and  $4 \mu\text{l}/\text{min}$  for the aqueous droplet phase. The continuous phase consisted of cyclohexane (Sigma-Aldrich) with 0.5% w/v of span-65 (sorbitan tristearate, Sigma-Aldrich) as a surfactant to ensure droplet stability. The cyclohexane/span solution was kept in a water bath at  $30^\circ\text{C}$  for at least 2h to ensure complete dissolution of the surfactant. Prior to use, all solutions were left to equilibrate at a controlled room temperature of  $25^\circ\text{C}$  for at least 4h. Steady state conditions were ensured by letting the droplet generation run until the volume inside the chip had been exchanged at least five times. The chip was then disconnected from the syringe pumps, and the connection points sealed prior to insertion of the chip into the NMR probe.

NMR measurements were carried out on a Bruker AVANCE III spectrometer equipped

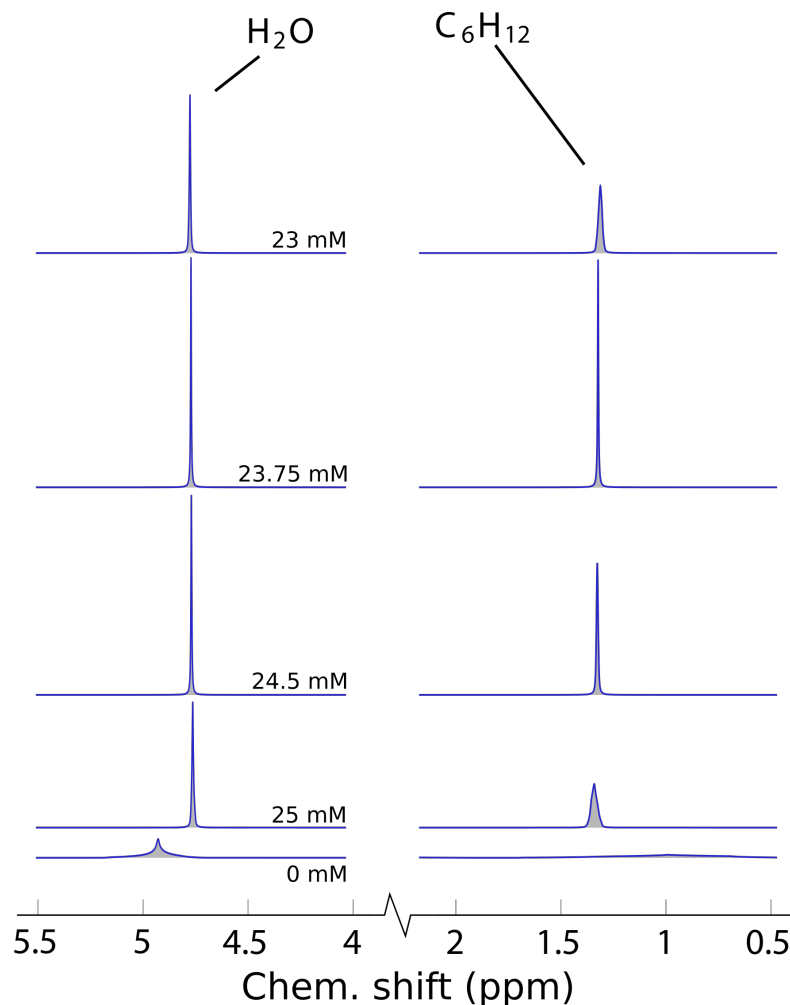


FIGURE 3.6: Predicted  $^1\text{H}$  NMR line shapes of water (left) and cyclohexane (right) of a water in cyclohexane emulsion as a function of  $\text{Eu}[\text{DTPA}]^{2-}$  concentration in the aqueous phase.

with an Oxford wide bore magnet operating at 7.05 Tesla, corresponding to a  $^1\text{H}$  Larmor frequency of 300 MHz. A home-built NMR probe based on a transmission-line detector was used[26]. It accommodates microfluidic chips of the shape shown in Fig. 3.2. In the present work, the probe was doubly tuned to allow irradiation both at 300 MHz for  $^1\text{H}$  and at 75 MHz for  $^{13}\text{C}$ . Details of the electronic and mechanical design of the probe are given in Ref. [143].

NMR spectra were obtained at an RF nutation frequency of 66 kHz for  $^1\text{H}$ , corresponding to 90 degree pulse length of 3.8  $\mu\text{s}$ . Shimming was first performed on a sample of pure cyclohexane in an identical chip, these resulting values were used throughout all subsequent experiments with minor adjustments being made to linear shims (X,Y,Z) before each experiment to minimise line width. NMR spectra were acquired using Bruker spectrometer software (TopSpin 2.0), and were processed using home-built scripts written in

*Julia.*[144] 20 mM of 4,4-Dimethyl-4-silapentane-1-sulfonic acid (DSS, Sigma Aldrich) was added to the aqueous phase as a chemical shift standard.

MRI gradient echo images of the sample chamber were obtained using ParaVision software and the fast low-angle shot (FLASH) pulse program. Flip angles of 30° were employed as well as a repetition time of 600 ms; 8 scans were averaged for each image. Two images were acquired for each field map at echo times of 6 and 10ms, respectively. The data was processed using home built software in *Mathematica*.

$\text{Eu}[\text{DTPA}]^{2-}$  solutions were prepared from a  $82.2 \pm 0.25$  mM stock solution, which was prepared by adding 1 g of  $\text{EuCl}_3$  (Sigma Aldrich) to a 50 mL volumetric flask. Separately, 3.93 g of diethylenetriaminepentaacetic acid (DTPA, Sigma Aldrich) and 1.99 g of NaOH (Fischer) were dissolved in 100 mL deionised (DI) water (Sigma Aldrich). An equimolar amount of the DTPA solution was added to the  $\text{EuCl}_3$  solution. The pH of this solution was then adjusted by addition of 2M NaOH solution dropwise until a neutral pH was attained. This was then topped up to 50 mL using DI water.

Finite element calculations of field distributions in emulsions were carried out using COMSOL Multiphysics with the "magnetic fields, no currents" (mfnc) physics module. Optimisation of the shim structures was done with COMSOL Multiphysics[145] Starting from a SolidWorks model of the chip design, which was also used as a basis for production of the devices using a laser cutter, a finite element model was assembled and meshed. The shim structures consist of four symmetrically arranged circular holes through the middle layer of the three-layered devices. The positions and the diameters of these holes were optimised using a Nelder-Mead simplex algorithm. At each iteration, the magnetic field distribution inside the sample chamber was calculated using the mfnc physics module. The square norm of the second derivative of the  $z$ -component of the magnetic field was integrated over the volume of the sample chamber, and was used as optimisation target.

### 3.4 Results and Discussion

While it is possible to predict the magnetic field distribution in a system of multiple phases with differing susceptibilities by solving the magnetostatic equation (Eqn. 3.8), this requires precise geometric information on the arrangement of the two phases. In the case of an emulsion, the arrangement of the droplets is not regular. However, at high droplet densities, it can be expected to approximate a dense packing of spheres. In order to obtain a semi-quantitative prediction, the demagnetising field in face-centred cubic (FCC) and simple cubic (SC) lattices of diamagnetic spheres was simulated; the results are shown in Fig. 3.4. A single unit cell containing one (SC) or two (FCC) independent spheres was meshed under periodic boundary conditions in all directions (Fig. 3.4C). As is well known, the demagnetising field inside an isolated diamagnetic

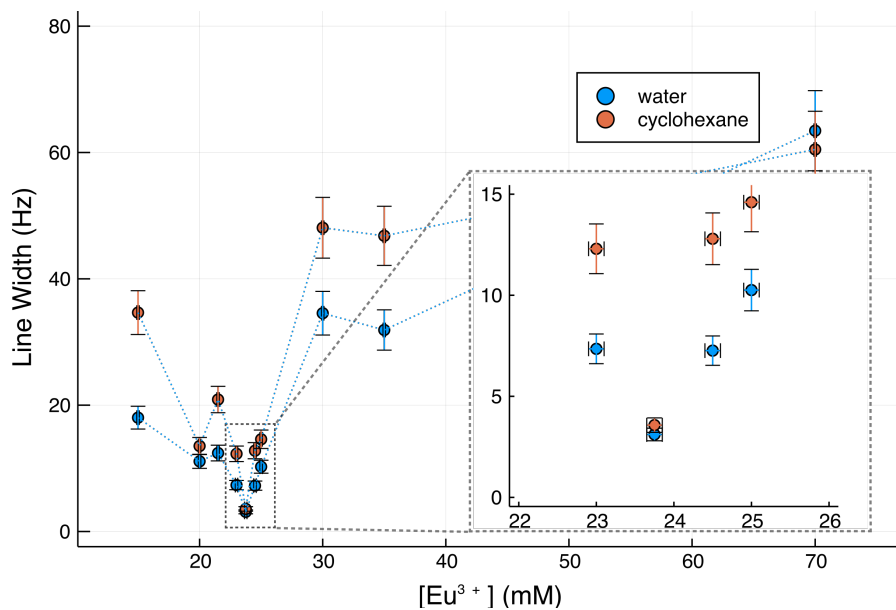


FIGURE 3.7: Observed line widths of water (blue circles) and cyclohexane (orange circles) in microfluidic droplet emulsions as a function of the Eu[DTPA]<sup>2-</sup> concentration in the aqueous phase. Inset is the plot around the minimum concentration. The widths of both lines are minimal at the matched concentration of 23.75 mM.

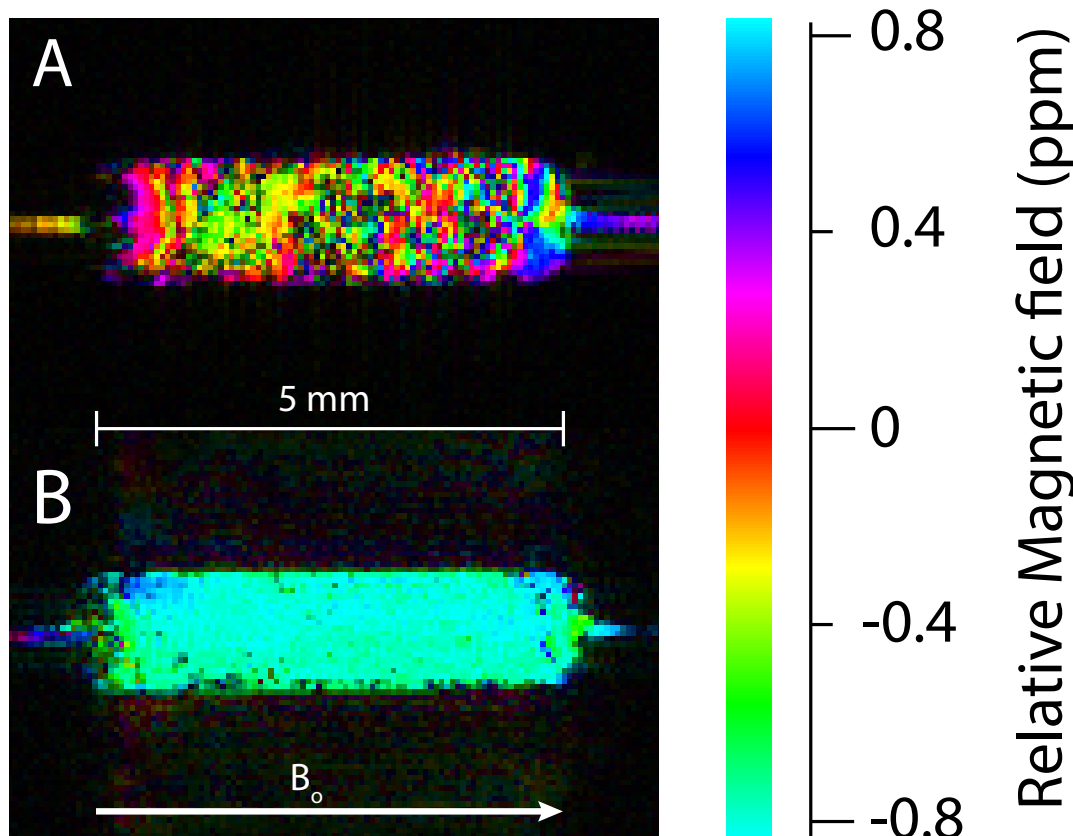


FIGURE 3.8:  $B_0$  Field maps obtained by magnetic resonance imaging of emulsions with (A)  $\Delta\chi = -1.41 \times 10^{-6}$  and (B)  $\Delta\chi \approx 0$ .

sphere is homogeneous, while the field outside of the sphere is that of a magnetic point dipole located at the sphere's centre. This situation is approximated in a lattice if the lattice constant is much larger than the sphere diameter. The computed demagnetising field of a small sphere in an SC lattice is shown in Fig. 3.4A. The contour levels display the  $z$ -component of the local demagnetising field normalised by the background  $B_0$  field and the susceptibility difference  $\Delta\chi = \chi_{\text{sphere}} - \chi_{\text{continuous}}$ . The field is homogeneous inside the sphere, and a spatially varying demagnetising field only exists in the continuous phase. By contrast, in a densely packed face-centered cubic lattice the field is no longer homogeneous inside the spheres (Fig. 3.4B). The FCC lattice approximates the geometry of a dense microemulsion of homogenous water-in-oil droplets. Fig. 3.4D shows the histograms of the  $z$ -components of the demagnetising field in the continuous and droplet phases of the FCC lattice, respectively.

The NMR spectra expected from an ideal emulsion of the same geometry can be predicted from these histograms (neglecting no broadening contributions from the sample container). The magnetic field relevant for nuclear Larmor precession, often referred to as the "external" field [127]  $\mathbf{B}_{\text{ext}}$  from Eqn. 3.10 is given by:

$$\mathbf{B}_{\text{ext}}(\mathbf{r}) = B_0(1 + \frac{\chi_s}{3})\mathbf{e}_z - \mu_0\nabla U_d(\mathbf{r}), \quad (3.11)$$

where  $B_0$  is the magnitude of the external field,  $\chi_s$  is the local magnetic susceptibility, and  $U_d(\mathbf{r})$  is the scalar magnetic potential of the demagnetising field. The volume susceptibility of a solution containing a paramagnetic species at low concentration  $c_p$  is

$$\chi_s \approx \chi_0 + c_p \zeta_P, \quad (3.12)$$

where  $\chi_0$  is the volume susceptibility of the pure solvent, and  $\zeta_P$  is the molar susceptibility of the paramagnetic species.  $\zeta_P$  depends slightly on the molecular environment. For example, values of  $5.86 \cdot 10^{-5}$  l/Mol,  $5.68 \cdot 10^{-5}$  l/Mol, and  $6.14 \cdot 10^{-5}$  l/Mol have been measured at 300K for  $\text{Eu}_2\text{O}_3$ ,  $\text{EuF}_3$ , and  $\text{EuBO}_3$ , respectively[146]. To our knowledge, the precise molar susceptibility of  $\text{Eu}[\text{DTPA}]^{2-}$  in aqueous solution has not been measured to date, but it is likely to be similar to the above values.

Fig. 3.5 shows  $^1\text{H}$  NMR spectra obtained from emulsions in the chip shown in Fig. 3.2 with varying  $\text{Eu}[\text{DTPA}]^{2-}$  concentrations in the aqueous phase as indicated in the figure. While the spectra are extremely broad without dopant, concentrations in the vicinity of 23 mM lead to much sharper lines for both water and cyclohexane, and the pure phase line widths are recovered at the optimum concentration of  $c_p = 23.75$  mM. Using the susceptibilities for  $\text{H}_2\text{O}$  and cyclohexane given in Table 3.1, this leads to molar susceptibility for  $\text{Eu}[\text{DTPA}]^{2-}$  of  $5.94 \cdot 10^{-5}$  l/Mol, well within the range of molar susceptibilities reported in literature for other  $\text{Eu}^{3+}$  compounds. Using this value, the histograms shown in Fig. 3.4D can be converted into predicted emulsion NMR spectra

as a function of  $\text{Eu}[\text{DTPA}]^{2-}$  concentration in the aqueous phase, as shown in Fig. 3.6. The predicted behaviour is qualitatively similar to the experimental observation; very broad lines are expected at zero dopant concentration, while sharp lines are recovered near the optimum concentration. Also, the droplet phase peak is predicted to be narrower than the one from the continuous phase; this is already evident in the histograms in Fig. 3.4. However, the predicted spectra are consistently sharper than the experimentally observed ones. It is not entirely clear what causes the discrepancy between the experimental observation and the simulations. However, it should be noted that the experimental geometry of the emulsion differs significantly from the simulation; the droplets are neither uniform in size, nor are they arranged in a crystalline (FCC) lattice.

The observed widths of the NMR signals from cyclohexane and water are summarised in Fig. 3.7. Here, we define the line width as the ratio of the peak integral to the peak height, multiplied by  $2/\pi$ . In the case of Lorentzian line shapes, this definition is equivalent to the full width at half height (FWHM). However, the expected line shapes from the droplet emulsion are very different from a Lorentzian (Fig. 3.4D), such that using the FWHM would be misleading.

Both line widths exhibit a narrow minimum at 23.75 mM  $\text{Eu}[\text{DTPA}]^{2-}$  in the aqueous phase. The water and cyclohexane minimum peak widths are 3.1 Hz and 3.5 Hz, respectively. For comparison, the best resolution that has been reached with the same NMR probe is 1.76 Hz for a homogeneous solution of 150 mM sodium acetate in  $\text{H}_2\text{O}$ .[26]

Fig. 3.8 shows magnetic field ( $B_0$ ) maps of the sample chambers filled with droplet emulsions. In these experiments, two separate images with different echo times are acquired. The phase difference in each pixel is therefore proportional to the echo time difference and to the local magnetic field. The echo time difference is constant therefore the colour denotes the phase acquired by each pixel and can be used to inform on the homogeneity of the magnetic field in the sample.

In Fig. 3.8A, the droplets do not contain any paramagnetic dopant. As a result, the susceptibilities of the phases are unmatched, and strong local magnetic field differences are visible in the images. By contrast, the droplets in Fig. 3.8B are doped with 23.75 mM  $\text{Eu}[\text{DTPA}]^{2-}$ . As is clearly visible in the image, the local differences in the magnetic fields are strongly attenuated in this case.

While the above results have demonstrated that optimal line widths can be minimised in  $^1\text{H}$  NMR spectra of microfluidic emulsions by paramagnetic doping, the question remains if this is sufficient to resolve homonuclear  $J$ -couplings of a few Hz. This is required in order to do meaningful NMR spectroscopy, particularly in the context of complex metabolic mixtures. The top trace in Fig. 3.9 shows a spectrum of 200 mM glucose and 23.75 mM  $\text{Eu}[\text{DTPA}]^{2-}$  in water. The water signal has been suppressed by pre-saturation. In this case, the resolution is about 3 Hz; such that e.g., the triplet at

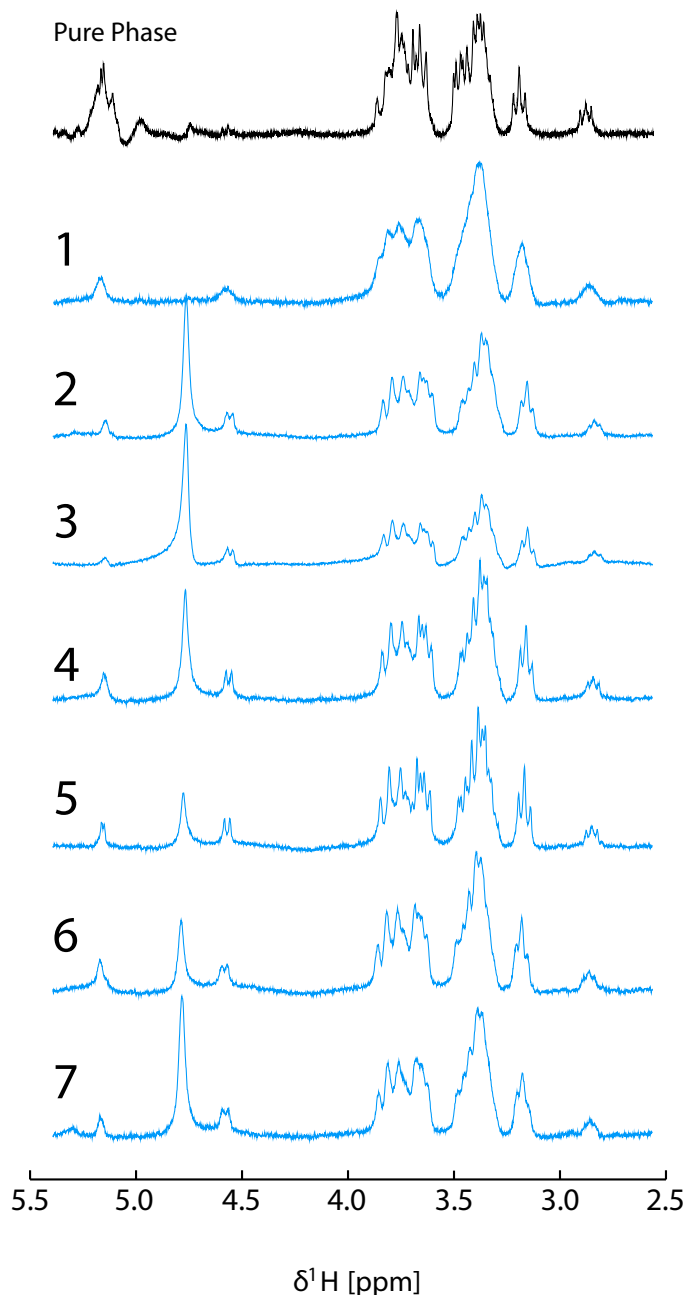


FIGURE 3.9: Spectra of 200 mM Glucose in  $\text{H}_2\text{O}$  obtained from microfluidic droplet emulsions in cyclohexane. 1: Aqueous phase contains  $c_0 = 23.75 \pm 0.25. Spectra 2-7 have been obtained by gradual dilution of the aqueous phase with small amounts of DI water. 2:  $\ln c/c_0 = -0.5\%$ ; 3:  $\ln c/c_0 = -0.75\%$ ; 4 :  $\ln c/c_0 = -0.875\%$ ; 5 :  $\ln c/c_0 = -1.0\%$ ; 6 :  $\ln c/c_0 = -1.125\%$ ; 7 :  $\ln c/c_0 = -1.25\%$ . A spectrum of pure phase 200mM glucose with optimised Eu doping in the same chip is included for comparison (black). The nonuniform peak at 4.8 ppm is due to carrier frequency drift during water suppression$

3.2 ppm (which corresponds to the proton in the 2-position on the  $\beta$ -glucose anomer) is clearly resolved.

Spectrum 1 in Fig. 3.9 has been obtained from droplet emulsions, starting from an aqueous stock solution prepared to a nominal concentration of 23.75 mM in Eu[DTPA] $^{2-}$  and 200 mM in glucose. Initially, the resolution in this spectrum is quite poor, in spite of the attempt to dope at the previously determined optimum concentration. Estimates predicted the pipetting and weighing errors to add up to an uncertainty in the concentration of the stock solution of  $\pm 1\%$ . Assuming the stock solution was too concentrated, rather than too dilute, it was then gradually diluted with small amounts of DI water corresponding to a change in concentration much less than the experimental error in each step. As can be seen in spectra 2-7, the resolution gradually increases, and matches the pure phase spectrum at spectrum 5, before it deteriorates again. In practice, high resolution spectra therefore require careful calibration of the dopant concentration. It may not be practical to achieve this in one step by preparing the stock solution, particularly if small volumes are used as in our experiments. Rather, a gradual dilution as in Fig. 3.9 may be required to calibrate the Eu[DTPA] $^{2-}$  concentration for an accurate match of the aqueous and carrier fluid susceptibilities. However, if such a match is established, the resulting resolution is as good as that of the pure aqueous solution.

### 3.5 Conclusion

Susceptibility differences between the chip, the aqueous phase, and the oil phase in a microfluidic droplet system can be successfully mitigated by a combination of structural shimming and doping of the less diamagnetic of the liquid phases with a europium compound. The ultimate resolution achieved is only slightly inferior to what has been demonstrated in homogeneous solutions on a microfluidic chip and is suitable for high resolution NMR spectroscopy.



# Bibliography

- [1] M. Sharma and M. Utz, *Journal of Magnetic Resonance*, 2019.
- [2] D. B. Weibel, M. Kruithof, S. Potenta, S. K. Sia, A. Lee and G. M. Whitesides, *Analytical chemistry*, 2005, **77**, 4726–4733.
- [3] T. Thorsen, R. W. Roberts, F. H. Arnold and S. R. Quake, *Physical review letters*, 2001, **86**, 4163.
- [4] F. K. Balagaddé, L. You, C. L. Hansen, F. H. Arnold and S. R. Quake, *Science*, 2005, **309**, 137–140.
- [5] P. J. Hung, P. J. Lee, P. Sabourchi, R. Lin and L. P. Lee, *Biotechnology and bioengineering*, 2005, **89**, 1–8.
- [6] S. Takayama, E. Ostuni, P. LeDuc, K. Naruse, D. E. Ingber and G. M. Whitesides, *Nature*, 2001, **411**, 1016.
- [7] A. R. Wheeler, W. R. Throndset, R. J. Whelan, A. M. Leach, R. N. Zare, Y. H. Liao, K. Farrell, I. D. Manger and A. Daridon, *Analytical chemistry*, 2003, **75**, 3581–3586.
- [8] J. Voldman, M. Gray, M. Toner and M. Schmidt, *Anal. Chem.*, 2002, **74**, 3984–3990.
- [9] Z. Wang, J. El-Ali, M. Engelund, T. Gotsaed, I. Perch-Nielsen, K. B. Mogensen, D. Snakenborg, J. P. Kutter and A. Wolff, *Lab on a Chip*, 2004, **4**, 372–377.
- [10] D. Di Carlo, K.-H. Jeong and L. P. Lee, *Lab on a Chip*, 2003, **3**, 287–291.
- [11] S.-W. Lee and Y.-C. Tai, *Sensors and Actuators A: Physical*, 1999, **73**, 74–79.
- [12] H. Lu, S. Gaudet, M. A. Schmidt and K. F. Jensen, *Analytical chemistry*, 2004, **76**, 5705–5712.
- [13] Y. Li, J. S. Buch, F. Rosenberger, D. L. DeVoe and C. S. Lee, *Analytical chemistry*, 2004, **76**, 742–748.
- [14] K. Sato, M. Yamanaka, H. Takahashi, M. Tokeshi, H. Kimura and T. Kitamori, *Electrophoresis*, 2002, **23**, 734–739.

- [15] T. P. Burg and S. R. Manalis, *Applied Physics Letters*, 2003, **83**, 2698–2700.
- [16] J. El-Ali, P. K. Sorger and K. F. Jensen, *Nature*, 2006, **442**, 403.
- [17] Y. Nakao, H. Kimura, Y. Sakai and T. Fujii, *Biomicrofluidics*, 2011, **5**, 022212.
- [18] K.-J. Jang and K.-Y. Suh, *Lab on a Chip*, 2010, **10**, 36–42.
- [19] D. Huh, B. D. Matthews, A. Mammoto, M. Montoya-Zavala, H. Y. Hsin and D. E. Ingber, *Science*, 2010, **328**, 1662–1668.
- [20] J. H. Sung and M. L. Shuler, *Lab on a Chip*, 2009, **9**, 1385–1394.
- [21] D. Huh, Y.-s. Torisawa, G. A. Hamilton, H. J. Kim and D. E. Ingber, *Lab on a Chip*, 2012, **12**, 2156–2164.
- [22] V. Badilita, R. C. Meier, N. Spengler, U. Wallrabe, M. Utz and J. G. Korvink, *Soft Matter*, 2012, **8**, 10583–10597.
- [23] R. C. Meier, J. Höfflin, V. Badilita, U. Wallrabe and J. G. Korvink, *J. Micromech. Microeng.*, 2014, **24**, 045021.
- [24] N. Spengler, A. Moazenzadeh, R. C. Meier, V. Badilita, J. Korvink and U. Wallrabe, *Journal of Micromechanics and Microengineering*, 2014, **24**, 034004.
- [25] H. Ryan, A. Smith and M. Utz, *Lab on a Chip*, 2014, **14**, 1678–1685.
- [26] G. Finch, A. Yilmaz and M. Utz, *Journal of Magnetic Resonance*, 2016, **262**, 73–80.
- [27] H. Fang, Y. Sun, X. Wang, M. Sharma, Z. Chen, X. Cao, M. Utz and Z. Tian, *Science China Chemistry*, 2018, **61**, 1460–1464.
- [28] S. Terry, J. Jerman and J. Angell, *IEEE Trans. Electron. Devices*, 1979, **26**, 1880.
- [29] D. R. Reyes, D. Iossifidis, P.-A. Auroux and A. Manz, *Analytical chemistry*, 2002, **74**, 2623–2636.
- [30] H. Van Lintel, F. Van de Pol and S. Bouwstra, *Sensors and actuators*, 1988, **15**, 153–167.
- [31] F. Van De Pol, D. Wonnink, M. Elwenspoek and J. Fluitman, *Sensors and Actuators*, 1989, **17**, 139–143.
- [32] S. Shoji, M. Esashi and T. Matsuo, *Sensors and Actuators*, 1988, **14**, 101–107.
- [33] A. Manz, Y. Miyahara, J. Miura, Y. Watanabe, H. Miyagi and K. Sato, *Sensors and actuators B: Chemical*, 1990, **1**, 249–255.
- [34] A. Manz, N. Graber and H. á. Widmer, *Sensors and actuators B: Chemical*, 1990, **1**, 244–248.

- [35] A. Manz, D. Harrison, J. Fettinger, E. Verpoorte, H. Ludi and H. Widmer, TRANSDUCERS'91: 1991 International Conference on Solid-State Sensors and Actuators. Digest of Technical Papers, 1991, pp. 939–941.
- [36] D. J. Harrison, A. Manz, Z. Fan, H. Luedi and H. M. Widmer, *Analytical chemistry*, 1992, **64**, 1926–1932.
- [37] K. Seiler, D. J. Harrison and A. Manz, *Analytical Chemistry*, 1993, **65**, 1481–1488.
- [38] A. T. Woolley, D. Hadley, P. Landre, A. J. deMello, R. A. Mathies and M. A. Northrup, *Analytical Chemistry*, 1996, **68**, 4081–4086.
- [39] L. Bousse, R. McReynolds, G. Kirk, T. Dawes, P. Lam, W. Bemiss and J. Parce, *Sensors and Actuators B: Chemical*, 1994, **20**, 145–150.
- [40] G. M. Whitesides, *Nature*, 2006, **442**, 368–73.
- [41] J. M. Ng, I. Gitlin, A. D. Stroock and G. M. Whitesides, *Electrophoresis*, 2002, **23**, 3461–3473.
- [42] G. M. Whitesides and A. D. Stroock, *Phys. Today*, 2001, **54**, 42–48.
- [43] J. C. McDonald, D. C. Duffy, J. R. Anderson, D. T. Chiu, H. Wu, O. J. Schueller and G. M. Whitesides, *ELECTROPHORESIS: An International Journal*, 2000, **21**, 27–40.
- [44] A. Günther, M. Jhunjhunwala, M. Thalmann, M. A. Schmidt and K. F. Jensen, *Langmuir*, 2005, **21**, 1547–1555.
- [45] D. J. Laser and J. G. Santiago, *Journal of micromechanics and microengineering*, 2004, **14**, R35.
- [46] C. L. Hansen, E. Skordalakes, J. M. Berger and S. R. Quake, *Proceedings of the National Academy of Sciences*, 2002, **99**, 16531–16536.
- [47] R. Ramsey and J. Ramsey, *Analytical Chemistry*, 1997, **69**, 1174–1178.
- [48] C.-C. Lee, G. Sui, A. Elizarov, C. J. Shu, Y.-S. Shin, A. N. Dooley, J. Huang, A. Daridon, P. Wyatt, D. Stout *et al.*, *Science*, 2005, **310**, 1793–1796.
- [49] T. Thorsen, R. W. Roberts, F. H. Arnold and S. R. Quake, *Physical review letters*, 2001, **86**, 4163.
- [50] D. Link, S. L. Anna, D. Weitz and H. Stone, *Physical review letters*, 2004, **92**, 054503.
- [51] Y.-C. Tan, J. S. Fisher, A. I. Lee, V. Cristini and A. P. Lee, *Lab on a Chip*, 2004, **4**, 292–298.

- [52] Z. Nie, S. Xu, M. Seo, P. C. Lewis and E. Kumacheva, *Journal of the American chemical society*, 2005, **127**, 8058–8063.
- [53] T. Nisisako and T. Torii, *Advanced materials*, 2007, **19**, 1489–1493.
- [54] A. Utada, E. Lorenceau, D. Link, P. Kaplan, H. Stone and D. Weitz, *Science*, 2005, **308**, 537–541.
- [55] A. Huebner, M. Srisa-Art, D. Holt, C. Abell, F. Hollfelder, J. Edel *et al.*, *Chemical communications*, 2007, 1218–1220.
- [56] A. Folch, A. Ayon, O. Hurtado, M. Schmidt and M. Toner, *Journal of biomechanical engineering*, 1999, **121**, 28–34.
- [57] A. Folch and M. Toner, *Annual review of biomedical engineering*, 2000, **2**, 227–256.
- [58] V. L. Tsang and S. N. Bhatia, *Advanced drug delivery reviews*, 2004, **56**, 1635–1647.
- [59] A. Sivaraman, J. Leach, S. Townsend, T. Iida, B. Hogan, D. B. Stoltz, R. Fry, L. Samson, S. Tannenbaum and L. Griffith, *Current drug metabolism*, 2005, **6**, 569–591.
- [60] M. J. Powers, K. Domansky, M. R. Kaazempur-Mofrad, A. Kalezi, A. Capitano, A. Upadhyaya, P. Kurzawski, K. E. Wack, D. B. Stoltz, R. Kamm *et al.*, *Biotechnology and bioengineering*, 2002, **78**, 257–269.
- [61] C. Guguen-Guilhouzo, B. Clément, G. Baffet, C. Beaumont, E. Morel-Chany, D. Glaise and A. Guilhouzo, *Experimental cell research*, 1983, **143**, 47–54.
- [62] C. S. Chen, M. Mrksich, S. Huang, G. M. Whitesides and D. E. Ingber, *Science*, 1997, **276**, 1425–1428.
- [63] S. Bhatia, U. Balis, M. Yarmush and M. Toner, *The FASEB journal*, 1999, **13**, 1883–1900.
- [64] M. Esch, T. King and M. Shuler, *Annual review of biomedical engineering*, 2011, **13**, 55–72.
- [65] A. Skardal, T. Shupe and A. Atala, *Drug discovery today*, 2016, **21**, 1399–1411.
- [66] J. Wang, *Biosensors and Bioelectronics*, 2006, **21**, 1887–1892.
- [67] R. Raiteri, M. Grattarola, H.-J. Butt and P. Skládal, *Sensors and Actuators B: Chemical*, 2001, **79**, 115–126.
- [68] B. Kuswandi, J. Huskens, W. Verboom *et al.*, *Analytica chimica acta*, 2007, **601**, 141–155.
- [69] N. Pires, T. Dong, U. Hanke and N. Hoivik, *Sensors*, 2014, **14**, 15458–15479.

- [70] R. J. Flanagan, D. Perrett and R. Whelpton, *Electrochemical detection in HPLC: Analysis of drugs and poisons*, Royal Society of Chemistry, 2005, vol. 10.
- [71] P. S. Waggoner and H. G. Craighead, *Lab on a Chip*, 2007, **7**, 1238–1255.
- [72] M. Ferrari, *Nature reviews cancer*, 2005, **5**, 161.
- [73] H. Hou, X. Bai, C. Xing, N. Gu, B. Zhang and J. Tang, *Analytical chemistry*, 2013, **85**, 2010–2014.
- [74] J. F. Rusling, C. V. Kumar, J. S. Gutkind and V. Patel, *Analyst*, 2010, **135**, 2496–2511.
- [75] A. M. Foudeh, T. F. Didar, T. Veres and M. Tabrizian, *Lab on a Chip*, 2012, **12**, 3249–3266.
- [76] S. Wang, X. Zhao, I. Khimji, R. Akbas, W. Qiu, D. Edwards, D. W. Cramer, B. Ye and U. Demirci, *Lab on a Chip*, 2011, **11**, 3411–3418.
- [77] J. R. Wojciechowski, L. C. Shriver-Lake, M. Y. Yamaguchi, E. Füreder, R. Pieler, M. Schamesberger, C. Winder, H. J. Prall, M. Sonnleitner and F. S. Ligler, *Analytical chemistry*, 2009, **81**, 3455–3461.
- [78] N. Yildirim, F. Long, C. Gao, M. He, H.-C. Shi and A. Z. Gu, *Environmental science & technology*, 2012, **46**, 3288–3294.
- [79] A. M. Foudeh, J. T. Daoud, S. P. Faucher, T. Veres and M. Tabrizian, *Biosensors and Bioelectronics*, 2014, **52**, 129–135.
- [80] M. Swanson and B. Hammer, *Annual Reviews in Microbiology*, 2000, **54**, 567–613.
- [81] I. S. Kinstlinger and J. S. Miller, *Lab on a Chip*, 2016, **16**, 2025–2043.
- [82] P. C. Gach, K. Iwai, P. W. Kim, N. J. Hillson and A. K. Singh, *Lab on a Chip*, 2017, **17**, 3388–3400.
- [83] B. Bao, J. Riordon, F. Mostowfi and D. Sinton, *Lab on a Chip*, 2017, **17**, 2740–2759.
- [84] S. Giulitti, M. Pellegrini, I. Zorzan, P. Martini, O. Gagliano, M. Mutarelli, M. J. Ziller, D. Cacchiarelli, C. Romualdi, N. Elvassore *et al.*, *Nature cell biology*, 2019, **21**, 275–.
- [85] J. Reboud, G. Xu, A. Garrett, M. Adriko, Z. Yang, E. M. Tukahebwa, C. Rowell and J. M. Cooper, *Proceedings of the National Academy of Sciences*, 2019, **116**, 4834–4842.
- [86] P. A. M. Dirac, *Mathematical Proceedings of the Cambridge Philosophical Society*, 1939, **35**, 416–418.

- [87] J. von Neumann, *Mathematical Foundations of Quantum Mechanics*, Princeton University Press, new edn, 2018.
- [88] F. Bloch, *Phys. Rev.*, 1946, **70**, 460–474.
- [89] D. I. Hoult and R. E. Richards, *Journal of Magnetic Resonance (1969)*, 1976, **24**, 71–85.
- [90] A. Abragam, *The Principles of Nuclear Magnetism*, Oxford University Press, 1961.
- [91] P. J. M. van Bentum, J. W. G. Janssen, A. P. M. Kentgens, J. Bart and J. G. E. Gardeniers, *Journal of Magnetic Resonance*, 2007, **189**, 104–113.
- [92] N. Spengler, J. Höfflin, A. Moazenzadeh, D. Mager, N. MacKinnon, V. Badilita, U. Wallrabe and J. G. Korvink, *PloS one*, 2016, **11**, e0146384.
- [93] I. Swyer, S. von der Ecken, B. Wu, A. Jenne, R. Soong, F. Vincent, D. Schmidig, T. Frei, F. Busse and H. J. Stronks, *Lab on a Chip*, 2019, **19**, 641–653.
- [94] W. Hale, G. Rossetto, R. Greenhalgh, G. Finch and M. Utz, *Lab Chip*, 2018, **18**, 3018–3024.
- [95] I. Kobayashi, Y. Wada, K. Uemura and M. Nakajima, *Microfluidics and Nanofluidics*, 2010, **8**, 255–262.
- [96] J. Zhang, R. J. Coulston, S. T. Jones, J. Geng, O. A. Scherman and C. Abell, *Science*, 2012, **335**, 690–694.
- [97] J. Ju, C. Zeng, L. Zhang and N. Xu, *Chemical Engineering Journal*, 2006, **116**, 115–121.
- [98] J. Kobayashi, Y. Mori, K. Okamoto, R. Akiyama, M. Ueno, T. Kitamori and S. Kobayashi, *Science*, 2004, **304**, 1305–1308.
- [99] U. Demirci and G. Montesano, *Lab on a Chip*, 2007, **7**, 1428–1433.
- [100] L. Mazutis, J. Gilbert, W. L. Ung, D. A. Weitz, A. D. Griffiths and J. A. Heyman, *Nature protocols*, 2013, **8**, 870.
- [101] W. Shi, J. Qin, N. Ye and B. Lin, *Lab on a Chip*, 2008, **8**, 1432–1435.
- [102] F. Schuler, M. Trotter, M. Geltman, F. Schwemmer, S. Wadle, E. Domínguez-Garrido, M. López, C. Cervera-Acedo, P. Santibáñez and F. von Stetten, *Lab on a Chip*, 2016, **16**, 208–216.
- [103] S. C. Kim, I. C. Clark, P. Shahi and A. R. Abate, *Analytical chemistry*, 2018, **90**, 1273–1279.
- [104] M. Y. Tang and H. C. Shum, *Lab on a Chip*, 2016, **16**, 4359–4365.

- [105] K. T. Kotz, Y. Gu and G. W. Faris, *Journal of the American Chemical Society*, 2005, **127**, 5736–5737.
- [106] S.-Y. Teh, R. Lin, L.-H. Hung and A. P. Lee, *Lab on a Chip*, 2008, **8**, 198–220.
- [107] M. He, J. S. Kuo and D. T. Chiu, *Applied Physics Letters*, 2005, **87**, 031916.
- [108] S.-H. Tan, N.-T. Nguyen, L. Yobas and T. G. Kang, *Journal of Micromechanics and Microengineering*, 2010, **20**, 045004.
- [109] B. Dura, M. M. Servos, R. M. Barry, H. L. Ploegh, S. K. Dougan and J. Voldman, *Proceedings of the National Academy of Sciences*, 2016, **113**, E3599–E3608.
- [110] W. Hale, G. Rossetto, R. Greenhalgh, G. Finch and M. Utz, *Lab on a Chip*, 2018.
- [111] P. Garstecki, I. Gitlin, W. DiLuzio, G. M. Whitesides, E. Kumacheva and H. A. Stone, *Applied Physics Letters*, 2004, **85**, 2649–2651.
- [112] P. Umbanhower, V. Prasad and D. A. Weitz, *Langmuir*, 2000, **16**, 347–351.
- [113] P. Zhu, T. Kong, Z. Kang, X. Tian and L. Wang, *Scientific reports*, 2015, **5**, 11102.
- [114] P. Zhu and L. Wang, *Lab on a Chip*, 2017, **17**, 34–75.
- [115] J. L. Markley, R. Brüscheiler, A. S. Edison, H. R. Eghbalnia, R. Powers, D. Raftery and D. S. Wishart, *Current opinion in biotechnology*, 2017, **43**, 34–40.
- [116] R. Powers, *Magnetic Resonance in Chemistry*, 2009, **47**, S2–S11.
- [117] V. Kasivisvanathan, A. S. Rannikko, M. Borghi, V. Panebianco, L. A. Mynderse, M. H. Vaarala, A. Briganti, L. Budäus, G. Hellawell and R. G. Hindley, *New England Journal of Medicine*, 2018, **378**, 1767–1777.
- [118] M. H. Horrocks, L. Tosatto, A. J. Dear, G. A. Garcia, M. Iljina, N. Cremades, M. Dalla Serra, T. P. Knowles, C. M. Dobson and D. Kleinerman, *Analytical chemistry*, 2015, **87**, 8818–8826.
- [119] S. Schlimpert, K. Flärdh and M. J. Buttner, *JoVE (Journal of Visualized Experiments)*, 2016, e53863.
- [120] E. A. Redman, J. S. Mellors, J. A. Starkey and J. M. Ramsey, *Analytical chemistry*, 2016, **88**, 2220–2226.
- [121] K. Choi, E. Boyaci, J. Kim, B. Seale, L. Barrera-Arbelaez, J. Pawliszyn and A. R. Wheeler, *Journal of Chromatography A*, 2016, **1444**, 1–7.
- [122] S. S. Zalesskiy, E. Danieli, B. Blümich and V. P. Ananikov, *Chem. Rev*, 2014, **114**, 5641–5694.

- [123] N. Spengler, J. Höfflin, A. Moazenzadeh, D. Mager, N. MacKinnon, V. Badilita, U. Wallrabe and J. G. Korvink, *Plos One*, 2016, **11**, e0146384.
- [124] P. W. Kuchel, B. E. Chapman, W. A. Bubb, P. E. Hansen, C. J. Durrant and M. P. Hertzberg, *Concepts in Magnetic Resonance Part A*, 2003, **18A**, 56–71.
- [125] C. J. Durrant, M. P. Hertzberg and P. W. Kuchel, *Concepts Magn. Reson.*, 2003, **18A**, 72–95.
- [126] J. D. Jackson, *Classical Electrodynamics*, John Wiley & Sons, 3rd edn, 2007.
- [127] M. H. Levitt, *Concepts Magn. Reson.*, 1996, **8**, 77–103.
- [128] J. C. VANDENENDEN, D. WADDINGTON, H. VANALST, C. G. VANKRALINGEN and K. J. PACKER, *Journal of Colloid and Interface Science*, 1990, **140**, 105–113.
- [129] I. FOUREL, J. P. GUILLEMENT and D. LEBOTLAN, *Journal of Colloid and Interface Science*, 1994, **164**, 48–53.
- [130] K. G. Hollingsworth, A. J. Sederman, C. Buckley, L. F. Gladden and M. L. Johns, *Journal of Colloid and Interface Science*, 2004, **274**, 244–250.
- [131] J. P. Hindmarsh, J. H. Su, J. Flanagan and H. Singh, *Langmuir*, 2005, **21**, 9076–9084.
- [132] M. L. Johns, *Current Opinion in Colloid & Interface Science*, 2009, **14**, 178–183.
- [133] R. Bernewitz, G. Guthausen and H. P. Schuchmann, *Magnetic Resonance in Chemistry*, 2011, **49**, S93–S104.
- [134] I. A. Lingwood, T. C. Chandrasekera, J. Kolz, E. O. Fridjonsson and M. L. Johns, *Journal of Magnetic Resonance*, 2012, **214**, 281–288.
- [135] M. E. Fabry and R. C. San George, *Biochemistry*, 1983, **22**, 4119–4125.
- [136] A. J. Lennon, N. R. Scott, B. E. Chapman and P. W. Kuchel, *Biophysical journal*, 1994, **67**, 2096–2109.
- [137] J. A. Peters, J. Huskens and D. J. Raber, *Progress in Nuclear Magnetic Resonance Spectroscopy*, 1996, **28**, 283–350.
- [138] *CRC Handbook of Chemistry and Physics*, ed. J. Rumble, 2017, pp. 1–4.
- [139] M. C. Wapler, J. Leupold, I. Dragonu, D. von Elverfeld, M. Zaitsev and U. Wallrabe, *Journal of Magnetic Resonance*, 2014, **242**, 233–242.
- [140] C. J. G. Bakker and R. de Roos, *Magn. Reson. Med.*, 2006, **56**, 1107–1113.
- [141] H. Ryan, A. Smith and M. Utz, *Lab Chip*, 2014, **14**, 1678–1685.

- [142] A. Yilmaz and M. Utz, *Lab Chip*, 2016, **16**, 2079–2085.
- [143] G. R. Finch, *PhD thesis*, University of Southampton, Southampton, 2017.
- [144] J. Bezanson, A. Edelman, S. Karpinski and V. B. Shah, *SIAM Rev.*, 2017, **59**, 65–98.
- [145] COMSOL Inc., *COMSOL Multiphysics®*, <https://www.comsol.com>.
- [146] Y. Takikawa, S. Ebisu and S. Nagata, *Journal of Physics and Chemistry of Solids*, 2010, **71**, 1592–1598.